Alma Mater Studiorum – Università di Bologna

DOTTORATO DI RICERCA IN

CHIMICA

Ciclo XXIX

Settore Concorsuale di afferenza: 03/A2

Settore Scientifico disciplinare: CHIM02

INVESTIGATION OF CELL-MATERIAL INTERACTIONS BY SCANNING PROBE MICROSCOPY

Presentata da: **Luca Bartolini**

Coordinatore Dottorato

Aldo Roda

Relatore

Stefania Rapino

Correlatore

Cristiano Albonetti

Esame finale anno 2017

Indice

Preface **1**

1. Introduction and Principles of scanning Electrochemical Microscopy and Atomic Force Microscopy **4**
Scanning Electrochemical Microscopy 4
Background 4
Principle of SECM 4
Applications 11
SECM Imaging 12
Setup 13
SECM of Biological Systems 14
SECM of Single Living Cells 15
Atomic Force Microscopy 17
Ex-Situ Atomic Force Microscopy Measurements 17
AFM Main Components 19
References 23

2. Organic Monomolecula Layer Fabbrication **26**
Organic Molecular Beam Epitaxy on Silicon oxide Substrates 26
Organic mono-Molecular Layers Fabrication 27
Materials 29
Growth of a Monolayer of α-Sexithiophene (6T) on native SiO_x 31
Growth of a Monolayer of P5 34
Growth of a Monolayer PDI8-CN2 35
A brief description of the partial annealing process 37
Surface Characterization by SECM 38
References 41

3. Characterization of Cell-Organic Monolayer Interaction by Fluorescence Microscopy **42**

Procedure standardization 42
A. Optical Images of MCF10A on Native SiOx (control samples) 42
MCF10A on Native SiOx 48
MCF10A on Pentacene 50
MCF10A on PDI8-CN2 51
MCF10A on α-Sexithiophene 52
Materials and Methods 55
MCF10A Cells 55
Optical and Fluorescence Microscopy 59
Cell Fixation Protocol Optimized for SECM Investigation 59
References 62

4. Cell Morphology on Organic Monolayer Investigated by Scanning Electrochemical Microscopy 63
Sample Characterization by Scanning Electrochemical Microscopy: Experimental and Results 64
SECM Imaging of Cells on Organic Monolayers 65
Morphology Characterization Procedure 71
References 82

5. Novel Method for the Fabrication of SECM Nanoelectrodes 84
The New Etching System 92
Modification for use as SECM electrode 101
Insulation Procedure 102
References 104

Conclusions 106

Preface

An understanding of how material properties influence cellular behavior is of considerable interest. Biomedical disciplines like gene therapy, regenerative medicine, drug delivery and diagnostic have developed on the study of cell-material interactions. Tissue engineering focuses on the design and synthesis of materials that must not only support the new tissue, but also have to drive cellular response in the regeneration process. This can have specific applications as in regenerative medicine after trauma or degenerative diseases (e.g. osteoarthritis or osteoporosis).

The in vitro studies exploit synthetic and biological materials to assess their bioactivity, cytotoxicity, biocompatibility and biofunctionality.

Cell behavior on materials is regulated by soluble factors, extracellular cues and cell cues. These factors are coupled with each other, as usual, and thus it is very difficult to unambiguously elucidate the role of each regulator. [1] Surfaces can influence cell growth and differentiation through a physical property such as their morphology or through their chemical compositions.

In this work of thesis a fundamental study on the effects that organic monolayers of Pentacene (P5), α-Sexithiophene (T6) and N,N′-bis(n-octyl)-x:y, dicyanoperylene-3,4:9,10- bis(dicarboximide) (PDI8-CN2), grown on silicon oxide, have on cell viability, proliferation, shape, adhesion and morphology was carried on.

These particular molecules were chosen for their relevant properties, as they act as semiconductors and charge-carriers. Their first application is in Organic field-effect transistors (OFETs) and since they offer mechanical flexibility, tailored surface chemistry and high sensitivity to electrostatic potential changes at devices interface can be employed into implantable devices that allow to send electrical stimuli to neural cells. [2]

Scanning probe microscopies (SPM) derived from scanning tunneling microscopy (STM) offer a powerful tool to investigate biological samples and their response to specific surfaces. For the following work, atomic force microscopy (AFM) and scanning electrochemical microscopy (SECM) allowed a complete characterization throughout the optimization of the substrates and of cells as well as substrates after cell were grown on them. While AFM is the routinely used technique to characterize organic thin films morphology for its high spatial resolution, SECM adds the functional information of the reactivity of the sample and so it is highly indicated for the study of semiconductor surfaces as well as for morphological analysis of the samples for the assessment of the 3D shape of the cells on the analyzed substrate in physiological conditions. Furthermore, in our case the imaging resolution of SECM is increased by the feedback contrast of the cell with the

underlying material: fixed cells are usually less conductive than the materials on which they are attached, when a hydrophilic redox mediator is used.

In order to improve the possibilities of SECM, part of this work also regards the development of a new method for the miniaturization of a SECM tip. SECM resolution, as every SPM techniques, depends strongly on the size of the tip, thus a nanometer-sized tip would provide great advantages in this respect.

Typically, an electrode is classified as a nanoelectrode, if at least one dimension is smaller than 100 nm [3], although other definitions may be found.

A nanoelectrode instead of the standard ultramicroelectrode used as SECM working electrode, can be inserted into the cell without damaging the cell membrane, thus allowing the study of single organelles inside the cytosol, overcoming the limitations of conventional SECM and thus broadening the information obtainable by this technique. The intracellular concentrations of biological active molecules will be potentially determined and spatially localized using such new developed nano-electrodes.

References

1. Yao X., Peng R., & Ding J. (2013). Cell-material interactions revealed via material techniques of surface patterning. *Advanced Materials*, *25*(37), 5257–5286. http://doi.org/10.1002/adma.201301762
2. Cramer T., Chelli B., Murgia M., Barbalinardo M., Bystrenova E., de Leeuw D. M., & Biscarini F. (2013). Organic ultra-thin film transistors with a liquid gate for extracellular stimulation and recording of electric activity of stem cell-derived neuronal networks. *Physical Chemistry Chemical Physics : PCCP*, *15*(11), 3897–905. http://doi.org/10.1039/c3cp44251a
3. Cox, J. T., & Zhang, B. (2012). Nanoelectrodes : Recent Advances and New Directions. https://doi.org/10.1146/annurev-anchem-062011-143124

1. Introduction and Principles of Scanning Electrochemical Microscopy and Atomic Force Microscopy

Scanning Electrochemical Microscopy

Background

Scanning electrochemical microscopy (SECM) is a scanning probe microscopy (SPM) technique, which involves current measurements obtained by the use of a ultramicroelectrode (UME) (an electrode with an active radius, a, of the order of a few nm to 25 μm) when it is held or scanned in a solution in proximity to a substrate. Substrates can be solid (e.g. polymer, glass, metal, thin films, biological material) or liquid surfaces (e.g. mercury, oil), they cause a variation in the electrochemical response of the tip, from this alteration information is acquired, thus making possible to study the properties and nature of the sample. [1] The fine movements of the probe are achieved thanks to piezoelectric elements, in a similar fashion to others SPM techniques such as scanning tunneling microscopy (STM) and atomic force microscopy (AFM). Instead, the coarse movements are executed through stepper motors. Generally, the direction normal to the substrate is taken as the Z-direction, while X and Y are those in the plane of the substrate. [2] The main modes of operation of the SECM are generation/collection mode and feedback mode. The generation/collection mode can be tip generation/substrate collection (TG/SC), in which the product of the reaction taking place at the tip, is detected at the substrate. For example, when a species is oxidized at the tip, it will be reduced back at the substrate. TG/SC is particularly useful for the study of homogeneous reactions. Alternatively a substrate generation/tip collection (SG/TC) mode can be employed, where the species generated at the substrate are collected at the tip. SG/TC is suitable for studies of surface reactivity and was first used to study concentration profiles near an electrode surface without scanning and imaging. [3-5] In this work we used the most common mode of operation of the SECM, the feedback mode. In this mode only the tip current is monitored. The substrate reactivity influences the tip current once the tip gets closer to the surface. If the surface is conductive the current at the tip will be enhanced, vice versa it will be reduced. So this effect makes this technique capable of investigating both electrically insulating and conducting surfaces. It is particularly suitable to highlight changes in the reactivity among the scanned area, which was fundamental for this work. This mode of operation with surface imaging was first described along with the apparatus and theory, in a series of papers in 1989, [6-8]

Principles of SECM

A. Ultramicroelectrodes (UMEs)

The probes usually employed in SECM are UMEs. The UME we used is constituted by a 10 μm Pt wire sealed in a glass capillary under vacuum, connected with silver epoxy to a larger silver wire to allow the connection to the potentiostat. A fundamental characteristic is the shape of the tip, which can be a disk, a sphere, a cylinder or ring-shaped. The shape influences how the electro active species diffuses at the active area of the electrode. We used a disk electrode, the most common type. For a conductive disk of radius *a* in an insulating sheath, the steady state diffusion-controlled current for a reduction reaction

$O + ne \rightarrow R$ when the tip is far from a surface (**Fig. 1a**) is given by

$$i_{T,\infty} = 4nFDca$$

where D is the diffusion coefficient of species O, F is the Faraday, c the concentration of the species and n the number of electrons involved in the reaction.

The current at electrodes with other shapes, like cones or hemispheres, can be expressed in a similar way, but all the SECM experiments are carried out with disk-shaped electrodes, as they show the best sensitivity. [2] A key parameter to be considered for an UME is the radius of the insulating glass sheath, r_g. In literature is generally reported the $RG = r_g / a$ which has to be known since it influences the diffusion at the tip and consequently it is linked to the parameters needed in experimental data processing. The common UME used for this work has an RG of 10 (**Fig. 1b**).

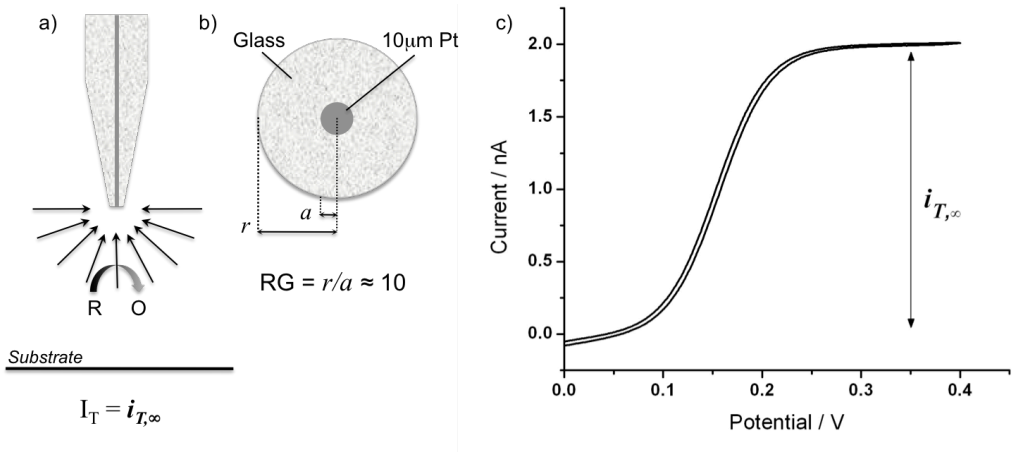

Fig. 1 a) Electrode behavior in bulk solution: the redox mediator reaches the tip by hemispherical diffusion. b) Frontal outline of the tip of a 10 μm Pt UME. c) Typical cyclic voltammogram for a 10mm Pt UME in PBS (pH 7.4) containing 1mM of FcMeOH. *E = 0÷0.4 V versus Ag/AgCl 3M KCl*. Scan rate = 10 mV/s.

The use of UMEs offers several advantages: first of all, since diffusion of the species to the ultramicroelctrode disk is hemispherical and as a consequence the diffusion layer is fixed, thin and geometrically controlled [2], the current is immune to convective effects and also independent from the radius of the insulating support. The UME reaches the steady state in a relatively short time, a fraction of a second in our case, as consequence the scanning probe can be treated as a steady-state system. Furthermore, due to the small currents characterizing SECM experiments (nA to pA or lower), the ohmic potential drops in solution is negligible as is the charging current of the double layer.[2] Lastly, owing to their small size, UMEs allow experiments in microscopic domains, similar to the dimensions typical of single living cells, that range from 20 to 100 μm.

B. Feedback mode

In **Fig. 2** the basic principles of feedback mode are shown. The tip is submerged in a solution containing a redox mediator, a species that can ben either in its oxidized or reduced state, these states must be completely reversible both chemically and electrochemically. The steady state current, $i_{T,\infty}$, mentioned earlier, is measured at the UME tip when it is far from the surface (**Fig. 2a**) the subscript, ∞, indicates this long distance. This distance is actually several tip diameters. In this condition the current is driven by the hemispherical diffusion of species from the bulk reaching the tip. When the tip approaches the surface in presence of a conductive substrate, such as a metal electrode (**Fig. 2b**), the substrate partially hinders the diffusion, but will also contribute to regenerate the redox mediator to its original state through electron transfer reaction with the redox mediator, thus enhancing the current at the tip, $i_T > i_{T,\infty}$. When the distance between the substrate and the tip approaches zero,the current, i_T, becomes very high owing to the fast regeneration regime.[2] Instead what happens when the tip is brought in proximity to an insulating substrate, commonly glass or plastic (**Fig. 2c**), is that this entirely blocks the diffusion of the redox species, so the closer the tip gets to the substrate, the smaller i_T becomes. When the distance, d, approaches zero, i_T approaches zero too.

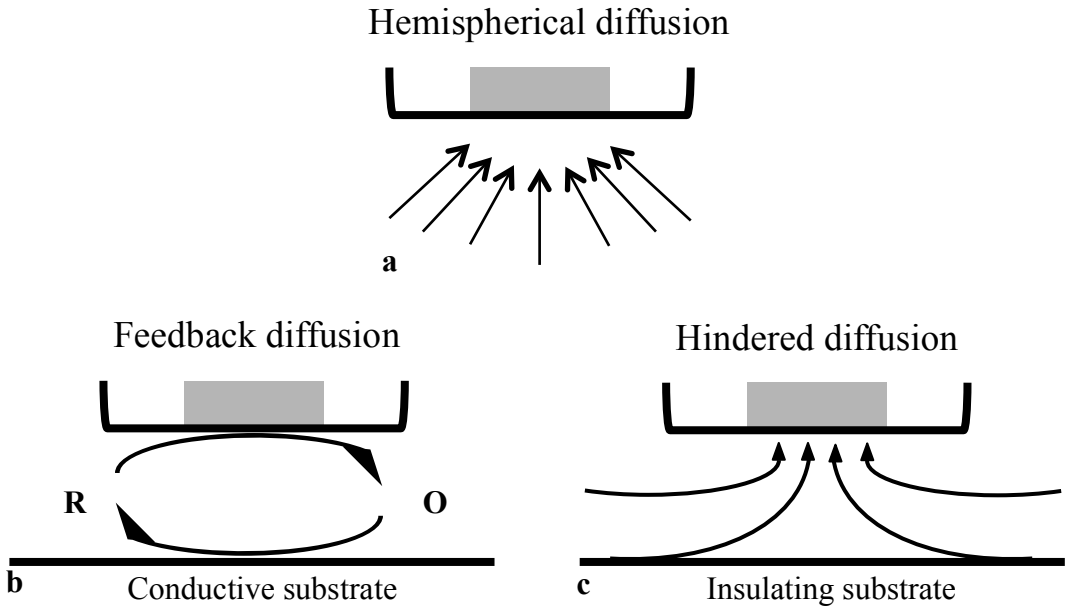

Fig. 2 Basic principles of SECM feedback mode: a) far from the substrate, diffusion leads to a steady-state current, $i_{T,\infty}$; b) near a conductive substrate, feedback diffusion leads to $i_T > i_{T,\infty}$; and c) near an insulating substrate, hindered diffusion leads to $i_T < i_{T,\infty}$.

Steady-state current-distance curves are called *approach curves* (ACs) (Figure 3), since the probe is moved along the z direction normal to the surface. The graph can be obtained by plotting $I_T = i_T / i_{T,\infty}$ versus $L = d/a$, both of them dimensionless quantities. When fitting experimental current-distance curves to theoretical equations the zero separation point ($L = 0$), has to be determined, which in turn allows one to establish the distance scale essential for any quantitative SECM measurement. The analytical expressions were numerically estimated by Mirkin and Bard, in function of several RG values[10]. The following theoretical equation fits within 1% the experimental current-distance curves for conductive substrates, over L interval from 0.04 to 10 and RG values between 1.1 to 10:

$$I_T^C(L) = \frac{i_T}{i_{T,\infty}} = k_1 + \frac{k_2}{L} + k_3 \exp\left(\frac{k_4}{L}\right)$$

where $L = d/a$ and k_1, k_2, k_3, and k_4 are parameters listed in Table 1. While, for an insulating substrate, the accuracy of the following equation is around 1% for $L \geq 2$ when RG = 1.11 and $L \geq 0{,}2$ for any other RG values present in **Table 2**:

$$I_T^{INS}(L) = \frac{i_T}{i_{T,\infty}} = \frac{1}{\left[k_1 + \frac{k_2}{L} + k_3 \exp\left(\frac{k_4}{L}\right)\right]}$$

Table 1. RG dependence on k_1, k_2, k_3, and k_4 for ACs under hindered diffusion control. [9]

RG	k_1	k_2	k_3	k_4	% Error	Validity Range
1002	0.13219	3.37167	0.8218	-2.34719	<1%	0.3-20
100	0.27997	3.05419	0.68612	-2.7596	<1%	0.4-20
50.9	0.30512	2.6208	0.66724	-2.6698	<1%	0.4-20
20.1	0.35541	2.02259	0.62832	-2.55622	<1%	0.4-20
15.2	0.37377	1.85113	0.61385	-2.49554	<1%	0.4-20
10.2	0.40472	1.60185	0.58819	-2.37294	<1%	0.4-20
8.13	0.42676	1.46081	0.56874	-2.28548	<1%	0.4-20
5.09	0.48678	1.17706	0.51241	-2.07873	<1%	0.4-20
3.04	0.60478	0.80683	0.39569	-1.89455	<0.2%	0.2-20
2.03	0.76179	0.60983	0.23866	-2.03267	<0.15%	0.2-20
1.51	0.90404	0.42761	0.09743	-3.23064	<0.7%	0.2-20
1.11	-1.46539	0.27293	2.45648	8.995E-7	<1%	2-20

Table 2. RG dependence on k_1, k_2, k_3, and k_4 for ACs under positive feedback control. [9]

RG	k_1	k_2	k_3	k_4	% Error	Validity Range
1002	0.7314	0.77957	0.26298	-1.29077	<0.2%	0.1-200
10.2	0.72627	0.76651	0.26015	-1.41332	<0.3%	0.1-200
5.1	0.72035	0.75128	0.26651	-1.62091	<0.5%	0.1-20
1.51	0.63349	0.67476	0.36509	-1.42897	<0.2%	0.1-200
10	0.68	0.78377	0.3315	-1.0672	<0.7%	0.05-20

Since approach curves involve only dimensionless variables, they do not depend upon the concentration or diffusion coefficient of the redox mediator. Instead, since the glass sheath covering the electrode hinders the redox mediator diffusion, the ACs shape depends upon RG. As shown in **Fig. 3** smaller RG values allow the electrode to get closer to the substrate.

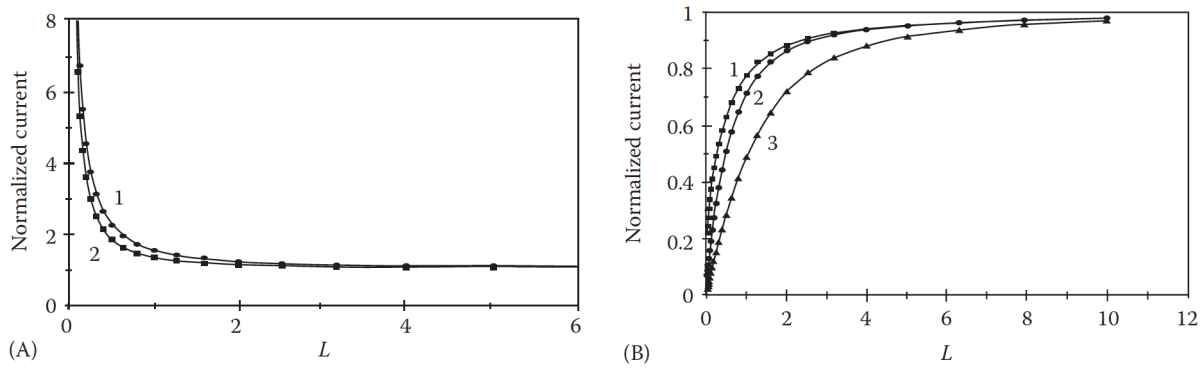

Fig. 3 Simulated SECM current vs. distance curves for a pure (A) positive and (B) negative feedback and different RG values. (A) RG = (1) 10 and (2) 1.1. (B) RG = (1) 1.1, (2) 2, and (3) 10. Reprinted from [10] Copyright 1998 American Chemical Society.

This is a great advantage, as it has been demonstrated that the dimensions obtained by SECM (*S*)

proved to be enlarged with respect to the real dimensions (S_0) with a dependence on the tip-surface distance and a formula describing this phenomenon has been obtained:

$$S = S_0 + 1.64d$$

The dependence on the distance arises from the lateral diffusion of the redox mediator, which becomes relevant as the distance increases, resulting in a reduced resolution. So the closest to the surface of the substrate the most accurate the image. Clearly if the tip and the substrate are not perfectly perpendicular, by getting closer to the surface an accidental contact could happen, with the risk of damaging the substrate or even worse breaking the probe.

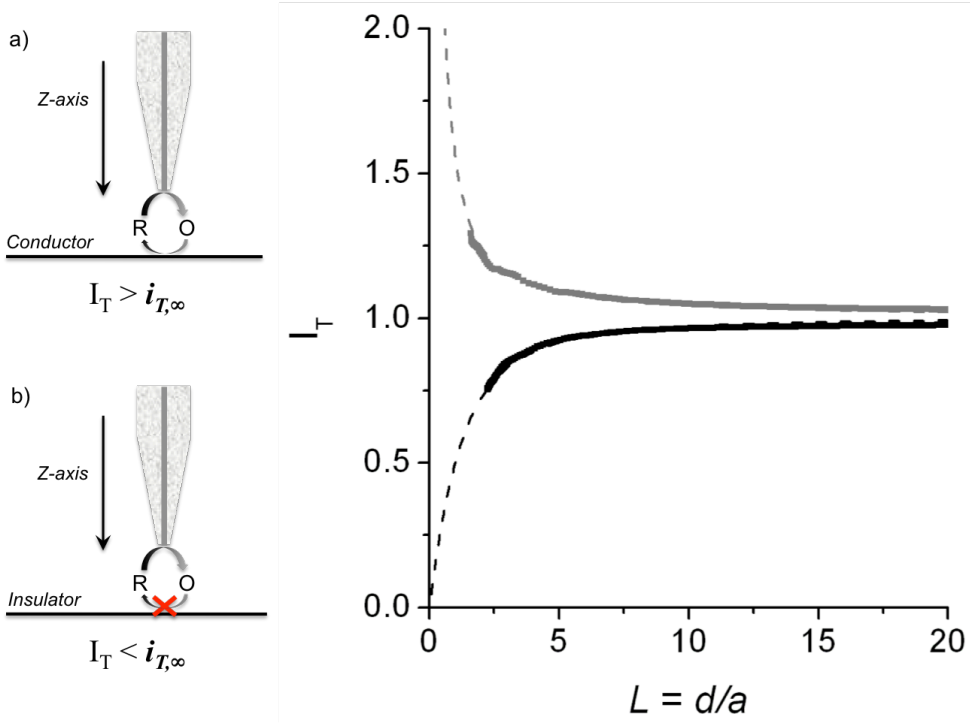

Fig. 4 Schematic representation of the probe movement along z axis toward a conductor material (a) and an insulating material (b). Experimental (dots) and theoretical (dashed lines) approach curves for a pure positive (grey) and negative (black) feedback obtained using 10mm Pt UMEs with a RG = 10. The measurements were performed in PBS (pH 7.4) containing 1mM of FcMeOH. *E = + 0.3 V versus Ag/AgCl 3M KCl.*

B. Generation/Collection Modes

Tip Generation/Substrate Collection (TG/SC)

In the tip generation/substrate collection mode, a species is generated at the tip, then diffuses across the distance, *d*, and reacts on the substrate surface (**Fig. 5a**). In this case both the current at the tip

i_T, and the current at the substrate i_S, are measured. In presence of a one-electron heterogeneous electronic transfer reaction, at the steady state those values are very similar ($i_S/i_T > 0.99$), for a $d \leq 2a$. This is because the substrate is considerably larger than the tip, so it the probability for the species to diffuse towards it is larger than to diffuse far from it. So the collection efficiency, given by i_S/i_T, is almost 100%, meaning that all the species generated at the tip is collected at the substrate. By contrast, homogeneous reactions coupled to electronic transfer have a different behavior and in this case it is possible to obtain important information on the kinetics. For example a tip generated species R reacts on transit from tip to substrate, i_S/i_T becomes smaller, and its change with separation, d, allows determination of the rate constant of the homogeneous reaction. In this case two situations arise:

1) The reaction is slow, the process is diffusion-controlled, the feedback is positive, then $i_S/i_T \approx 1$ at short distances.
2) The reaction is fast, most of the species R is converted to its inactive form before reaching the substrate, consequently $i_S/i_T \approx 0$.

In conclusion, to obtain information on the kinetics, the efficiency of the reaction at the substrate as function of d is measured.

Substrate Generation/Tip Collection (SG/TC)

In the SG/TC mode, at the tip is measured the current due to the product of the reaction occurring at the substrate. During a scan along z, the UME is brought in proximity of the substrate so that it gets through the diffusion layer, generated by the substrate, and measures the concentration profile as shown in **Fig.5b**. Scanning on the xy plane, it is possible to identify different reactive centers, characterized by different rate or reactions. In order not to perturb the diffusion layer at the substrate, the UME should be as small as possible, in this case nanometric electrodes can be employed to obtain a higher resolution. This method is less efficient than the TG/SC mode and presents some drawbacks: it is difficult to reach the steady state since the substrate is not micrometric, it is also complicated to control the tip-substrate distance and is highly sensitive to noise. Still this method proved very useful for monitoring corrosion, enzymatic reactions and others surface heterogeneous processes.

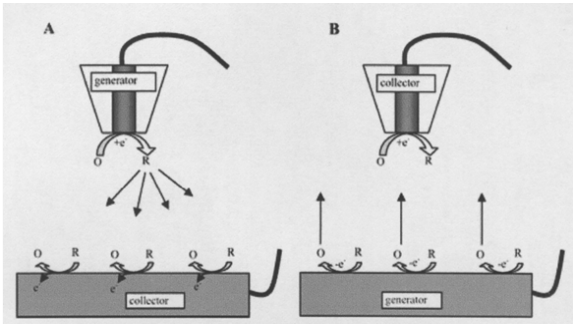

Fig. 5 Schematic representation of the tip generation/substrate collection (TG/SC) mode (a), and substrate generation/tip collection (SG/TC) mode (b).

Applications

This paragraph illustrates a wide range of applications of SECM that have appeared during the last years. Below, a general overview is provided, that might help to put the technique in perspective.

a) Imaging: by scanning the tip in x-y plane and measuring current changes, it is possible to obtain the topography of both conductive and insulating substrates. Of particular interest is the use of SECM to perform "chemical imaging", observing differences in reaction rates at different locations on the surface. This mode is very useful in studying biological materials (e.g. enzymes sites), and other surfaces. [2a]

b) UME shape characterization: by recording voltammograms and approach curves, recessed tips or tips with shape different than a disk can be identified. [2b]

c) *Homogeneous and heterogeneous kinetics measurements*: by measuring an approach curve or a voltammogram with the tip close to a substrate, one can investigate the electron transfer reactions rates at the electrode surface. Moreover, rate reaction constants of tip-generated species, as they diffuse between tip and conducting substrate, can be determined from steady-state feedback current or TG/SC experiments or by transient measurements. [2c]

d) Biological systems: there have been a number of applications of SECM to biological systems. These include imaging of living cells or tissues, studies of enzymatic reactions and investigation of transports of species through skin. [2d]

e) Reactions that occur on liquid/liquid interfaces, through membranes and thin films: by employing locally different electrochemical methods, one can study ion and electron transfer processes at the interface, the permeability of a membrane and the thickness of a film. [2e]

f) Reactions that occur at insulating and semiconductor surfaces: by following the current over time, it is possible to monitor rates of surface reactions, such as dissolution, adsorption and surface diffusion. [2f]

g) Owing to its ability to position the tip with high spatial resolution in three dimensions, SECM can be also used to probe *electrochemistry in very small volumes of solution* (3 ÷ 20 mL), and in thin liquid layers. [2g]

h) Fabrication; it is proved that SECM can be used also to carry out metal deposition, metal and semiconductor etching, local polymerization and others surface modification procedures with high spatial resolution. [2h]

SECM Imaging

It is possible to generate a three-dimensional SECM image in two ways: the first method is the *constant height mode*, where the tip is scanned in the x-y plane and fixed along the z axis and the current changes are measured in function of the UME location (*x,y,i*). Alternatively in the *constant current mode,* a value of current is fixed and the UME-substrate distance changes, necessary to keep the current constant, are measured in function of the probe location (*x,y,z*). [2a]

The resolution of such images is largely governed by the UME radius, *a*, and the distance between the probe and the sample, *d*. Smaller UME size and lower UME-sample operational distances increase the resolution of the image. The *constant current mode* is challenging to perform, because small electrodes are very delicate, and there might be irregularities in the sample surface, or a tilt of the substrate that can cause a "tip crash" during scanning. [11] In *constant height mode*, it is important to keep the probe at the right distance from the sample in order to avoid any kind of damage and still be close enough to be able to get information.

The Probe Approach Curve mode allows the working electrode to approach the surface of the substrate, and can be exploited for studying surface processes as well. The step dimension is automatically adjusted to permit fast surface approach for larger distances (by using stepper motors), whereas for finer z-control movements over short distances a piezoelectric positioner is used. The approach can be automatically stopped when a fixed percentage of the steady-state current is reached (we usually use 75%), in order to avoid crashing against the surface.

Probe Scan Curve mode controls the probe movement along x, y, and z direction, while the probe and substrate potentials are controlled and currents are measured. The rate of the UME movement has to be chosen in order to permit the reaction to take place at the electrode at steady-state during the scan. By using this mode, it is possible to measure ionic and redox species flows through membranes and investigate local transport properties and kinetic parameters of intracellular enzymatic redox processes, as for cellular respiration and metabolism.

SECM routinely offer μm resolution images of surface structures in bulk electrolyte solutions. AFM and STM commonly offer a better spatial resolution; however, SECM remains unique because,

beside topography, it provides also images of local chemical and electrochemical reactivity of surface features. Since its response is also related to the rates of the heterogeneous reactions at the substrate. In particular, it is useful in identifying and understanding functional aspects of several substrate structures, such as membranes, polymers, leaves, films and biological systems.

Setup

For this work, SECM measurements were carried out using an experimental setup where a 910B SECM (CHInstruments Inc., Austin, TX) and a Nikon Ti inverted microscope were coupled. The position system of the 910B CHInstrument was removed from the original stage and mounted on the plate of the inverted microscope. The modifications for this optical/electrochemical microscope were accomplished in house. This setup is very helpful to assist the UME movement along the axis during approaches, scan curves and imaging, to minimize the risks of damaging the UME. Furthermore, the optical microscope can be used to assess the morphology of the substrate or the scan area, particularly of a biological sample such as living cells. The positioning system is controlled by a computer, which is also used for data acquisition. A bipotentiostat controls the potential (range ± 10 V) at the tip and/or at the substrate versus the reference electrode and measures the tip and substrate currents. The bipotentiostat is able to record a broad range of currents (range ± 10 A), with a sensitivity ranging from pA or even lower to mA in the case of macroscopic substrates. [2] In order to achieve the best resolution when measuring signals as low as pA, a Faraday cage is fundamental to isolate the apparatus from any possible electrical noise and a vibration-free table is required to avoid environmental vibrations. The experiments were carried out in a 3,5 cm Petri dish, normally used for cell cultures, located on the inverted microscope plate holder, representing the electrochemical cell. The SECM probes (by CHInstruments) are 10 μm Pt ultramicroelectrodes with RG = 10. The tips were cleaned before use with alumina (0.05 mm) or diamond paper and sonicated in a bath sonicator for 10-20 seconds. The cell was also equipped with a Pt wire as counter electrode and a reference electrode Ag/AgCl (KCl 3M). The CHI900 software allows extensive experimental control and analysis of acquired data, whereas for data elaborations, statistics and computations OriginPro8.5 was utilized. The post processing of the bi-dimensional images was performed using the software MIRA, written by Wittstock[12] or using Gwyddion.
The apparatus just described is depicted in **Fig. 6**.

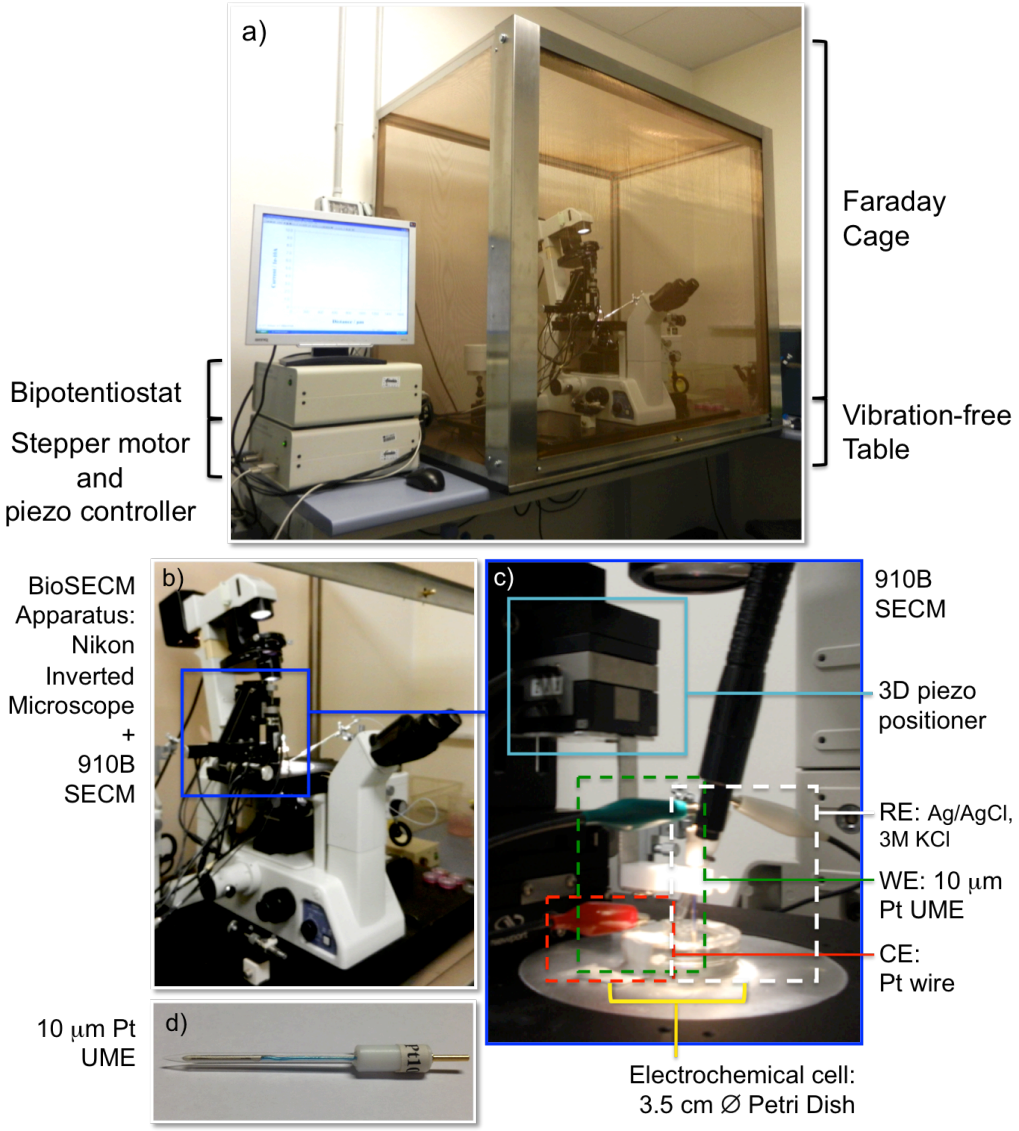

Fig. 6 SECM setup. a) SECM is mounted on the stage of a Nikon ECLIPSE 200 Inverted Microscope, on a vibration-free table inside a Faraday cage. b) Picture of the BioSECM apparatus. c) Part of the SECM components. Stepper motors and 3D piezo positioner (light blue square) that control the movement of the probe: 10 mm Pt UME (d), acting as WE (Working electrode). In the electrochemical cell (3.5 cm ∅ Petri dish) are allocated also the CE and the RE (Counter and Reference electrodes)

SECM OF BIOLOGICAL SYSTEMS

In the last thirty years SECM-based methods have been developed to deal with charge transfer reactions in biological systems, such as immobilized enzymes [12] and cell processes [13,14]; map cellular redox activities [15-17] and cellular metabolism, and image the topography of biological specimens or biomolecules.[18,19] The reasons why SECM is ideal to investigate biological systems are mainly two: i) to begin, with SECM measurements can be carried out directly in cell culture media and also in buffered solutions, environments suitable for most biological samples; ii)

secondly SECM is a non-contact mode SPM technique, which consent to obtain information from the samples without damaging it.

SECM OF SINGLE LIVING CELLS

SECM is a powerful technique for investigating living cells thanks to the variety of species that can be detected with an appropriate selection of the working electrode. This technique proved to be sensitive, able to give a quantitative response, not invasive and capable of good resolution in terms of time and space.[2d] The types of experiments generally conducted on living cells are generation/collection and amperometric feedback mode measurements [1]. These methods require the positioning of the probe in proximity of the substrate of interest. The electrode is positioned at a known distance *d* from the bottom of the plastic Petri dish where cell were cultured at low density (to allow single cell measuring without any interference by neighboring cells), by using probe approach curves. In this case the feedback is negative, due to the insulating plastic dish. The majority of SECM profiles and images of living cells reported in literature [15,11,20], were obtained in constant height mode that is scanning the UME in the x-y plane at a fixed value of z above the surface. Through SECM measurements it is possible to map the redox reactivity of a cell [15-17], image the cell topography by positive or negative feedback behavior, [19,21] ATP [22] and other metabolites like oxygen reactive species (ROS), nitrogen reactive species (NOS) or glucose and lactate [23] across the cell membrane. Working in constant height mode, many issues arise because of the variety of dimensions found within a sample of cells of the same kind. Since some cells are bigger than others, it is difficult to obtain highly resolved images without damaging some of them or, at the same time, missing or obtaining low-resolution images of the flatter ones. A possible remedy for this inconvenient is to scan the surface at a distance with a small percentage of negative feedback, allowing a good imaging capability and a relatively large distance between the probe and the dish. Another possible procedure is to scan small areas.

Cellular redox reactivity can be studied using feedback mode. SECM can monitor the release of redox species from living cells, or the interaction of redox mediators with living cells providing information on cellular metabolism and/or topography. In the case of a redox mediator not interacting with the cell, the current decreases approaching the living cell, giving a negative feedback. [16] In this way the cellular topographic contribution can be finely mapped for every SECM measurements. By contrast, if a cellular component is able to regenerate the redox species to its pristine form, the current recorded will increase when approaching the cell, leading to a less negative feedback. [24] The electrochemical signal reflects the thermodynamic equilibrium interesting the interaction of the mediator with all the cell redox components. For example, the

analysis of cellular redox balance is used to quantify the changes of redox species associated to oncogene expression and malignant phenotypes. [24] Generation/collection mode instead is employed in experiments that aim to measure electroactive species, directly or indirectly produced or consumed by the cell.

One of the main examples of the use of SG/TC mode in cell analysis is the study of the respiratory activity of a single cell [17], where the oxygen gradient near the cell surface is measured. [19,24] There is also the possibility to monitor different redox species, like the ones involved in the electron transport chain. [22,23] Many research groups investigated oxygen consumption in a variety of living systems and cells. By measuring the rate of oxygen consumption, some authors addressed a number of biomedical problems, ranging from drug sensitivity of cancer cells [25] to the viability of bovine embryos [26] and mitochondrial respiration in neuronal cells.[20]

Another field where SG/TC mode is often applied is the study of cellular metabolism at single cell level, by probing the gradient concentration of metabolites such as ATP [22], ROS and NOS, close to the cell surface.

It is also possible to perform electrochemical acquisition within an immobilized cell or within "artificial cells". [27] In this case the main obstacle is presented by the size and geometry of the probe, which could damage the cell membrane after puncturing it. [28] Thus, in order to perform spatially resolved intracellular measurements, the use of a nanoelectrode is highly recommended. This was the case of the experiment shown in **Fig. 7**, where authors were able to determine the mass and charge transfer rates of redox species across the cell membrane, the membrane potential and the redox properties of a living cell, with nanometric resolution. Since the thickness of the diffusion layer is equal to a few tip radii, a nanoprobe is able to sense only local electrochemical properties in a sub-micrometer or nanometer-sized domain. [27]. It is thus clear that a nanoprobe allows to investigating the local redox environment, without the amplified response deriving from the subcellular compartments all together.

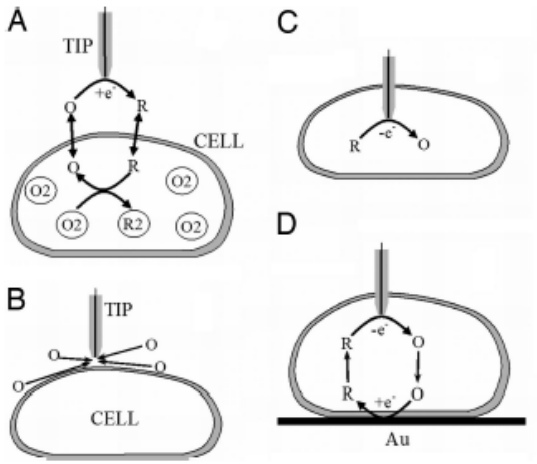

Fig. 7 SECM experiments at single cell level. a) The tip is placed in solution close to the cell surface. Positive feedback occurs through the bimolecular electron transfer between the hydrophobic redox mediator (O/R) and the redox charges inside the cell (O2/R2). b) The impermeability of lipid cell membrane for a hydrophilic redox mediator is shown; thus a negative feedback arises since the diffusion of redox species to the probe is prevented. c) A nanoelectrode voltammetry inside the cell is represented. d) A positive feedback occurs after the redox mediator regeneration by means of electron transfer from the underlying Au electrode. [27]

Atomic Force Microscopy

Ex-situ Atomic Force Microscopy measurements

Atomic Force Microscopy (AFM) was used to perform morphological characterizations of both MLs and deposition steps (see chapter 2). The AFM head (Smena, NT-MDT) [29] is placed within an acoustic case equipped with a spring isolation frame to reduce as much as possible any type of noise sources. An optical microscope (visible in **Fig.8**) is used to it can be used to place the cantilever in the right place of the sample.

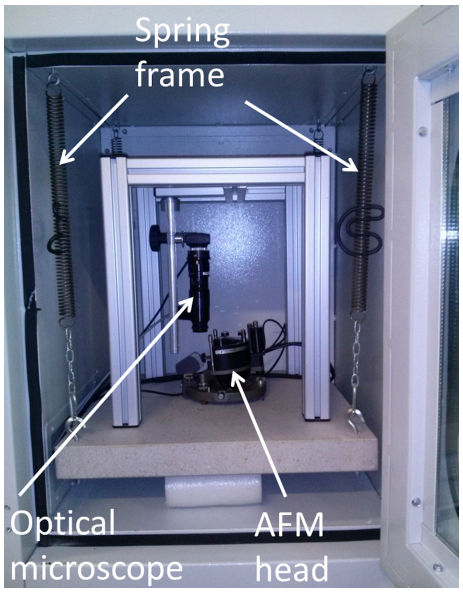

Fig. 8 The NT-MDT Smena Measurement Head, the spring isolation frame and the optical microscope.

General scheme of an AFM Smena head

The general view of the Smena Measurement Head is shown in **Fig. 9**. The base (1) is installed on three adjustable supports (2 a,b). The base accommodates a scanner (3) with a probe holder (4), a tracking and detection device (5 a,b) and an electronic circuit board (6). The cantilever is installed into the holder (4).

Supports

Adjustable height supports (2 a,b) are used for setting up the horizontal and the height position of the MH with regard to the analyzed sample. The tip and the sample should be as much perpendicular as possible, this is achieved manually selecting the three height supports. A tilting angle too big between the tip and the sample can strongly affect the quality of the AFM image. The rear support (2 b) is used for approaching the probe to the sample by changing the inclination of the head. This is a 0.35 mm pitch thread screw. Rotation of this screw by 1° results in changing the cantilever vertical position with regard to the sample by 0.3 microns, this allows an easy manual approach of the probe.

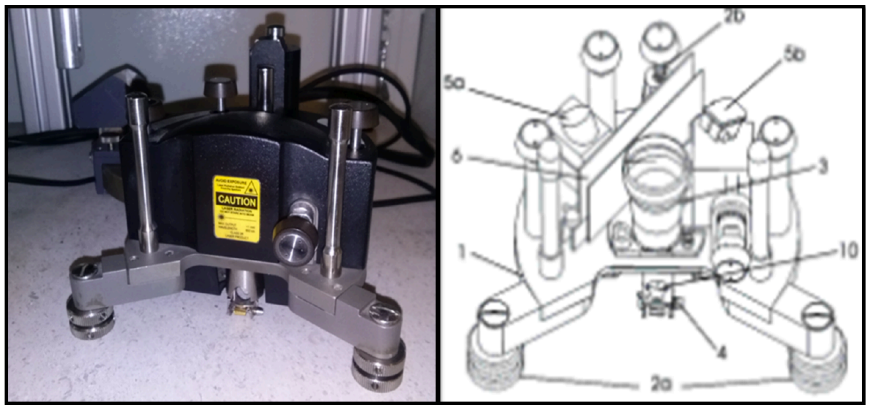

Fig. 9 Main parts of the Smena Measurement Head. [29]

AFM main components

Scanner

The scanner is designed for the probe movement in the x,y and z directions. It consists of 2 concentric piezotubes, one inserted into the other, which are connected at one end. The outer tube ensures the probe displacement along axis z, the inner tube provides for movement in plane x-y. The free end of the inner piezotube, has the cantilever holder and the scanning mirror attached. This mirror is the primary sensing device of the cantilever laser tracking system.

Cantilever Holder

It consists in a spring clamp. It also has a piezodrive for exciting the cantilever at its resonant frequency.

Optical Detection System

To measure the cantilever movements, an AFM incorporates a laser with focusing lenses, a mirror system and a photodetector with a magnifying glass, as depicted in **Fig. 10**.

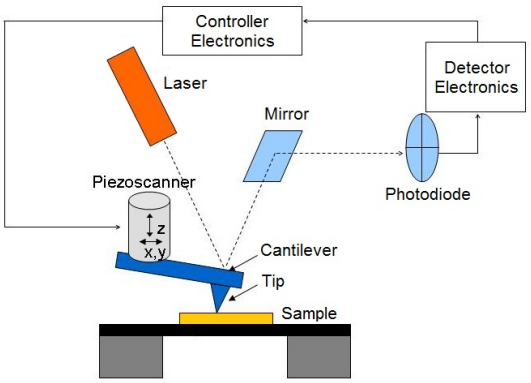

Fig. 10 Tracking and detection device.

A laser beam is focused to a spot on the back of the cantilever, its reflective surface reflects the beam via a mirror onto a photodiode. This works as an optical lever, since minute displacements of the cantilever, become large light movements on the photodiode. The major advantages in this system are that since very small deflections of the cantilever are amplified, they can be detected by the photodiode and that it is quite simple to build. The laser beam is reflected onto a photodetector divided in four quadrants, where it is converted into an electronic signal. Bending of the cantilever varies according to different interactions with the sample. Specifically, the difference in signal acquired by the two top and the two bottom areas of the photodiode will give the vertical deflection of the cantilever, while the difference between the two quadrants on the right and the two on the left will give the lateral torsion.

The optical lever AFM force sensor requires alignment every time the tip is changed. Alignment is usually achieved by directing the laser beam onto the back of the cantilever first, and then by checking the signal at the photodetector, ensuring that the light is centered on the photodiode.

Tapping Mode

In AFM tapping mode, the cantilever is oscillated in the range 1-100 nm [30], typically at its resonant frequency by using a piezoelectric crystal. When the tip approaches the surface, the oscillation is subjected to a variation in amplitude, frequency and phase shift, any of this information can be exploited to investigate the surface and different sample properties. The effect on the oscillation is a reduction of both amplitude and frequency upon contact to the surface [31] as is visible in **Fig. 11**. The tapping mode is effective in case of compounds easily deteriorated and of species not firmly attached to the underlayer, since it substantially reduces the sample damage.

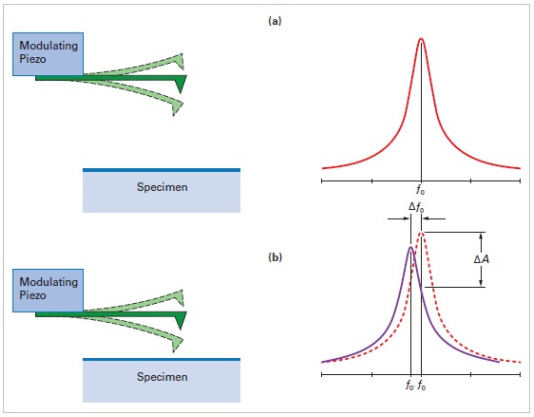

Fig. 11 Resonance curve of a tapping mode cantilever above and close to the surface. The resonance shifts to lower frequencies and exhibits a drop in amplitude. [31]

The effects on oscillation are monitored by the force transducer, while the z scanner adjusts the z height via the feedback loop, so that a constant distance from the surface is maintained. Below (**Fig. 12**) the resulting curve of attractive forces (van der Waals interactions) and repulsive forces (short range Coulomb interaction) is shown. [31]

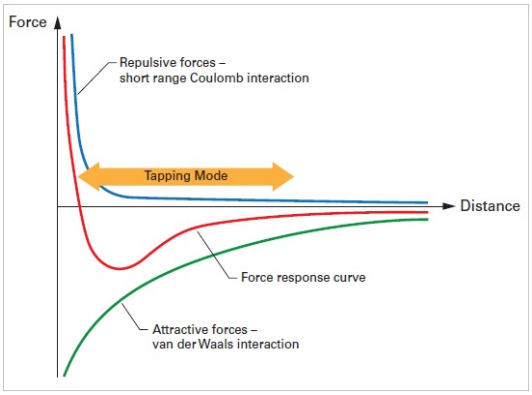

Fig. 12 Force curve showing the motion of a cantilever during tapping mode. [31]

Since large oscillation amplitude is applied, the probe moves from being far from the surface where there is no tip-sample interaction, through the attractive regime, into the repulsive regime, and back, this for every oscillation cycle. The AFM in tapping mode oscillates back and forth on this curve and an average response of various interactions is reported. For example, if the sample is composed of different regions with different properties, for instance polymers incorporating more rigid nanoparticles, when the tip scans the surface swaying, from an area to another a variation in the amplitude module is observed and the resonance may shift, in the lower frequencies. Since the amplitude of the oscillation is kept constant through a feedback loop, if the zone scanned by the tip has a protrusion the cantilever has less space to sway, so it diminishes the amplitude. On the contrary if the tip passes over a depression zone, the amplitude is increased. This technique is very popular as it combines the lower possibility of sample damage if compared to contact mode, the fact that in this technique lateral forces (experienced by the sample and the tip during contact mode) are almost eliminated and the higher stability in air with respect to non-contact mode.

Lastly, the performance parameters of the NT-MDT Smena Measurement Head are reported.

Scanning Range	90x90x5 μm
Minimum Scanning Step	0.01 nm

Sample Size	unlimited
Overall Dimension	115x130x100 mm
Weight	0.7 kg

References

1. (a) Sun P, Laforge FO, Mirkin MV, Scanning Electrochemical Microscopy in the 21st century. *Phys. Chem. Chem. Phys*. 9, pp. 802-823 (2007) (b) Mirkin MV, Nogala W, Velmurugan J, Wang Y, Scanning Electrochemical Microscopy in the 21st century. Update 1: five years after. *Phys. Chem. Chem. Phys*. 13, pp. 21196-21212 (2011)
2. Bard AJ, Introduction and principles (Chapter 1). *Scanning Electrochemical Microscopy*. Bard AJ, Mirkin MV (Eds.), Marcel Dekker, New York (2001) (a) Fan F-RF, SECM Imaging (Chapter 4), (b) Mirkin MV, Theory (Chapter 5), (c) Borgwarth K, Heinze J, Heterogeneous electron transfer reactions (Chapter 6) – Unwin PR, Kinetics of homogeneous reactions coupled to heterogeneous electron tranfer (Chapter 7), (d) Horrocks BR, Wittstock G, Biological System (Chapter 11), (e) Mirkin MV, Tsionsky M, Charge-Transfer at the liquid/liquid interface (Chapter 8), (f) Bath BD, White BH, Scott ER, Imaging molecular transport across membranes (Chapter 9), (g) Macpherson JV, Unwin PR, Probing reactions at solid/liquid interfaces (Chapter 12), (h) Mandler D, Micro- and nanopetterning using the scanning electrochemical microscope (Chapter 13).
3. Engstrom, R. C., Weber, M., Wunder, D. J., Burgess, R., Winquist, S. Measurements within the diffusion layer using a microelectrode probe. Anal. Chem. 1986, 58, 844.
4. Engstrom, R. C., Meaney, T., Tople, R., Wightman, R. M. Spatiotemporal description of the diffusion layer with a microelectrode probe. Anal. Chem. 1987, 59, 2005.
5. Engstrom, R. C., Wightman, R. M., Kristensen, E. W. Diffusional distortion in the monitoring of dynamic events. Anal. Chem. 1988, 60, 652.
6. Bard, A. J., Fan, F.-R. F., Kwak, J., Lev, O. Scanning electrochemical microscopy. 1. Introduction and principles. Anal. Chem. 1989, 61, 132.
7. Kwak, J., Bard, A. J. Scanning electrochemical microscopy. 2. Theory of the feedback mode. Anal. Chem. 1989, 61, 1221.
8. Kwak, J., Bard, A. J. Scanning electrochemical microscopy. 4. Apparatus and two-dimensional scans of conductive and insulating substrates. Anal. Chem. 1989, 61, 1794.
9. (a) Sun P, Laforge FO, Mirkin MV, Scanning Electrochemical Microscopy in the 21st century. *Phys. Chem. Chem. Phys*. 9, pp. 802-823 (2007) (b) Mirkin MV, Nogala W, Velmurugan J, Wang Y, Scanning Electrochemical Microscopy in the 21st century. Update 1: five years after. *Phys. Chem. Chem. Phys*. 13, pp. 21196-21212 (2011).
10. Shao, Y. and Mirkin, M.V., Probing ion transfer at the liquid/liquid interface by scanning electrochemical microscopy (SECM), J. Phys. Chem. B, 102, 9915–9921, 1998.

11. Takahashi Y, Shevchuck AI, Novak P, Babakinejad B, Macpherson J, Unwin PR, Shiku H, Gorelik J, Klenerman D, Korchev YE, Matsue T, Topographical and electrochemical nanoscale imaging of living cells using voltage-switching mode scanning electrochemical microscopy. *PNAS*. 109:29, pp. 11540-11545 (2012)
12. http://www.wittstock.chemie.uni-oldenburg.de/gunther.wittstock/en/index.html
13. Kurulugama RT, Wipf DO, Takacs SA, Pongmayteegul S, Garris PA, Baur JE, Scanning electrochemical microscopy of model neurons: constant distance imaging. *Anal. Chem*. 77, pp. 1111-1117 (2005)
14. (a) Liu B, Cheng W, Rotenberg A, Mirkin MV, Scanning electrochemical microscopy of living cells. Part 4. Mechanistic study of charge transfer reactions in human breast cells. *Anal. Chem*. 74, pp. 6340-6348 (2002) (b) Liu B, Cheng W, Rotenberg A, Mirkin MV, Scanning electrochemical microscopy of living cells. Part 5. Imaging of fields of normal and metastatic human breast cells. *Anal. Chem*. 75, pp. 4148-4154 (2003)
15. Liu B, Rotenberg SA, Mirkin MV, Scanning Electrochemical Microscopy of living cells: different redox activities of nonmetastatic and metastatic human breast cells. *PNAS*. 97:18, pp. 9855-9860 (2000)
16. Liu B, Cheng W, Rotenberg A, Mirkin MV, Scanning electrochemical microscopy of living cells. Part 2. Imaging redox and acid/basic reactivities. *J. Electroanal. Chem*. 500, pp. 590-597 (2001)
17. (a) Yakusawa T, Kondo Y, Uchida I, Matsue T, Imaging of cellular activity of single cultured cells by scanning electrochemical microscopy. *Chem. Lett*. pp. 767-768 (1998) (b) Kaya T, Torisawa Y, Oyamatsu D, Nishizawa M, Matsue T, Monitoring the cellular activity of a cultured single cell by scanning electrochemical microscopy (SECM). A comparison with fluorescence viability monitoring. *Biosensors and Bioelectronics*. 18, pp. 1379-1383 (2003) (c) Yakusawa T, Kaya T, Matsue T, Imaging of photosynthetic and respiratory activity of a single algal protoplast by scanning electrochemical microscopy. *Chem. Lett*. pp. 975-976 (1999)
18. Yakusawa T, Kaya T, Matsue T, Dual imaging of topography and imaging of photosynthetic activity of a single protoplast by scanning electrochemical microscopy. *Anal. Chem*. 71, pp. 4637-4641 (1999)
19. Schulte A, Nebel M, Schuhmann W, Single live cell topography and activity imaging with the shear-force-based constant-distance scanning electrochemical microscope (Chapter 12). *Methods in Enzymology*. Vol. 504, ©Elsevier Inc. (2012)

20. Takii Y, Takoh K, Nishizawa M, Matsue T, Characterization of local respiratory activity of PC12 neuronal cell by scanning electrochemical microscopy. *Electrochim. Acta*. 48, pp. 3381-3385 (2003)
21. Nebel M, Grützke S, Diab N, Schulte A, Schuhmann W, Microelectrochemical visualization of oxygen consumption of single living cells. *Faraday Discussion*. 164:19, pp. 19-32 (2013)
22. Schulte A, Nebel M, Schuhmann W, Single live cell topography and activity imaging with the shear-force-based constant-distance scanning electrochemical microscope (Chapter 12). *Methods in Enzymology*. Vol. 504, ©Elsevier Inc. (2012)
23. Ciobanu M, Taylor DE Jr, Wilburn JP, Cliffel DE, Glucose and lactate biosensors for scanning electrochemical microscopy imaging of single live cells. *Anal. Chem*. 80, pp. 2717-2727 (2008)
24. Nebel M, Grützke S, Diab N, Schulte A, Schuhmann W, Visualization of oxygen consumption of single living cells by scanning electrochemical microscopy: the influence of the faraic tip reaction. *Angew. Chem*. 52, pp. 6335-6338 (2013).
25. Y-S Torisawa, Kaya T, Takii Y, Oyamatsu D, Nishizawa M, Matsue T, Scanning electrochemical microscopy – based drug sensitivity test for a cell culture integrated in silicon micro-structures. *Anal. Chem*. 75:9, pp. 2154-2158 (2003)
26. Shiku H, Shiraishi T, Ohya H, Matsue T, Abe H, Hoshi H, Kobayashi M, Oxygen consumption of single bovine embryos probed with scanning electrochemical microscopy. *Anal. Chem*. 73, pp. 3751-3759 (2001)
27. Sun P, Laforge F. O., Abeyweera T. P., Rotenberg S. A., Carpino J., and Mirkin M. V., Nanoelectrochemistry of mammalian cells. *PNAS January 15, vol. 105 no. 2 443–448* (2008)
28. Zhan W, Bard AJ. Scanning electrochemical microscopy. 56. Probing outside and inside single giant liposomes containing $Ru(bpy)_3^{2+}$, *Anal Chem* 78:726–733 (2006)
29. http://ntmdt.com
30. Garcia R. and Perez R., *Surface Science Reports*, 47, 197 (2002)
31. http://www.azonano.com/article.aspx?ArticleID=3010. Fundamentals of Contact Mode and TappingMode Atomic Force Microscopy. Sponsored by Bruker Nano Surfaces (2012)

2. Organic Monomolecular Layer Fabrication

Organic Molecular Beam Epitaxy on Silicon Oxides Substrates

To functionalize Silicon oxides substrates with organic molecules, a High-Vacuum system (HV, Base pressure $2 \cdot 10^{-8}$ mBar) capable to sublimate small organic molecules has been exploited (**Fig. 1 a**). The HV system is composed by two vacuum chambers, a Fast Entry Lock (FEL) and an Organic Chamber (OC), separated by a vacuum gate. Both chambers are evacuated by two separated pumping systems composed by a primary pump (from ambient pressure to 10^{-2} mBar) and a turbo-molecular pump (from 10^{-2} to 10^{-9} mBar). The OC chamber is kept constantly at the lower possible pressure ($2 \cdot 10^{-8}$ mBar), while the FEL has used for introducing substrates from ambient pressure to the OC. In particular, the FEL is pumped down to low10^{-7} mbar prior opening the gate valve in order to introduce a new substrate into the OC chamber. The sample transfer from the FEL to the OC is possible by means of a linear vacuum manipulator.

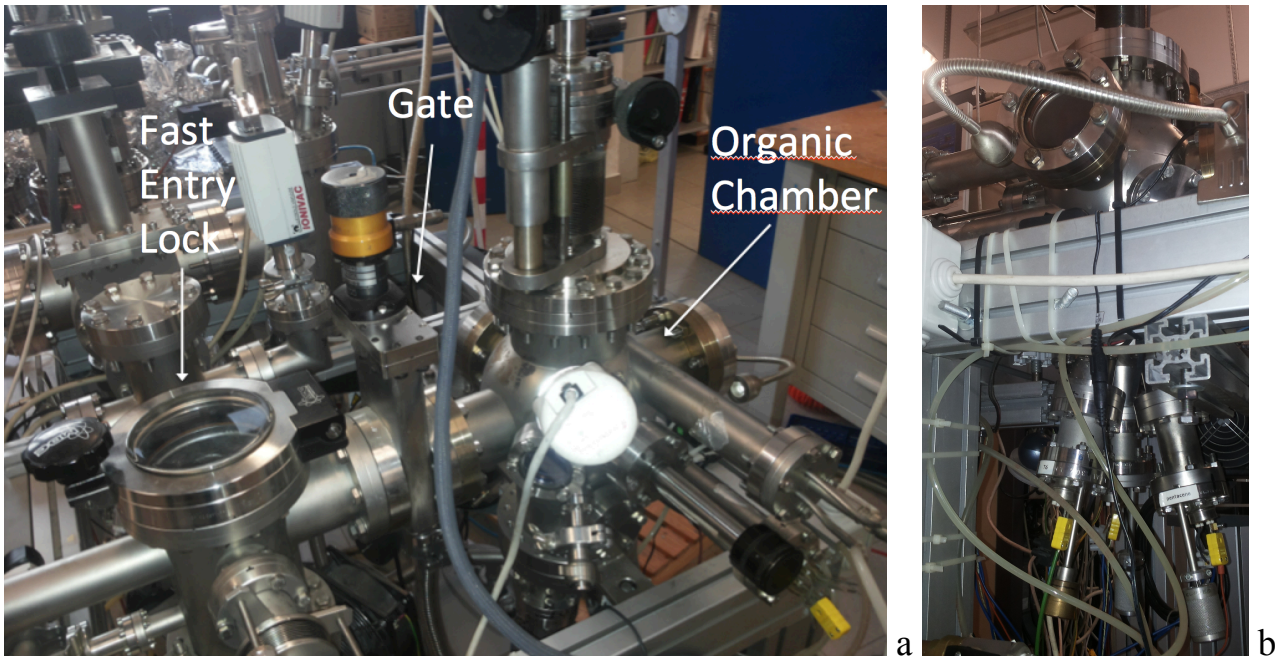

Fig. 1 a) UHV system composed by the FEL and the organic chamber, separated by a vacuum gate. **b)** Organic Emission Cells situated below the organic chamber.

Three Knudsen cells (KC) are placed in the bottom part of the organic chamber, each one loaded with three different molecules, and their azimuthal axis converge on the sample surface (**Fig. 1 b**). Briefly, Knudsen cell are composed of a heated crucible filled by the organic powder. When the KC

temperature reaches about 200°C (but this temperature depends on the molecular weight), the powder sublimates passing from solid state to vapor phase. Due to the low pressure and the small aperture of the KC crucible, a molecular vapor expands in the volume of the OC following a spherical cap (molecular flux). The KC is equipped with a shutter to stop the molecular flux, as well as the sample that has a shutter to protect the sample surface. Close to the sample, there is a Quartz Crystal Microbalance (QCM) to measure the amount of deposited molecules (in ng). When the sample shutter is retracted, the molecular vapor can reach the substrate surface, and molecules are absorbed physically on it to form a continuous molecular film.

Organic Mono-molecular Layers Fabrication

General procedure

Our aim was to form a highly ordered single layer (monolayer, ML) of molecules. Experiments were carried out by using the organic chamber previously described for sublimating three different molecules, namely α-Sexithiophene (6T) and Pentacene (P5) – purchased from Sigma-Aldrich – and N,N'-bis(n-octyl)-dicyanoperylene-3,4:9,10-bis dicarboximide (PDI8-CN2) – purchased from Polyera Corporation. As reported in the paper [1] a monolayer is effectively organized by exploiting a post-annealing process. In reason of that, the substrate is heated (thermal radiations) at a certain temperature (T_{sub}) measured by means of a thermocouple previously calibrated. Prior the molecular deposition, samples were kept one hour at their respective target temperature, in order to both assure a homogeneous sample temperature and degas the solvent from the silver paste.

All substrates, i.e. squared wafer fragments of Si coated with native silicon oxide, were manually cut from the same wafer (p-type, boron doped, resistivity 5-10 Ω-cm), glued to the sample holder using silver paste for having a good thermal contact. Such operation are performed in a laminar flow hood and then they are immediately introduced in the FEL without further treatments to limit as much as possible the surface contamination. Once transferred in the OC, the sample holder was fixed on a movable holder that is lifted in a fixed position (i.e. 3.97 cm) kept constant for all the experiments performed.

After deposition, samples were cooled down to RT and, lastly, they are transferred to the FEL. Monolayers were morphologically characterized by *ex-situ* Atomic Force Microscopy (AFM) experiments, performed in air by an NT-MDT Smena AFM microscope operating in semi-contact mode. To avoid film damages, soft cantilevers (NSG10, NT-MDT) were used.

Evaporation experimental procedure

- The KC temperature (T_{cell}) is kept constantly to 100°C for reducing the powder contamination. Before deposition experiments, T_{cell} is raised to 180° C overnight for degassing more impurities.
- The sample holder, with the sample fixed with Ag paste, is mounted on the linear manipulator in the FEL that is then pumped down to 10^{-7} mbar. This operation usually takes around three hours.
- During this time, T_{cell} is gradually raised every hour up to reach the sublimation temperature. The Knudsen cell shutter is closed. The steel gate separating the FEL and the OC can be opened when the FEL pressure reaches 10^{-7} mBar, which is comparable to OC vacuum (~10^{-8} mBar).
- With the two chambers in communication the sample holder can be transferred inside the organic chamber and locked with the sample facing down towards KCs. The manipulator is then retracted and the gate closed.
- If substrate temperature was different than room temperature, the sample was heated and 1 hour was waited after reaching the target T_{sub}, in order to have a homogeneous temperature on the surface substrate. At this time, the sample shutter is closed.
- The shutter of the KC was opened and the molecular flux measured by the QCM. The flux (in ng/min) was monitored for 10-15 minutes in order to stabilize it.
- When the molecular flux is stable, the sample shutter was opened, and the deposition process starts.
- To form a highly ordered ML, 150ng of molecules (as measured by QCM) were deposited in three steps of 50 ng each, followed by one hour of post-annealing (namely partial annealing). In the post-annealing process both KC and sample shutters were closed, and the substrate is kept at T_{sub}. When the target amount of molecules was reached, both KC and sample shutter were closed, while T_{cell} and T_{sub} were cooled down to 100° C and RT, respectively.
- When T_{sub} reaches RT, the gate is opened and the sample holder was transferred back to the FEL, where the sample was brought to ambient pressure.

Materials: molecules

α-Sexithiophene (6T)

Sexithiophene also known as α-hexathiophene, α-hexathienyl or α-sexithienyl has the chemical formula $C_{24}H_{14}S_6$ and a melting temperature of 290° C at normal condition. It belongs to the class of p-type organic semiconductors. This molecule belongs to the class of oligothiophenes: conjugated organic molecules of different chain-length with a five membered sulphur ring containing aromatic compound as smallest unit (see **Fig. 5**). Oligomers of this monomer unit bonded by σ bonds via its α-carbons are termed α-*n*T where *n* stands for the number of subunits of the respective oligothiophene.

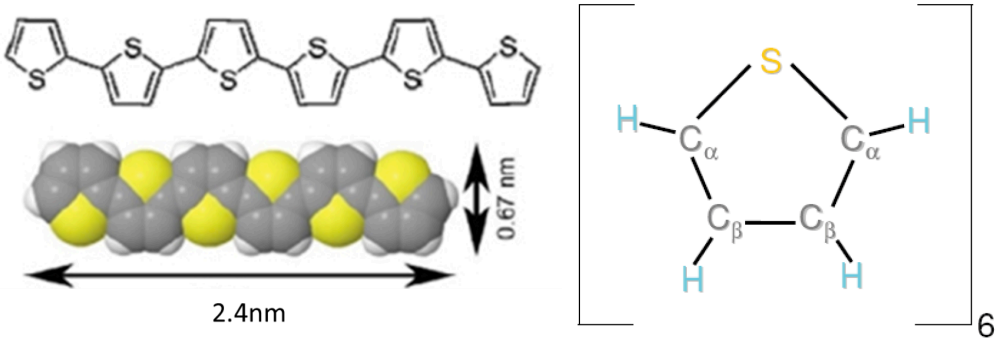

Fig. 4 6T molecule structure composed of six conjugated aromatic rings and relative dimensions. (right) Thiophene monomer with the atomic nomenclature for the carbon atoms. The alternative name α-6T underlines the linking of the monomer subunits through the C_α atoms. (left).

6T has been strongly studied as the first organic semiconductor for its rigid-rod behavior and its morphological properties that made it to be used for the first OFET employing a small conjugated molecule.[2] Due to its peculiar self-organization and transport properties it is considered a prototype for studying the physics of molecular devices. It can be obtained as a pure material, and it is processed as thin film sublimated in high vacuum conditions. On dielectric surfaces, like silicon oxide, 6T molecules adsorb in a standing orientation, namely with the long molecular axis almost normal to the substrate.

Pentacene (P5)

Pentacene is a molecule composed by five polyaromatic fused rings that form a rod like shape structure. This highly conjugated compound is a p-type organic semiconductor. Pentacene has been

thoroughly investigated as material of choice for OTFTs and OFETs, owing to one of a high application potential thanks to its high performances in OFETs better than those of amorphous silicon.[3,4] Pentacene based OFETs have been employed as transducer and electrical stimulators of neuronal network activity by Cramer et al. [5], who showed that this material enables good cellular adhesion and efficient coupling of the ionic currents at the biological-organic semiconductor interface with the OFET current.

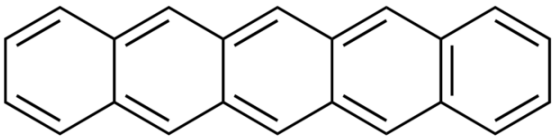

Fig. 5 Sketch of the 5 units long polyacene pentacene.

Perylene (PDI8-CN2)

The perylene derivate N,N'-bis(n-octyl)-dicyanoperylene-3,4:9,10-bis dicarboximide (PDI8-CN2) is a new generation n-type semiconductor with a rigid core in contrast to the rodlike shape of Sexithiophene and Pentacene. It is a perylene derivative having two cyano groups directly bond to the aromatic core **Fig. 5**, which has been proved to be a suitable material for complementary circuits and shown to yield high-performance devices by sublimation or from solution methods. [6] X-ray diffraction (XRD) and AFM analyses on films of different thickness deposited at different substrate temperatures indicate the existence of two temperature-dependent deposition regimes: a low-temperature (RT) regime and a high-temperature (80-120° C) one, each characterized by different growth mechanisms. These growth mechanisms results in different morphology, which in turn are correlated to the trends of the electrical parameters measured in OTFTs based on PDI8-CN2. [6] Structural differences where observed also for the first three MLs for low (RT) and high (120° C) substrate temperatures, and it has been demonstrated, [7] that their evolution during growth determines which ML contributes most to the charge transport in the OFET.

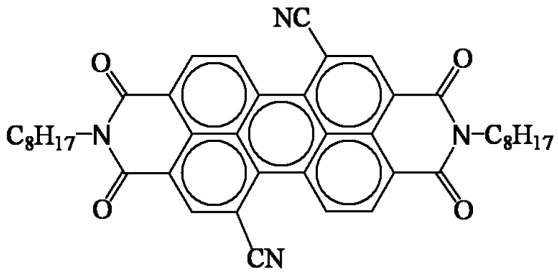

Fig. 5 Sketch of the molecule Perylene (PDI8-CN2). [8]

Materials: substrates

Silicon oxide is an amorphous inorganic material in which silicon binds four oxigens with a tetrahedral geometry. At the surface however two different kind of bonds are present: silanols (Si-OH) and siloxanes (Si-O-Si). The naturally forming oxide layer in contact with air is only about 20 angstrom thick, it is composed of a superficial layer with stoichiometry SiO_2 7 Å thick and underneath a layer 13 Å thick which as a non-stoichiometric composition usually indicated as SiO_x.

Growth of a monolayer of α-Sexithiophene (6T) on native SiO_x

6T Preparation

The KC crucible was cleaned from the 6T residues by means of acetone bath sonicated for several minutes. The KC components were manually cleaned by acetone. When the crucible was dry, it was loaded for two thirds with 6T (bright orange powder), using a spatula, and placed back in the KC. The 6T was purified by heating the KC in HV (up to 180°C) for several days.

6T Experimental

The goal of this experiment was to obtain an almost perfectly completed ML of α-Sexithiophene on native silicon oxide (SiO_x). This means a film formed by enough 6T molecules, oriented normally to the surface, to occupy the entire surface of the substrate, and no more molecules, that would start to grow on the second ML increasing the roughness. [9]
The parameters that control the evolution of the experiment are:

- Temperature of the substrate (T_{sub}) [° C];
- Temperature of the effusion cell (T_{cell}) [° C];
- Deposition rate (r) [ng/min];
- Amount of molecules deposited on the quartz microbalance usually referred to as 'thickness' [ng].

The first step of this experiment is to perform a calibration of the thickness, in order to obtain a coverage of approximately 33% ML at RT. For instance, we started from the sublimation of 15 ng of 6T with a T_{cell} = 267° C, in order to have a Φ = 5 ng/min at T_{sub} = RT.

The ex-situ AFM characterization was carried out obtaining at least three topographic images (usually 20 µm x 20 µm), to determine the averaged surface coverage <Θ>, defined as the mathematical average of coverages measured. Images were elaborated with the software Gwyddion and coverages were calculated with the threshold process, which consists in selecting the islands by their height (upright molecules are 2,4 nm long). The resulting <Θ> was 25% ML. In **Fig. 1** is reported an AFM image obtained for this sample. In this image the scale of colors turns lighter along with a bigger height, islands can be seen in yellow, while the bottom SiO_x is brown. This image dimensions are 10 µm x 10 µm, in order to better appreciate the island disposition.

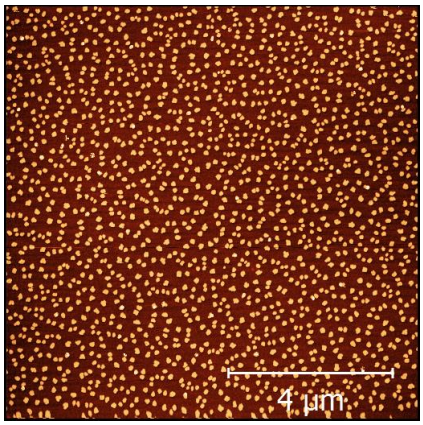

Fig. 1 AFM topographic image of 6T islands grown on native SiO_x. The scale of colors turns lighter along with height; islands (upright molecules are 2,4 nm) can be seen in yellow.

In order to obtain a <Θ> = 33% ML the rate between molecules sublimated and the coverage obtained was calculated and multiplied by the coverage desired. The proportion is reported below in **Eq. 1**.

Eq. 1 12 (Thickness adopted) : 25 (Coverage obtained) = *X* (New thickness) : 33 (Target coverage)

$$X = \frac{12\ ng \times 33}{25} \approx 16\ ng$$

In this way we found the thickness that we needed to use for the next experiment, in order to obtain a coverage of approximately 33% ML.

This step is repeated until the coverage is exactly the one desired. With the same conditions, small variations (± 2%) are intrinsic of the technique, while higher ones could indicate some changes of the material conformation, occurred in the crucible or other issues to be taken care of. Also when

the material is just been loaded in the crucible, several depositions could be needed to obtain a stable behavior of the sublimation process.

Once the <Θ> = 33% ML was obtained, the same conditions were employed in a new experiment where only T_{sub} was changed to 80° C. This experiment was needed to quantify the percentage of molecules that underwent re-evaporation at this T_{sub}. With the same thickness, this time a lower <Θ> = 10 % ML was obtained. Re-evaporation is calculated by difference between the coverage obtained at room temperature and that obtained at 80° C (**Eq. 2**).

Eq. 2 (Coverage obtained with T_{sub} = RT) – (Coverage obtained with T_{sub} = 80° C) = Percentage of molecules re-evaporated

$$33 - 10 = 23\ \%$$

$$X = \frac{16\ ng \times 33}{10} \approx 55\ ng$$

At this stage, with the same method used for the calibration at RT, another sublimation experiment was carried out, with the calculated thickness needed to obtain <Θ> = 33% ML at T_{sub} = 80° C.

The next step was to perform another experiment with the last experimental conditions used, only when the sublimation was stopped by decreasing T_{cell} and the Knudsen cell was closed, the heating of the substrate was not interrupted, but continued for 1 hour at the same temperature. This process, reported above as partial annealing, will explained in detail in a dedicated paragraph. In case the calculated <Θ> ≠ 33% ML after sublimation at 80° C, again the proportion **Eq. 1** could be used and another experiment would be performed. In our case this step did not change the final coverage, which remained <Θ> = 33% ML.

The final experiment, run to obtain a coverage of 100%, consisted in repeating three times the sublimation with the last experimental conditions described. The amount of molecules deposited on the SiOx substrate and the deposition rate *r* were kept constant to 55 ng and 5 ng/min, respectively. After each sublimation, the Knudsen cell was closed and T_{cell} decreased from 267° C to 180° C to prevent sublimation, while the substrate was kept for 1 hour at 80° C.

This series of experiments lead to a SiO_x substrate with an averaged surface coverage <Θ> = 97% ± 5 % ML.

A representative AFM image obtained for this sample is reported in **Fig. 2**.

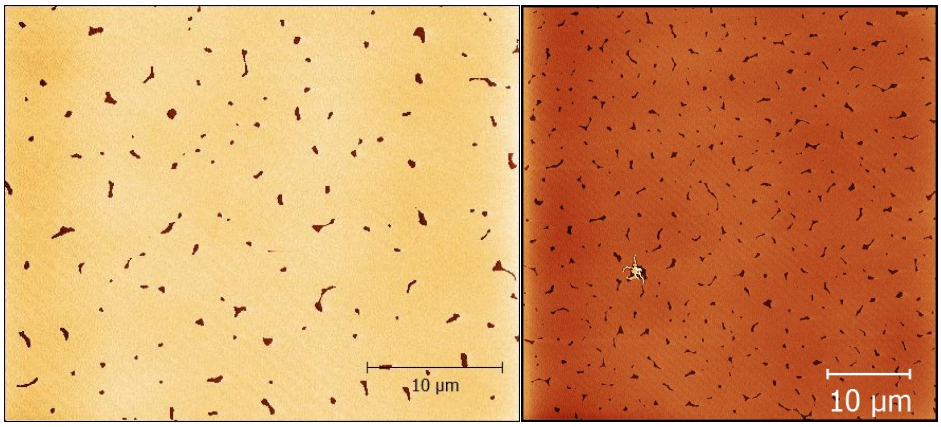

Fig. 2 AFM topographic images of a substrate of native SiO_x covered by 6T upright molecules with a calculated coverage of 97% ML. The darker spots represent the holes in the 6T film.

Below in **Fig. 3**, AFM images referring to different coverages obtained are reported.
If the AFM image in **Fig. 3 a** is confronted with that in **Fig. 3 d**, it is possible to notice as the small rounded islands formed by 6T molecules (**Fig. 3 a**) have coalesced into an almost continuous film of molecules and only some holes are present in this structure (**Fig. 3 d**). In **Fig. 3 b** is reported an AFM topographic image, where island of 6T have a bigger size than those in **Fig. 3 a**, the coverage here is 46 %, in order to show a typical intermediate situation in the growth of the firs monolayer of 6T on native SiO_x. The islands of 6T show a dendritic shape at this stage.

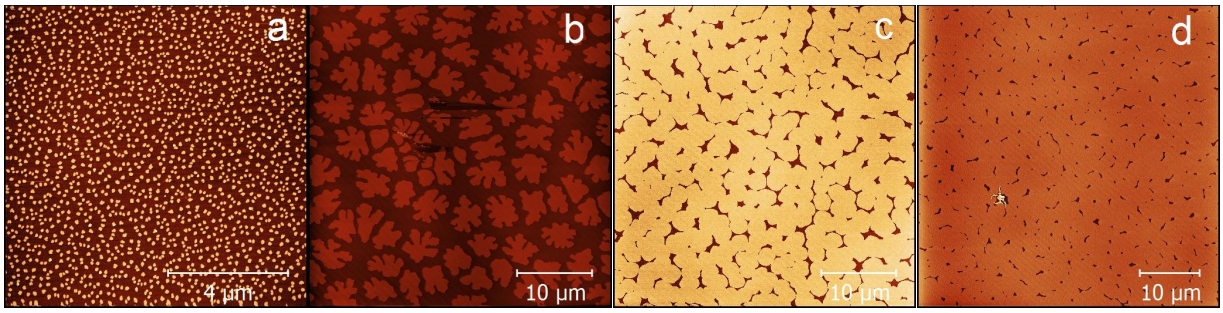

Fig. 3 AFM topographic images of a substrate of native SiO_x covered by 6T islands with calculated coverages of 25% (a), 46% ML (b), 92% (c) and 97% (d).

In **Fig. 3 c** is reported a substrate with a coverage of 92 %, similar to that shown in **Fig. 3 d**, but this time slightly inferior, in fact it is still possible to notice small spaces between former islands.

P5 Experimental

The experimental procedure followed to obtain a ML of Pentacene (P5) on native SiO_x was

analogous to that followed in the case of 6T.

For this experiment the amount of molecules deposited on the SiOx substrate and the deposition rate *r* were kept constant to 21 ng and 5 ng/min, respectively. After each sublimation, the Knudsen cell was closed and T_{cell} decreased from 164° C to 120° C to prevent sublimation, while the substrate was kept for 30 minutes at 40° C. The sublimation temperature of P5 is considerably lower than that of 6T due of its lower molecular weight. This makes easier for molecules to be re-evaporated but also reorganized requiring less energy. We observed that already a substrate temperature of 50° C was too high, in order to obtain a layer by layer growth, since molecules receive too much energy and start to grow in a three-dimensional fashion, forming vertical structures, namely crystals. For this reason T_{sub} and annealing time, were considerably reduced for this molecule.

The final experiment, run to obtain a coverage of 100%, consisted in repeating three times the sublimation with the experimental conditions described. Two representative topographic images of a sample obtained with this experiment are reported in **Fig. 4**. This sample showed an averaged surface coverage $\langle\Theta\rangle = 100\% \pm 2\ \%$ ML.

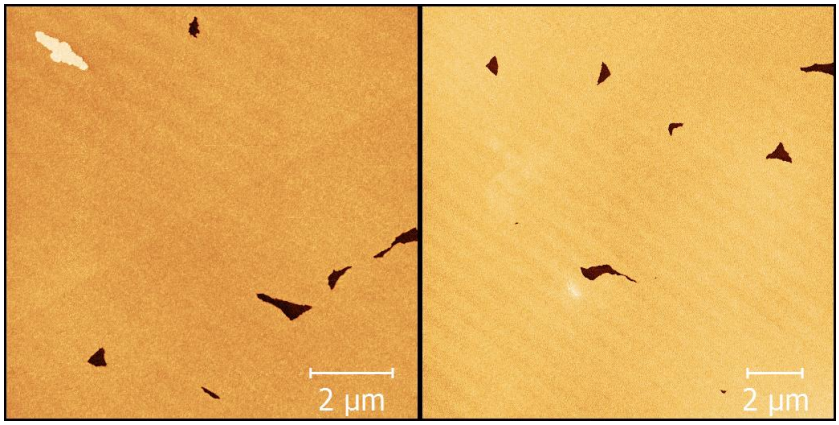

Fig. 4 AFM topographic images of a substrate of native SiO_x covered by P5 upright molecules with calculated coverages of 99%.

PDI8-CN2 Experimental

The experimental procedure followed to obtain a mono-molecular layer of N,N'-bis(n-octyl)-dicyanoperylene-3,4:9,10-bis dicarboximide (PDI8-CN2) on native SiO_x was analogous to that followed in the previous experiments. However, in this case the calibration at RT was not effective, since this molecule has two distinctive behaviors during growth at RT and growth at high T_{sub}.

Liscio et al. [7] demonstrated that PDI8-CN2 exhibited a marked difference in molecular organization, crystal order and density, which also reflects in the distribution of charge carriers in a transistor. The morphology observed at RT shows that grains a few nanometers diameter form, while at 120° C the morphology was characterized by elongated islands few micrometers long.

For this experiment the amount of molecules deposited on the SiOx substrate and the deposition rate *r* were kept constant to 27 ng and 5 ng/min, respectively. After each sublimation, the Knudsen cell was closed and T_{cell} decreased from 267° C to 180° C to prevent sublimation, while the substrate was kept for 1 hour at 80° C.

Two representative topographic images of a monolayer of PDI8-CN2 obtained with this experiment are reported in **Fig. 5**. This sample showed an averaged surface coverage $\langle\Theta\rangle$ = 96% ± 2 % ML.

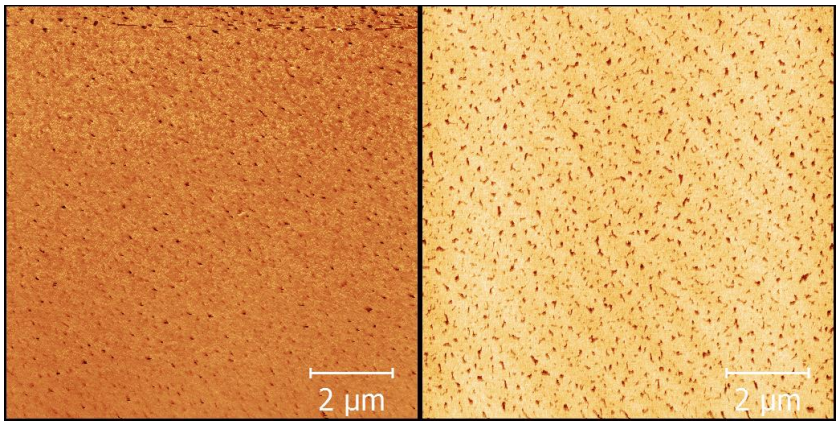

Fig. 5 AFM topographic images of a substrate of native SiO_x covered by PDI8-CN2 upright molecules with calculated coverages of 96%.

The table below summarizes all the experimental parameters relative to the experiments just reported.

	6T	P5	PDI8-CN2
MW [uma]	494,76	278,36	664,79
Thickness [ng]	3 x 55	3 x 21	3 x 27
Rate [ng/min]	5	5	5
Cell T [°]	267	164	267
Substrate T [°]	80	40	80
Annealing [min]	3 x 60	3 x 30	3 x 60

A brief description of the partial annealing process

When conjugated oligomers, like 6T, are deposited on a chemically inert and flat surface, like that of silicon oxide, initially stable nucleus composed of few molecules are formed. Subsequently, these nuclei evolve into islands during the deposition and coalesce to form a continuous organic layer. [10] Film growth is characterized by two simultaneous molecular dispositions, molecules can show an upright configuration, they dispose almost normal to the surface and form islands and the flat-lying configuration, of those molecules placed in between them. [1]

During the film's growth, these flat-lying molecules can affect islands coalescence in two ways: if they remain flat, an empty space in between islands is created; otherwise, if they are collected from islands, the interfacial disorder between islands is increased (domain boundaries). [11]

To utilize these films in electronic and optoelectronic devices, the molecular orientation with respect to the substrate is crucial: for Organic Light Emitting Diodes (OLEDs) or solar cell applications, growth of the molecules should preferably occur in a lying fashion. This allows the charge transport, which is perpendicular to the molecule's long axis, between the electrodes as is illustrated in **Fig. 6**. For OTFTs, instead, growth of standing molecules is desired on the gate oxide between source and drain.

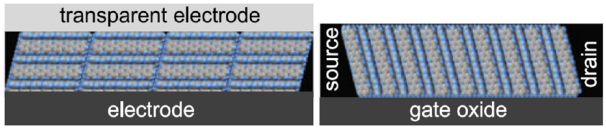

Fig. 6 Desired molecular orientation for OLEDs or organic solar cells (left). Arrangement for an OTFT application (right).

Flat lying molecules, not directly visible by AFM, where observed indirectly by Albonetti in 2011, through the application of a post annealing process. This process consists in keeping the substrate at the same temperature (80°C or 100°C) for 1 hour after the molecules deposition, while the sample and the Knudsen cell shutters are closed. In order to investigate the flat lying molecular layer, surface averaged coverage (<Θ>) were calculated for both substrate temperatures (80° C and 100° C) and with or without the application of the annealing process. These experiments showed that both at 80° C and 100° C the <Θ> increased when the post annealing process was applied. These results indicate that some molecules (not visible in AFM topographic image) are present in between islands and they are re-organized through the post-annealing process. In particular, the heat (energy) provided for 1 hour after the deposition gives energy and time to the not-organized molecules to

move towards islands thus increasing their size. [1]

Surface Characterization by SECM

The substrates covered with mono-molecular layers of 6T, P5 and PDI8-CN2, were characterized by means of Probe Approach Curves by SECM. By recording this kind of curves to a substrate, the rates of electron transfer reaction can be studied [12]. The ability of the substrate to regenerate the redox mediator species is described by the heterogeneous electron transfer constant (k_{eff}). Thus, these measurements allowed to determining surface conductivity of the different substrates. Furthermore to verify how the stability of the monolayers was affected by immersion in the electrolyte solution 1mM of FcCOOH in PBS, approaches were performed at time 0 (*t0*), after 30, 60 and 90 days, during this time samples were stored at 4° C when not in use, these curves were fitted and by the curve obtained k_{eff} was calculated (for details on the fitting and constant estimations see **Chapter 5**) . As shown **Fig. 7**, the approach curves performed on 6T at *t0*, 30 and 60 days did not change significantly, they all show a negative feedback, so $k_{eff} \approx 0$. Notably the monolayer decrease the conductivity of the bare SiOx substrate.

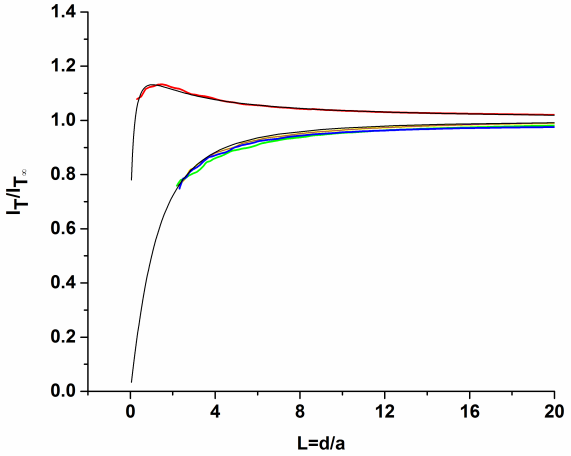

Fig. 7 PACs in 1mM FcCOOH on native SiO_x (red) and on 6T (blue green and orange) at *t0*, 30 and 60 days.

As a basis of comparison, in all the graphs in **Fig. 7-8-9**, the approach curve on native SiO_x (red) and the relative fitting curve (black) are reported. In **Fig. 7**, it is possible to notice, that SiO_x has a semipositive approach (k_{eff} = 0,68), which means that the uncovered substrate is a better conductor than the monolayer functionalized substrate in these conditions (FcCOOH used as redox mediator).

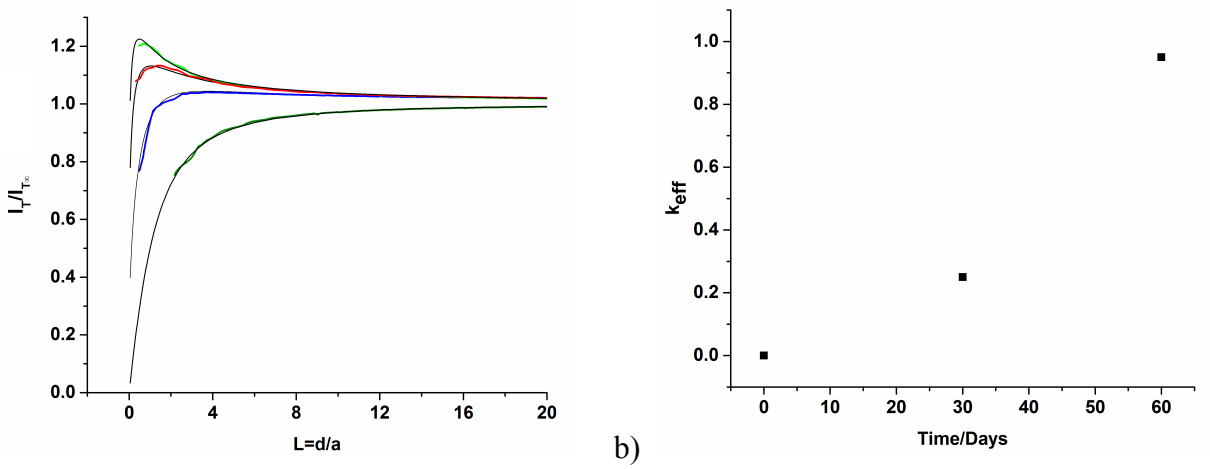

Fig. 8 a) PACs in 1mM FcCOOH on native SiO_x (red curve) and on P5 at *t0* (dark green), 30 (blue) and 60 days (light green). All approaches show the relative fitting curve (black). b) Calculated k_{eff} for approaches in FcCOOH 1 mM on Pentacene at *t0*, 30 and 60 days.

The behavior of Pentacene in this respect is quite different, in **Fig. 8 a** it is possible to observe how the conductivity, measured using the same conditions as in the case of 6T, changes dramatically in time. The first measurement at *t0* (dark green line) shows a negative approach, after 30 days the film of molecules probably started to undergo some kind of variation and consequently the approach curve became less negative. The last PAC performed (light green line) shows a conductivity even improved, if compared to that of SiO_x. **Fig. 8 b** shows how the electron transfer constants change in time, the calculated k_{eff} at various times are reported in the following table. This behavior shows that the monolayer is not stable when it is immersed for several days in the PBS.

P5

t (days)	k_{eff}
0	0
30	0,25
60	0,95

The PACs performed on PDI8-CN2, displayed in **Fig. 9 a**, highlight a characteristic behavior. At

time zero, the approach is negative, in line with the other substrates.

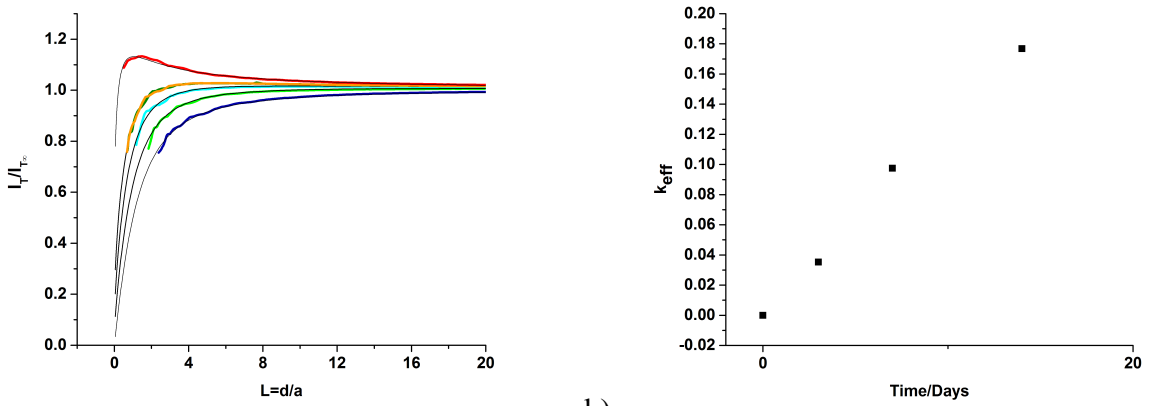

a) b)

Fig. 9 a) PACs in 1mM FcCOOH on native SiO_x (red curve) and on PDI8-CN2 at *t0* (violet), 3 (light green) and 7 (light blue), 14 (dark green) and 90 days (orange). All approaches show the relative fitting curve (black). b) Calculated k_{eff} for approaches in FcCOOH 1 mM on PDI8-CN2 at *t0*, 3, 7, 14 and 90 days.

Then it shows a constant increase in the k_{eff} values, that is evident in **Fig. 9 b**, for measurements after 3, 7 and 14 days. After two weeks the conductivity of the substrate apparently reaches a plateau, as testified from the approach performed after 90 days. The curves registered after 14 and 90 days in fact (dark green and orange respectively), are almost superimposable and the calculated k_{eff} are approximatively the same, as reported in the table below.

PDI8-CN2

t (days)	k_{eff}
0	0
3	0,04
7	0,10
14	0,18
90	0,18

References

1. Albonetti C., Biscarini F. . *Microscopie*, 36 (2011)
2. Horowitz G., Fichou D., Peng X., Xu Z., Garnier F., Moleculaires M. and Dunant H.. *Solid State Communications*, 72, 381 (1989)
3. Koch N. et al. Organic Electronic Devices and Their Functional Interfaces. *ChemPhysChem*. 8 (10): 1438–55. (2007) doi:10.1002/cphc.200700177
4. Yamashita Y. et al. Organic semiconductors for organic field-effect transistors. *Sci. Technol. Adv. Mater*. 10 (2). (2009) doi:10.1088/1468-6996/10/2/024313
5. Cramer, T., Chelli, B., Murgia, M., Barbalinardo, M., Bystrenova, E., de Leeuw, D. M., & Biscarini, F. (2013). Organic ultra-thin film transistors with a liquid gate for extracellular stimulation and recording of electric activity of stem cell-derived neuronal networks. *Physical Chemistry Chemical Physics : PCCP*, *15*(11), 3897–905. https://doi.org/10.1039/c3cp44251a
6. Liscio, F., Milita, S., Albonetti, C., Angelo, P. D., Guagliardi, A., Masciocchi, N., and Biscarini, F. . Structure and Morphology of PDI8-CN2 for n-Type Thin-Film Transistors, 943–953. *Adv. Funct. Mater.* (2012) https://doi.org/10.1002/adfm.201101640
7. Liscio, F., Albonetti, C., Broch, K., Shehu, A., Quiroga, S. D., Ferlauto, L., and Milita, S.. Molecular Reorganization in Organic Field-Effect Transistors and Its Effect on Two-Dimensional Charge Transport Pathways, *Acs Nano* (2), 1257–1264.
8. Ferlauto L., Liscio F., Orgiu, E., Masciocchi N., Guagliardi A., Biscarini B., Samorì P. and Milita S. Enhancing the Charge Transport in Solution-Processed Perylene Di-imide Transistors via Thermal Annealing of Metastable Disordered Films, (696656). *Adv. Funct. Mater.* (2014) https://doi.org/10.1002/adfm.201400789
9. R. Kariotis and M. G. Lagally. *Surf. Sci.*, 216, 557 (1989)
10. Ruiz R., Choudhary D., Nickel B., Toccoli T., Chang K.-C., Mayer A. C., Clancy P., Blakely J. M., Headrick R. L., Iannotta S. and Malliaras G. G.. *Chemistry of Materials*, 16, 4497 (2004)
11. Annibale P., Albonetti C., Stoliar C. and Biscarini P.. J. Phys. Chem. *J. Phys. Chem.* A, 111, 12854 (2007)
12. Bard AJ, Introduction and principles (Chapter 1). *Scanning Electrochemical Microscopy*. (a) Borgwarth K, Heinze J, Heterogeneous electron transfer reactions (Chapter 6) – Unwin PR, Kinetics of homogeneous reactions coupled to heterogeneous electron tranfer (Chapter 7)

3. Characterization of Cell-Organic Monolayer Interaction by Fluorescence Microscopy

In order to evaluate the biocompatibility, the proliferation, the average cellular area, the distribution on the samples examined and the differences between the substrates with monomolecular layers and the bare silicon oxide (SiOx), optical and fluorescence microscope measurements were performed. The images acquired were then elaborated with the software Image J. Initially it was necessary to standardize a consistent procedure for the image analysis of all the samples, so that the data collected were reliable. In the case of cells grown on bare silicon oxide, a different method for cell counting had to be used.

Experimental Part

In the following experiment MCF10A cells were grown for 24 hours at 37°C, 5% CO_2 (for details on the cell line and culturing media see the material and method part at the end of this chapter), on a 6 wells multiwell plate, 4 wells were occupied by the substrates (area ≈ 1 cm^2) previously described. In details: the first well contained a sample of bare silicon oxide, the second the third an fourth contained samples of SiOx (CONTROL) covered with a monomolecular layer of three different molecules: respectively pentacene (P5), N,N0-bis(n-octyl)-dicyanoperylene-3,4:9,10-bis(dicarboximide) (PDI8-CN2) and α-sexithiophene (T6). The fifth and the sixth contained no samples, as control. Cells were cultured on all six wells, with a density that allowed a uniform distribution with cells not too close (40000 cells for well). For each samples 18 fluorescence images were acquired and then analyzed with the software Image J.

Procedure Standardization

A. Optical Images of MCF10A on Native SiOx (control samples)

In order to evaluate the cell distribution on the native SiOx substrates, optical images (800x800 μm) were captured using a 10x magnification. Unfortunately, as it is clear by **Fig. 1**, these were not sufficient for a thorough evaluation, owing to the sample opacity, which prevented the use of the optical microscope in transmission mode.

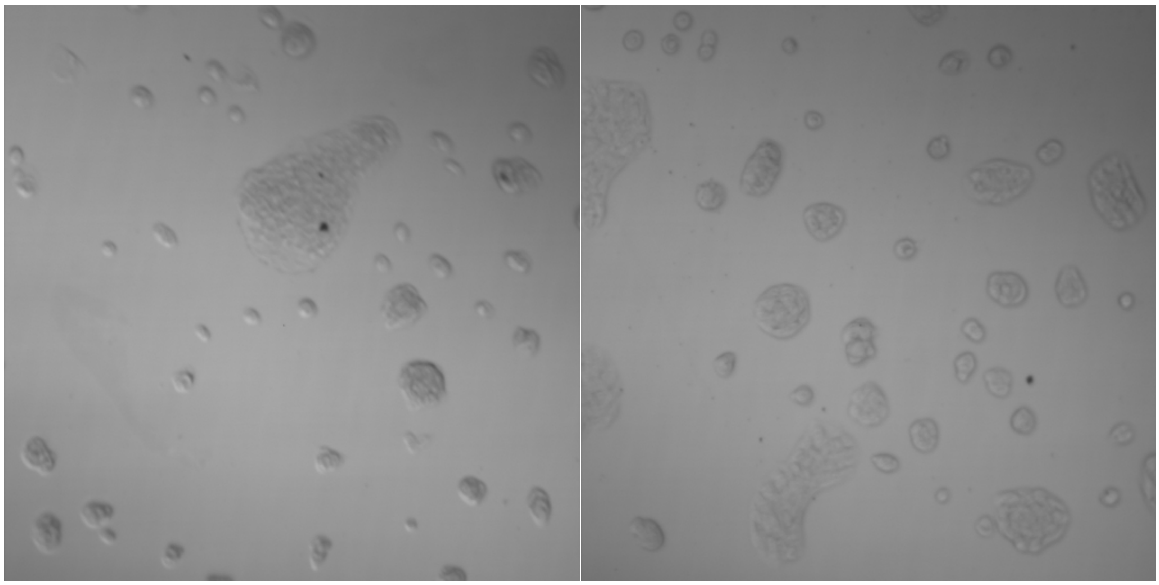

Fig. 1 Optical images 800x800 µm at 10x magnification. Native SiOx (Control_1), left; Native SiOx (Control_2), right.

Therefore it was decided that fluorescence microscopy would be the best choice to analyze the cell distribution and the cell number on our substrates. The samples were stained with 4,6-diamidino-2-phenylindole (DAPI), a nuclear stain and 10x fluorescence images were obtained. The images were taken using epifluorescence microscopy as described in the methods at the end of the chapter.

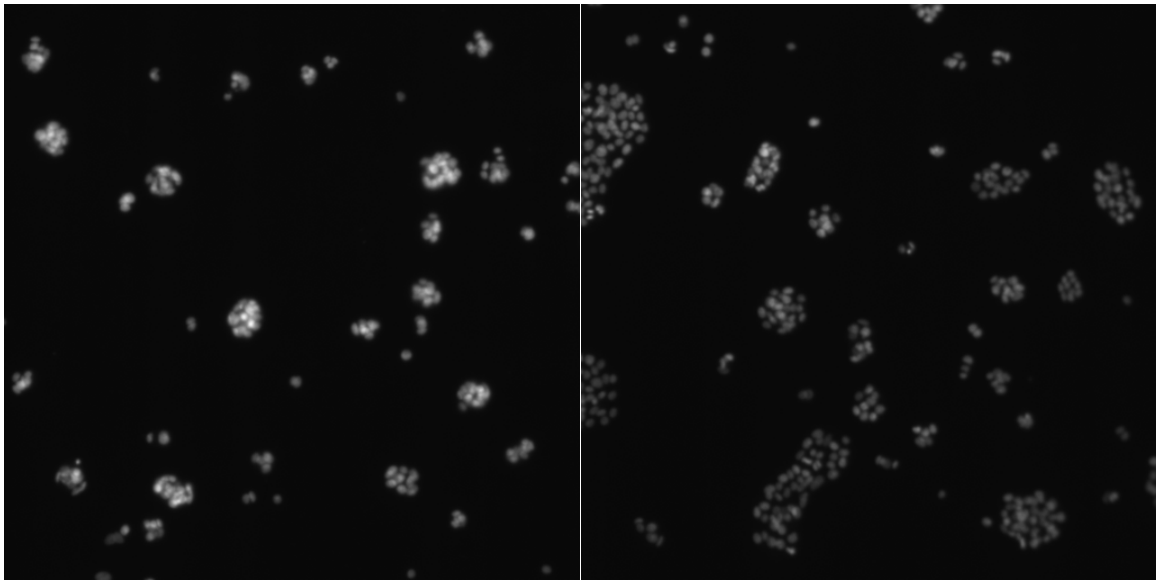

Fig. 2 Fluorescence images 800x800 µm at 10x magnification. Native SiOx (Control_1), left; Native SiOx (Control_2), right.

The cellular count was then performed using Image J. All the steps followed in this procedure are resumed below.

File > *Open* > choose the image to analyze

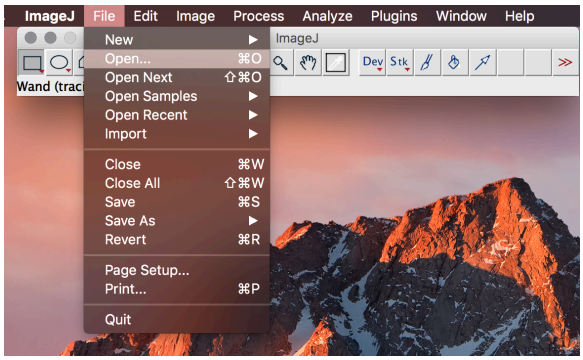

Image > *Adjust* > *Threshold* > adjust the threshold manually so that the white area matches that in the fluorescence image

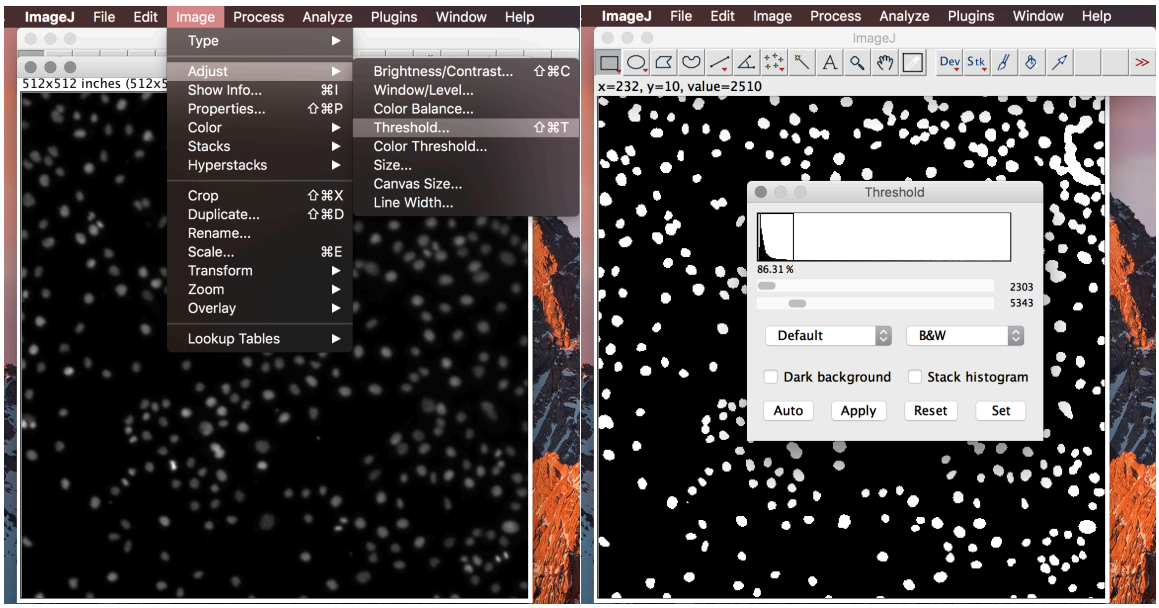

Process > *Binary* > *Watershed* > this command allows to separate those areas whose images were merged together for an error of the software

Process > *Binary* > *Make Binary* > the binary image that will be analyzed is produced

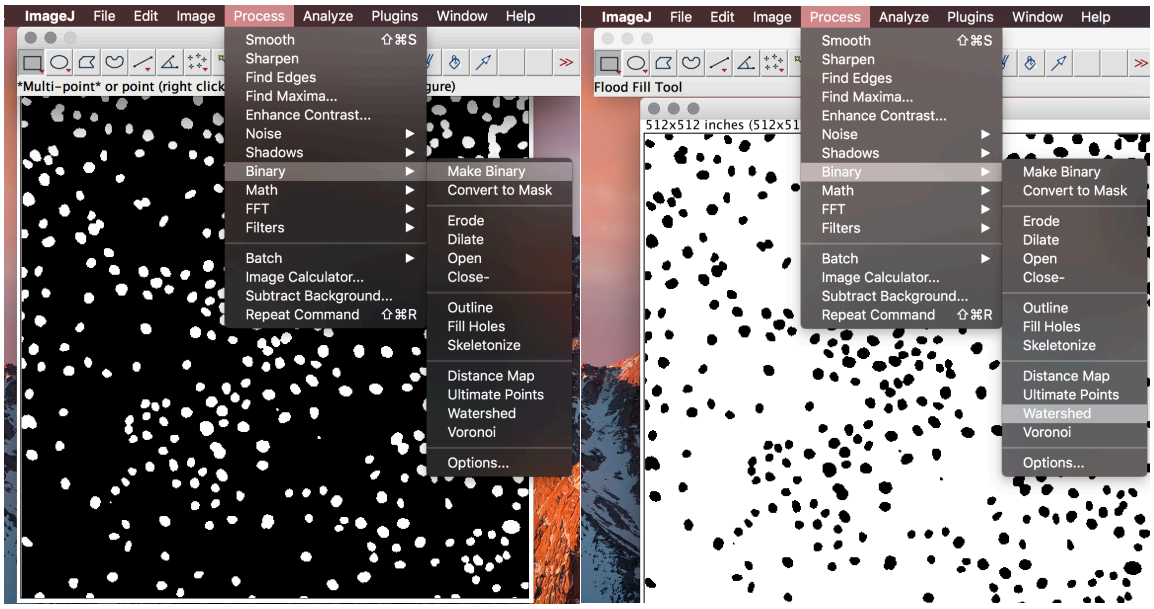

Analyze > *Analyze Particles* > it is possible to select a minimum size that will be detected in order to cut off particles not related with the cell counting

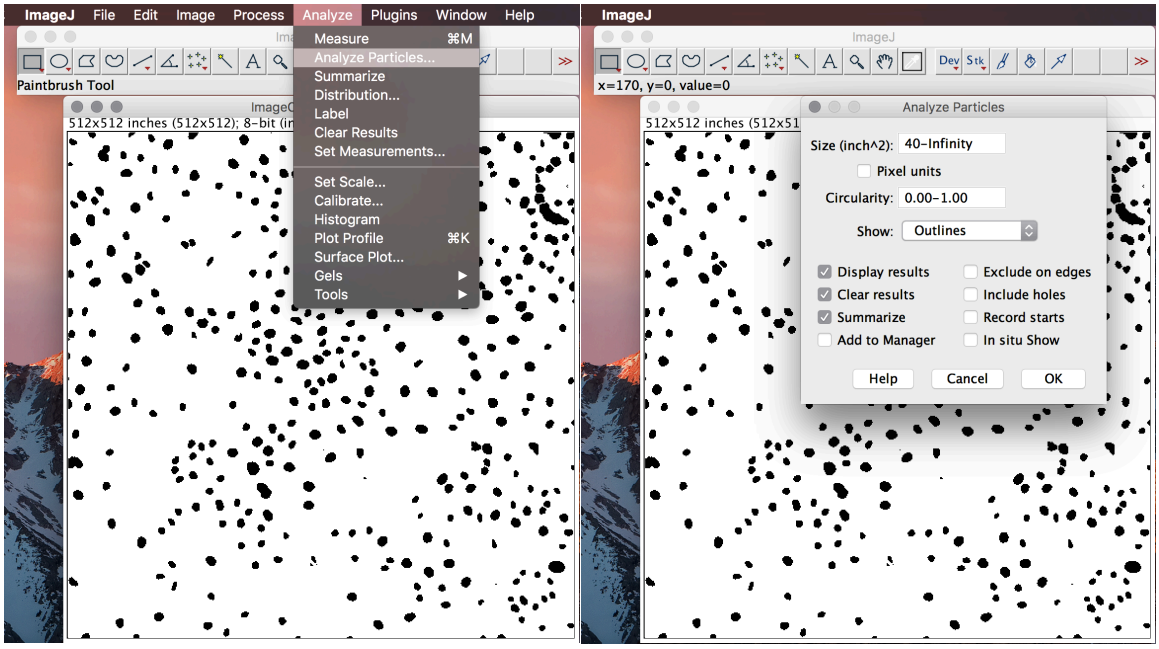

The software output will show the Total Area, the cell Count as well as the Area corresponding to every single cell analyzed and their Average Size.

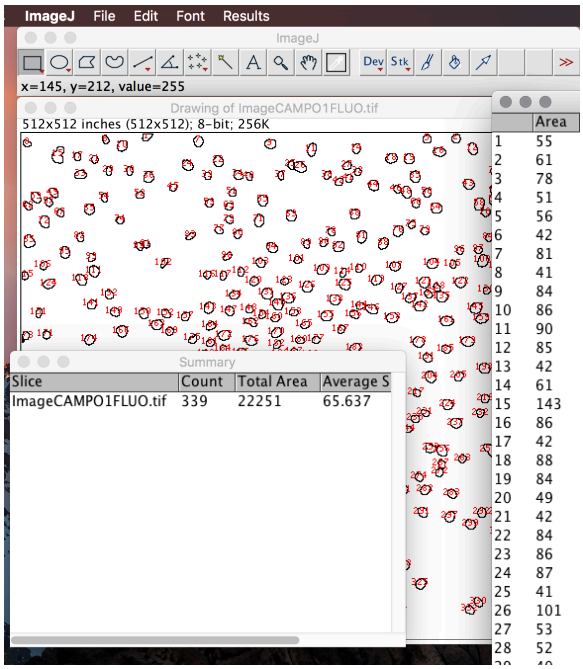

The procedure just described, while effective for the other samples of this study, was not advisable for MCF10A cells grown on SiOx. In fact applied to the sample "Control_1", led to the results in Fig. **2**. It is clear that this method is not effective, as multiple cells are counted as one due to their proximity.

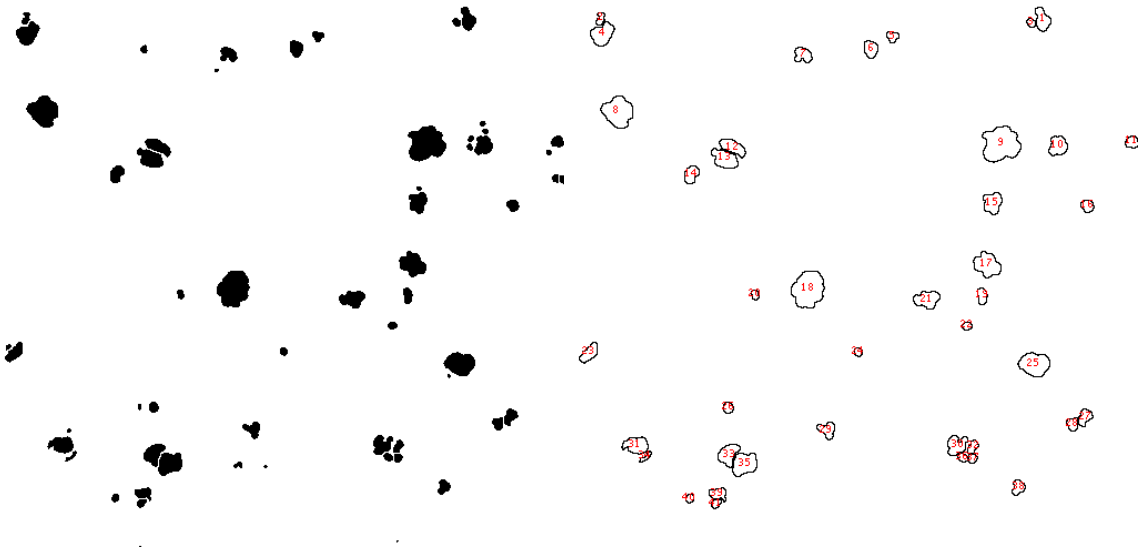

Fig. 2 Binary image produced after Image J analysis of "Control_1" (left) and relative output of the cell count (right).

It was observed that cells had a three-dimensional growth on SiOx substrates, thus forming aggregates (foci). The procedure described before requires a minimum distance among cells that is not present in this case. Therefore it was necessary to adopt a different approach, in order to obtain a better esteem of the cell number on these samples. The method is the following.

File > *Open* > choose the image to analyze

Process > *Find Maxima* > select the noise tolerance

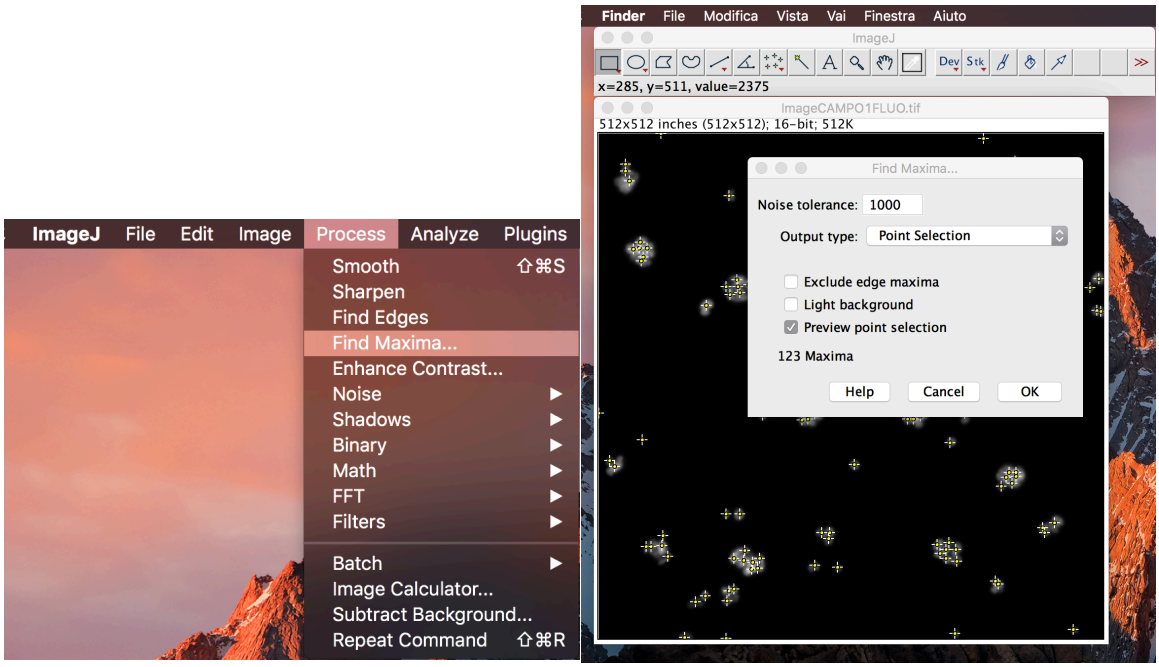

With this procedure we were able to obtain a plausible esteem of the number of cells on the sample. For obvious reasons the cell count will be underestimated, as cells are stacked on one another and this technique only allows to image the superficial cells. This procedure does not allow to calculating cellular area.

Below are reported some representative fluorescence images acquired with the relative elaborations: maxima count for the SiOx; cell number and cell average area for the other substrates.

MCF10A on Native SiOx

The feature of MCF10A cells three-dimensional growth on SiOx is repeated here as shown in **Fig. 4**, where Image 7 and Image 9 clearly highlight the presence of multiple foci on the surface.

Fig. 4 Fluorescence images of "CONTROL" (MCF10A on SiOx) Image 7 (left), Image 9 (right).

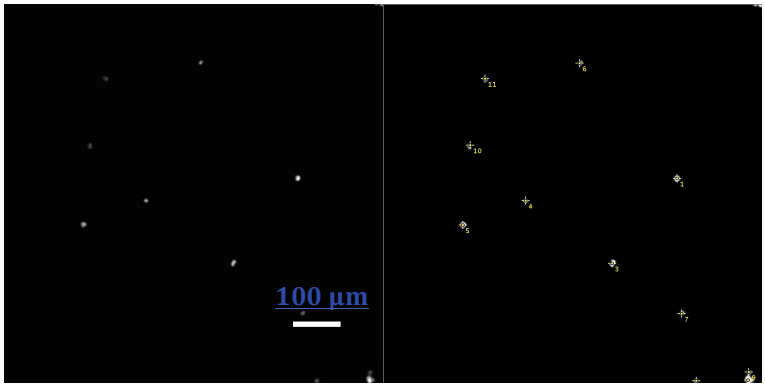

Image 1 Maxima: 11

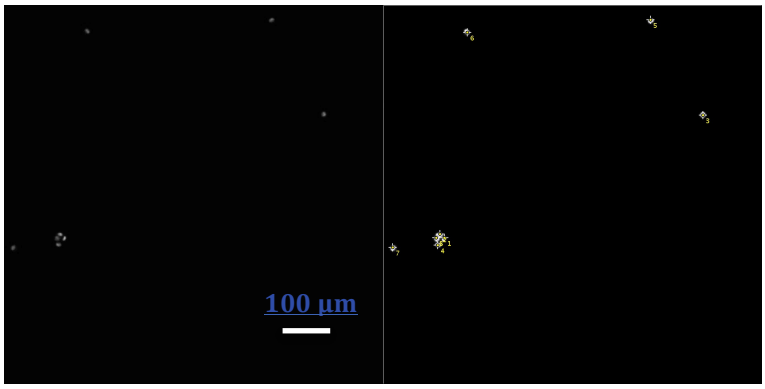

Image 2 Maxima: 8

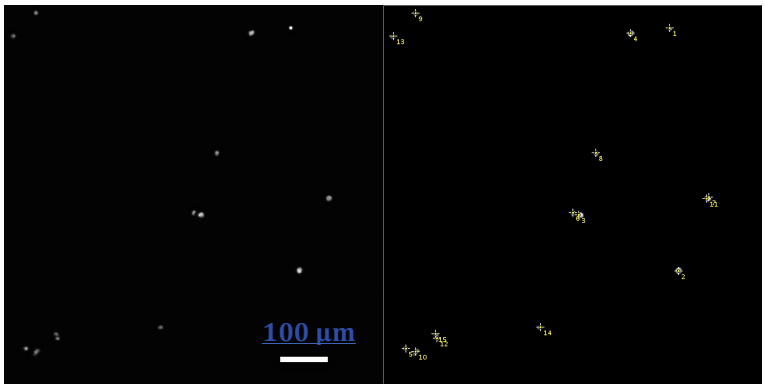

Image 3 Maxima: 15

MCF10A on Pentacene

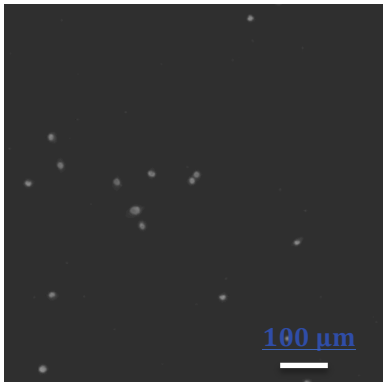

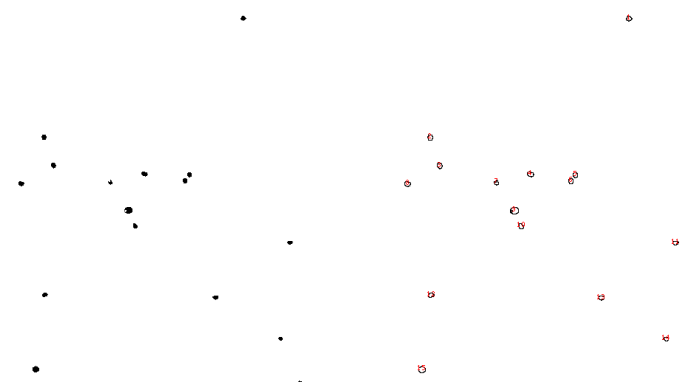

Image 1 Count: 15 Average Area: 95 µm^2

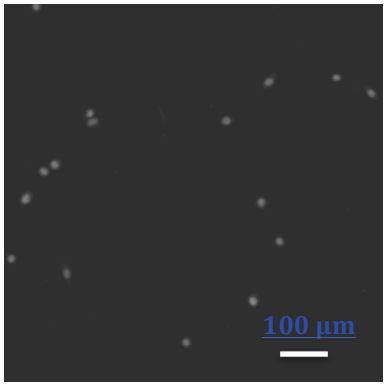

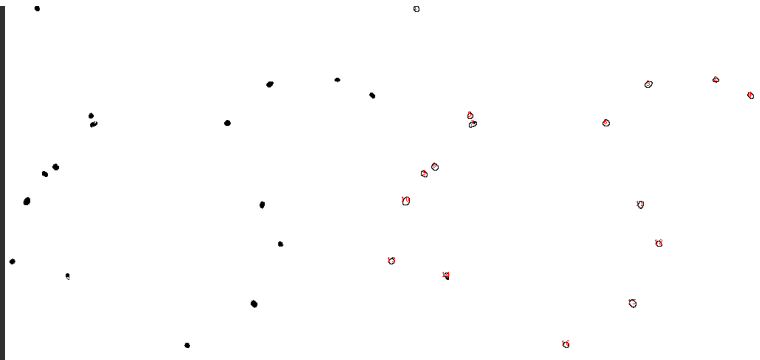

Image 2 Count: 16 Average Area: 120 µm^2

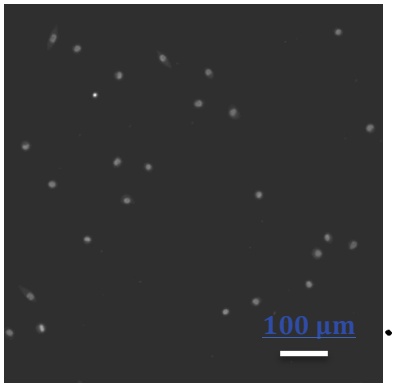

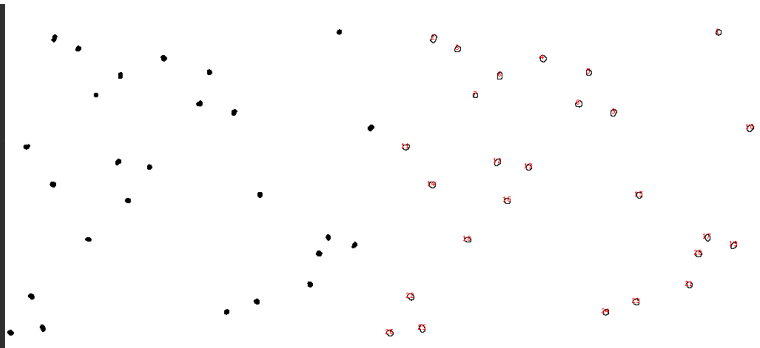

Image 3 Count: 26 Average Area: 122 µm^2

MCF10A on PDI8-CN2

Image 1 Count: 20 Average Area: 90 µm²

Image 2 Count: 23 Average Area: 88 µm²

Image 3 Count: 11 Average Area: 71 µm²

MCF10A on α-Sexithiophene

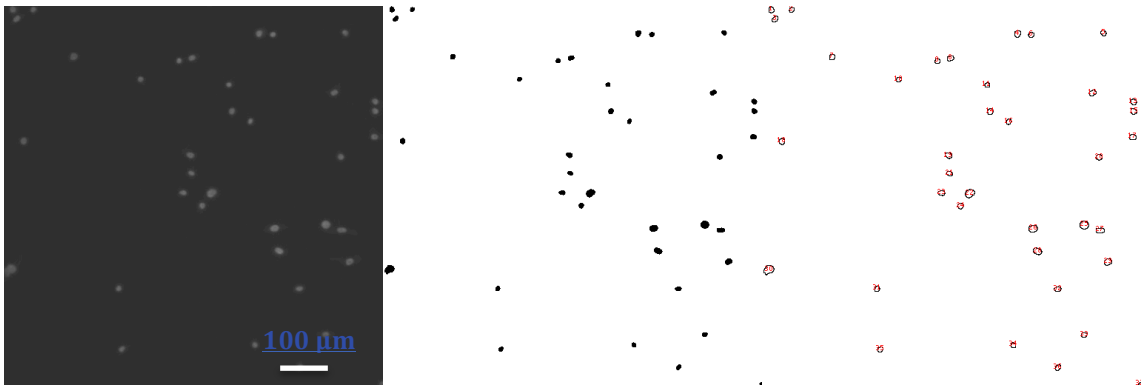

Image 1 Count: 37 Average Area: 127 µm²

Image 2 Count: 22 Average Area: 115 µm²

Image 3 Count: 25 Average Area: 83 µm²

After statistical data treatment (paired t-test with the null hypothesis to determine whether the mean difference between two sets of observations is zero) the average cell number for each sample were obtained and are reported in **Table 1**.

	Average Cell Number/ 0.64 mm^2
MCF10A on SiOx	20 ± 3
MCF10A on P5	31 ± 2
MCF10A on PDI	18 ± 1
MCF10A on T6	23 ± 2

Table 1: Average cell number calculated for each sample.

The results are schematized in a column graph in **Fig. 3**.

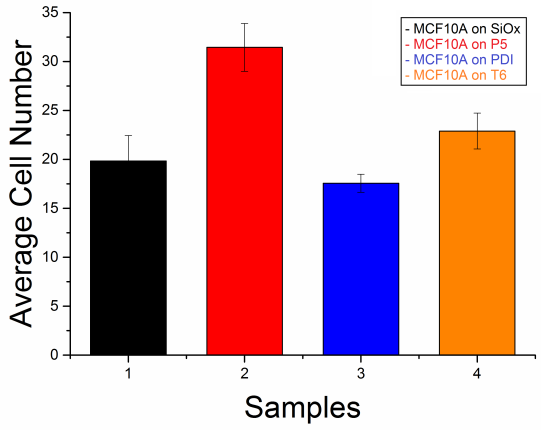

Fig. 3 Average cell number for each sample (0.64 mm^2 area). MCF10A on SiOx (black); MCF10A on Pentacene (red); MCF10A PDI8-CN2 (blue); MCF10A on α-sexithiophene (orange).

After statistical data treatment (paired t-test, vide infra) the average cell area for P5, PDI and T6 were calculated and are reported in **Table 2** (**Fig. 4**). As already mentioned, it was not possible to calculate the area of the cells on SiO_x with a sufficient degree of confidence as the cells grown in foci and it is not possible to distinguish single cell area.

	Average Cell Area/μm^2
MCF10A on P5	99 ± 4
MCF10A on PDI	77 ± 3
MCF10A on T6	94 ± 4

Table 2: Average cell area calculated for P5, PDI and T6.

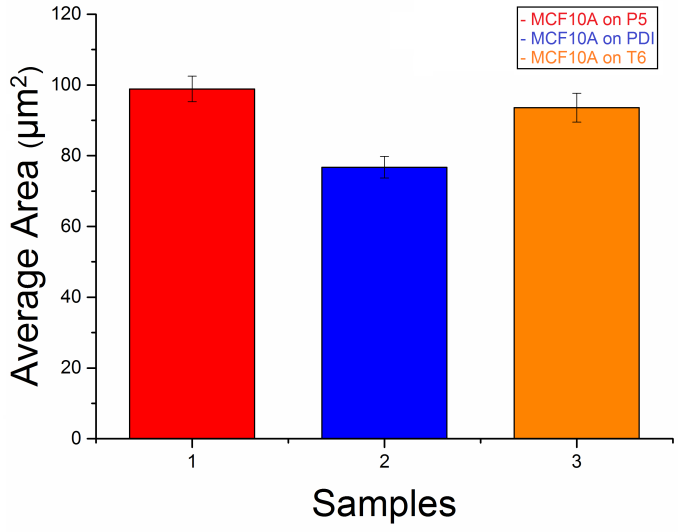

Fig. 4 Average cell area (µm^2) calculated for each sample. MCF10A on Pentacene (red); MCF10A PDI8-CN2 (blue); MCF10A on α-sexithiophene (orange).

By this study, carried out by means of fluorescence microscopy, it was possible to investigate cell density as well as cell distribution of MCF10A cells cultured on native SiOx and monomolecular layers grown on native SiOx of pentacene, N,N0-bis(n-octyl)-dicyanoperylene-3,4:9,10-bis(dicarboximide) (PDI8-CN2) and α-sexithiophene. The following features were noticed: the presence of monomolecular layers highly influences the cellular growth. In particular, in absence of such molecular coverage on native SiOx cells tend to grow in a three-dimensional way, by forming aggregates. This behavior reflects the presence of a stronger cell-cell interaction over the cell-material interaction, due to a low affinity with the substrate used as control. In all the samples with the organic monolayers instead, the cell grow in adhesion and singularly as expected by the morphology of the cells employed. Therefore cell-material interaction overwhelms the cell-cell interaction and thus is enhanced with respect to the silicon oxide. This implies that all these samples are biocompatible. After statistical t-tests carried out with Origin 9.0 software it is possible to make some remarkable consideration. Taking into account the cellular count on the different samples, the only monomolecular layer resulting significantly different from SiOx is P5, whether PDI and T6 are not. This result must be further interpreted since, as already said many times, qualitatively the growth on SiOx is not favored and certainly this substrate cannot be considered biocompatible. Paired t-test carried out between P5 and T6, P5 and PDI, PDI and T6, show in all cases significance differences.

Interestingly considering the order of values in the average cellular area found reflects that of the cell count of the same substrate but in this case the calculated average areas of P5 and T6 are not significantly different between them, but are both significantly different than that of PDI.

In conclusion, among the samples studied it appears that a monomolecular layer of P5 on SiOx is to be considered the environment for which MCF10A cells have the best affinity, considering the higher proliferation and the larger adhesion they show. By contrast PDI on SiOx resulted to be the substrate with which cells interacts the least, as proved by both the cellular count and the measured area. Lastly, T6 on SiOx has an intermediate behavior between the other two, in fact it is significantly different from PDI both as number of cells and of average area, so it displays a better affinity and is not significantly different from P5 in terms of average areas, which could suggest that this material promotes adhesion more than proliferation.

Materials and Methods

MCF10A cells

The MCF10A cell line is a non-tumorigenic epithelial cell line, these cells are human (*Homo sapiens*) and adherent. [1] Their biosafety level is 1 and they come from a fibrocystic disease affected patient. The cell line is positive for epithelial sialomucins, cytokeratins and milk fat globule antigen. MCF10A cells exhibit three-dimensional growth in collagen and form domes in confluent cultures. (**Fig. 5**) This cell line is responsive to insulin, glucocorticoids, cholera enterotoxin, and epidermal growth factor (EGF). By electron microscopy the cells display characteristics of luminal ductal cells but not of myoepithelial cells, they also express breast specific antigens as detected by positive reaction with MFA-Breast and MC-5 monoclonal antibodies. The calcium content of the medium exerts a strong effect on the morphology of the cells. [1]

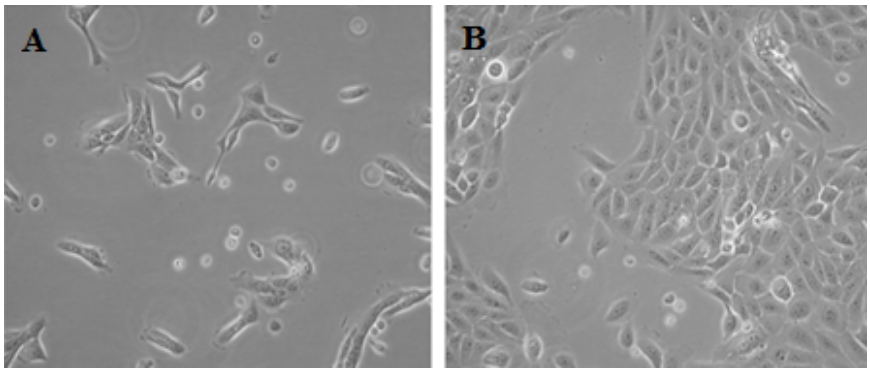

Fig. 5 Optical images of MCF10A cell line. A) Low density MCF10A cells. B) High density MCF10A cells. [1]

MCF10A Cell Growth Medium

Inorganic Salts (g/liter)	
$CaCl_2$ (anhydrous)	0.20000
$Fe(NO_3)_3 \cdot 9H_2O$	0.00010
$MgSO_4$ (anhydrous)	0.09770
KCl	0.40000
$NaHCO_3$	1.50000
NaCl	6.40000
$NaH_2PO_4 \cdot H_2O$	0.12500
Amino Acids (g/liter)	
L-Arginine·HCl	0.08400
L-Cystine·2HCl	0.06260
L-Glutamine	0.58400
Glycine	0.03000
L-Histidine·HCl·H_2O	0.04200
L-Isoleucine	0.10500
L-Leucine	0.10500
L-Lysine·HCl	0.14600
L-Methionine	0.03000
L-Phenylalanine	0.06600
L-Serine	0.04200
L-Threonine	0.09500
L-Tryptophan	0.01600
L-Tyrosine·2Na·2H_2O	0.10379
L-Valine	0.09400

Vitamins (g/liter)	
Choline Chloride	0.00400
Folic Acid	0.00400
myo-Inositol	0.00720
Nicotinamide	0.00400
D-Pantothenic Acid (hemicalcium)	0.00400
Pyridoxine·HCl	0.00400
Riboflavin	0.00040
Thiamine·HCl	0.00400
Other (g/liter)	
D-Glucose	4.50000
Phenol Red, Sodium Salt	0.01500
Sodium Pyruvate	0.11000

Table 3: Formulation for Dulbecco's Modified Eagle's Medium (DMEM). [1]

The medium used for the growth of MCF10A has the following composition: 5% Horse Serum, 0.5% L-Glutamine (also present in Ham's F12 Glutamax at 0.5%; stock concentration: 200 mM, medium concentration: 1 mM), 1% P/S (stock concentration: 5000 U/mL; medium concentration: 50 U/mL), 1% Insuline (Ins, stock concentration: 100x ; medium concentration: 1x), 0.5% Hydrocortisole (Hydro); 0.1% Cholerotoxin (CT); 0.02% Epidermal Growth Factor (EGF); DMEM (**Table 3** contains a list of DMEM components), Ham's F12-Glutamax: 2 mM L-Glutamine and 1500 mg/L sodium bicarbonate (**Table 4** contains a list of F12-Glutamax components) [1]; DMEM/Ham's F12, 1:1 mixture.

Inorganic Salts (g/liter)	
$CaCl_2 \cdot 2H_2O$	0.13524
$CuSO_4 \cdot 5H_2O$	0.0000025
$FeSO_4 \cdot 7H_2O$	0.000834
$MgCl_2 \cdot 6H_2O$	0.10572
$MgSO_4$ (anhydrous)	0.19264
KCl	0.28329
KH_2PO_4 (anhydrous)	0.05852
$NaHCO_3$	1.50000
Na_2HPO_4 (anhydrous)	0.11502
NaCl	7.59720
$ZnSO_4 \cdot 7H_2O$	0.000144
Amino Acids (g/liter)	
L-Arginine (free base)	0.42140
L-Alanine	0.01782
L-Asparagine·H_2O	0.03020
L-Aspartic Acid	0.02662
L-Cysteine·HCl·H_2O	0.07024
L-Glutamic Acid	0.02942
L-Glutamine	0.29220
Glycine	0.01501
L-Histidine·HCl·H_2O	0.04192
L-Isoleucine	0.00782
L-Leucine	0.02624
L-Lysine·HCl	0.07304
L-Methionine	0.00895
L-Phenylalanine	0.00991
L-Proline	0.06906
L-Serine	0.02102
L-Threonine	0.02382
L-Tryptophan	0.00408
L-Tyrosine (free base)	0.01087
L-Valine	0.02342

Vitamins (g/liter)	
D-Biotin	0.0000733
Choline Chloride	0.01396
Folic Acid	0.00132
Hypoxanthine	0.00408
myo-Inositol	0.01802
Nicotinamide	0.0000366
D-Pantothenic Acid (hemicalcium)	0.000477
Putrescine·2HCl	0.000322
Pyridoxine·HCl	0.0000617
Riboflavin	0.0000376
Thiamine·HCl	0.000337
Thymidine	0.000727
Vitamin B-12	0.001355
Other (g/liter)	
D-Glucose	1.26000
Phenol Red, Sodium Salt	0.00332
Sodium Pyruvate	0.22000
Lipoic Acid	0.00021

Table 4: Formulation for F-12K Medium. [1]

MCF10A cell culture

The cells were cultured in the aforementioned medium at 37°C, 5% CO_2 and split upon trypsin digestion every three or four days using a splitting ratio of 1:10, avoiding cells to reach full confluence. The splitting of adherent cells consists in:

1. Removal of the "old" complete growth medium from the dish;

2. Rinse of the adherent cells with Phosphate Buffered Saline (PBS), generally 5 mL for a 10 cm Petri Dish;

3. Addition of 1 mL of Tripsyn-EDTA solution (0.25% Trypsin/0.53 mM EDTA in Hanks Balanced Salt Solution without calcium or magnesium23) and incubation (Temperature: 37°C**;** Atmosphere: air, 95%; carbon dioxide (CO2), 5%) for few minutes; the time of incubation in trypsin depends on the cellular type, typically 10 min for MCF10A;

4. Removing of the cells from the dish walls and dilution in fresh medium (generally 5 mL);

5. Centrifugation of the cellular suspension for 5 minutes at 1300 rpm;

6. Removal of the supernatant and re-suspension of the pellet containing cells in fresh growth medium;

7. Plating of the one tenth of the cells in a new dish and incubation (Temperature: 37°C**;** Atmosphere: air, 95%; carbon dioxide (CO2), 5%).

For the experiment of cell growth on the organic monolayer 30000 cells for each six wells (also containing the substrates) were plated, and incubated for 24 hours before the fixation and the SECM and fluorescence analyses.

Cell Fixation

The fixation of a sample is useful for preserving the sample in order to allow time consuming imaging experiments. In this case we were interested in the investigation of the spatial distribution of the cells in the sample and in their morphological analyses (vide Chapter 5): to facilitate the process of cell visualization and counting we fixed the sample and stained it with DAPI, a fluorophore which localizes in cell nuclei.

The protocol for cell fixation used in the present thesis is the following:

1. Removal of the medium growth from the dish;
2. Wash with PBS for three times;
3. Addition of glutaraldeyde (GDA 0.25% in PBS) to cover the whole substrate and incubation of the dish at 0°C for 20 minutes;
4. Addition of ethanolamine 150 mM and incubation at 0°C for 20 minutes;
4. Removal of the solution and 3 consecutive washes in PBS (at room temperature), each wash for the duration of 5 minutes;
5. The sample is conserved at 4 °C in PBS.

Between the passages 4 and 5 it's possible to perform the staining of the biological sample with DAPI according to following method:

i. Addition of DAPI (4°C in PBS stock solution1mg/mL 1:5000) enough to cove rthe entire substrate and incubation for 30 minutes in the dark if the cells are permeabilized or for 30 min if they are not;

ii. Removal of the DAPI solution and 3 consecutive washes with PBS for 5 minutes each in the dark;

iii. Removal of PBS and conservation of the sample at 4 °C in PBS.

Optical and Fluorescence Microscopy

For microscopy imaging, an epifluorescence microscope from Nikon (Chiyoda, Tokyo, Japan) equipped with ultrasensitive electron-multiplying CCD camera (EM-CCD 9100–13 from Hamamatsu, Hamamatsu Japan) was used with a resolution of 512 pixel x 512 pixel with a size of 16 x 16 μm. The microscope was enclosed in a homemade dark box to avoid interference from ambient light and was equipped with a motorized microscope
stage (Corvus, Marzhauser, Wetzlar, Germany) for sample positioning.
Long distance objective from Nikon (10x/0.30 DL17, 5 mm, 20x/0.40 DL13 mm, 50x) were used.

Statistical Analyses

A t-test is any statistical hypothesis test in which the test statistic follows a Student's t-distribution under the null hypothesis. It can be used to determine if two sets of data are significantly different from each other. Paired sample *t*-test is a statistical procedure used to determine whether the mean difference between two sets of observations is zero. We employed the stathistical analysis pakage of Origin 9.0 to perform the statistical analyses.

Cell Fixation Protocol Optimized for SECM Investigation

Fixation immobilizes antigens maintaining the cellular and subcellular structure. The fixation method depends on the sensitivity of the epitope and the antibodies themselves and may require some optimization.
Fixation can be achieved using crosslinking reagents such as paraformaldehyde and glutaraldehyde (GDA). This preserves the cell structure better, but may reduce the antigenicity of some cell components as the crosslinking can obstruct antibody binding.
Several fixation protocols were explored: below a step-by-step guide which describes the best three methods applied on our cultured cell line and the relative optical and SECM imaging results is reported.

Fixation with Methanol.

1. Grow cells to 50-60% confluency.

2. Aspirate the medium and cover cells to a depth of 2-3 mm with ice-cold 100% methanol.
3. Allow cells to fix for 15 minutes at -20°C.
4. Aspirate fixative, rinse three times in PBS for 5 minutes each.

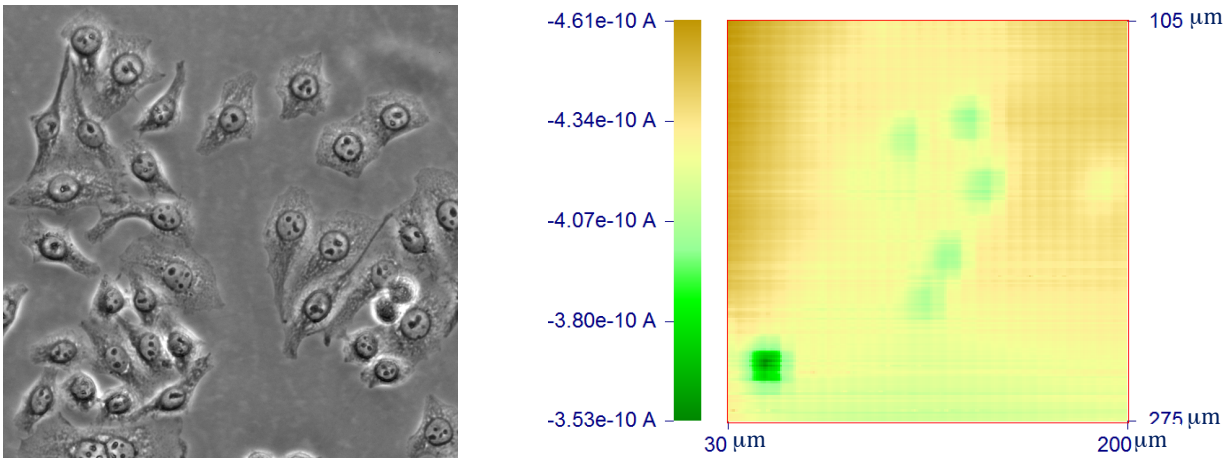

Fig. 1 Optical image (left) and SECM image (right)

Fixation with 2.5% GDA.

1. Grow cells to 50-60% confluency.
2. Aspirate the medium and cover cells to a depth of 2-3 mm with 2.5% glutaraldehyde in PBS for 2 h RT.
3. Aspirate fixative, rinse three times in PBS for 5 minutes each.

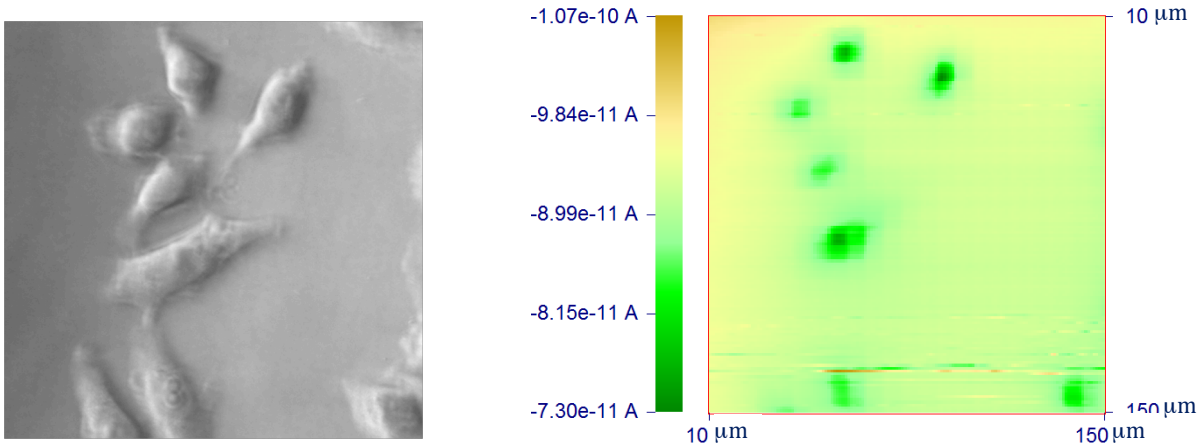

Fig. 2 Optical image (left) and SECM image (right)

Fixation with 0.25% GDA.

1. Grow cells to 50-60% confluency.
2. Aspirate the medium and wash cells twice with PBS
3. Cover cells with a solution of 0.25% glutaraldehyde in PBS. The dish was flooded with the appropriate fixative for 20 min at 0°C. Fixation was arrested by flooding the dish with 150 mM ethanolamine for 20 min at 0°C.
4. Aspirate fixative, rinse three times in PBS for 5 minutes each.

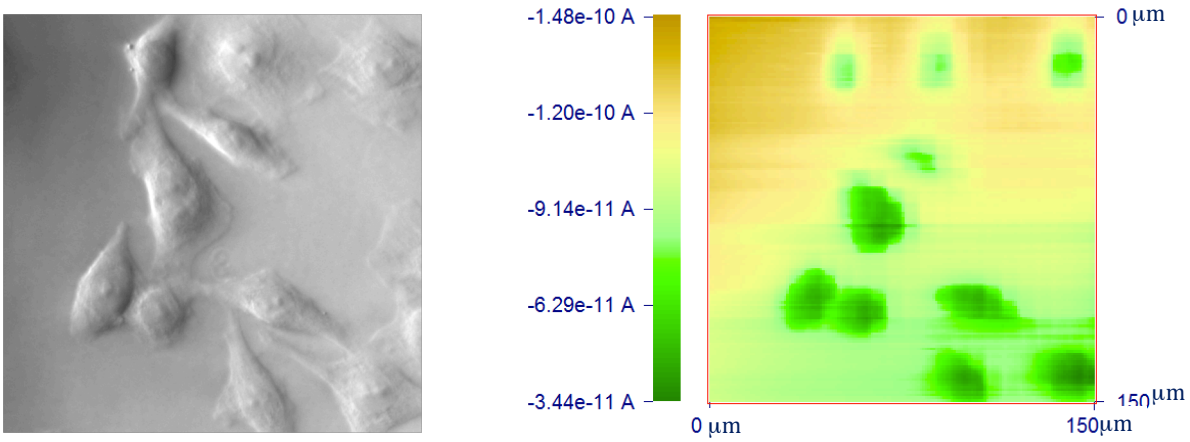

Fig. 3 Optical image (left) and SECM image (right)

This optimization step was essential since at first we were using methanol as fixative agent, but this lead to an undesired cell permeabilization. This affects SECM imaging capability, in fact the permeabilized cell could show both a positive or a negative feedback current as shown in **Fig. 1 (**right), where is possible to observe a cell acting as a conductive substrate. This behavior could be ascribed to the channels formed by the methanol that can be filled with the redox mediator. The protocol chosen was that with GDA and ethanolamine, which proved to give the best results.

References

1. http://www.lgcstandards-atcc.org

4. Cell Morphology on Organic Monolayer Investigated by Scanning Electrochemical Microscopy

Many biological processes are influenced by cell adhesion such as embryogenesis [1], leukocyte extravasation during an immune response [2] and invasion-metastasis cascade of tumors [3]; respectively referring to the fields of development, health and the pathogenesis of disease. Besides, the importance of cell adhesion plays a key role in the development of implantable biomedical devices, which must be accepted by the host organism [4,5] and produce a correct integration. Cells morphology displays significant modifications during adhesion as they spread increasing the area in contact with the surface, whereas they show a spherical shape in suspension, in absence of external mechanical contacts. The basic process of adhesion has been described through a number of models, trying to include the biophysics and biomechanics underlying cell behavior applied to system ranging from a single-cell to more complex tissues. [6-9]

The study of cell shape is believed to provide understanding also on an important cellular mechanism, protrusion control and thus migration. So far the two opposite forces that determine cell protrusion rate are the pressure deriving from actyn polymerization and membrane tension. In a recent work Gabella et al. [10], used osmotic treatments to modify membrane tension and protrusion rate in migrating keratocytes and also modulate the topography of the substrates in order to find novel relationships between the 3D cell shape and its dynamics. They reported that the leading edge of the cell can be considered as a triple interface between substrate, membrane and extracellular medium and that the protrusion rate could be extracted by the contact angle between the substrate and the membrane, as it indicates the load on actin polymerization.

The interest on cell contact angle as a fundamental parameter to characterize cell adhesion has grown considerably and is found in a number of studies. [11-13] This kind of approach, aims to exploit the theories describing surface wetting phenomena in physics, in an attempt to find a quantitative description of cell adhesion. [14,15] In this work, we tried to obtain a representative geometrical parameter of cell morphology, calculated with a finer process with respect to cell contact angle. In fact contact angle is obtained by a measurement on a single profile, which proved to be effective for a water drop, but is probably a limited approach to characterize a cell in its entirety and over- approximates this complex biological system. In our case, a statistics on all plane inclinations of single cell 3D surface, whose morphology was measured by SECM, was carried out. Many cells (almost 100 overall) were imaged for three different surfaces and the resulting angles obtained were compared, together with others geometrical parameter, to evaluate cellular responses to chemically controlled surfaces of 2D materials with a well controlled roughness (see chapter 3).

Why SECM

In this study cell fixation was used to preserve the morphology of the sample, so that time consuming images were allowed (see Chapter 3). An optimization step was required in order to avoid cell permeabilization that can negatively affect the imaging capability of SECM, caused by the redox mediator permeation in the channels formed through the cell membranes. The redox mediator permeation in the membrane does not allow for a precise measurement of the cell morphologies as the hindering of the diffusion, which reports for their topography, is affected by the diffusion of the specie in the cells. This scanning probe microscopy technique is particularly suitable for the investigation of biological samples, as described in chapter 1. Among the reasons accountable for this are: i) SECM high throughput capability with respect to other SPM techniques (several micron for second are scanned) and ii) it is independent from the use of a stain, that is usually toxic for cells and not always able to mark the real topography of a cell. Moreover SECM works in physiological solution and it can be performed on living cells.

Sample Characterization by Scanning Electrochemical Microscopy: Experimental and Results

The investigation of the samples through Scanning Electrochemical Microscopy was executed by SECM imaging in constant height mode and by probe approach curves (PACs). These techniques consist respectively in scanning a probe in the XY plane at a constant value of Z and register the current variations underneath, and bringing a probe near the surface to determine its reactivity (see chapter 2 for details). At least 20 SECM images were performed on each sample (MCF10A cells grown on mono-molecular layers of 6T, P5 and PDI8-CN2), in order to study how the different chemical functionalities influenced cell response, by evaluating their shape, structure and size. Experimentally this required the acquisition of a SECM image, that in order to be acceptable for the morphology analysis should not have noise interferences and should scan whole cells well isolated from others. We took into account at least 30 cells per sample, a sufficient number to perform a valid statistical analysis. In this respect, a new procedure was developed and employed to assess cell morphology in a reproducible way. PACs were necessary to transform the measured variable current into a distance, required for the morphological study. Furthermore, this technique was of fundamental interest to evaluate substrates reactivity/conductivity and, by repeating these measurements at different times, it was possible to monitor the molecular thin films degradation in

the solution of Phosphate Buffer Saline, where all the samples were submerged and conserved from the first experiment (see Chapter 3).

SECM Imaging of Cells on Organic Monolayers

For this study, cells were fixed with a combination of glutaraldehyde as fixing agent and ethanolamine to arrest fixation (protocol reported at the end of the chapter 3), glutaraldehyde works as a cross-linker of the cell proteins, thanks to its two aldehyde functional groups and the alkane chain, that consent to reach distant protein residues and link them, this fixation offers a tightly linked product, suitable for studying its structure.
Fixed cells were imaged by SECM through amperometric feedback mode measurements, in order to investigate how different chemical properties of the substrate were influencing cell morphology. It was necessary to perform measurements on cells after fixation, since not only storing and handling of the samples was noticeably facilitated, but also because activities linked to the living cell behavior (metabolism, ionic exchange etc.) could produce a signal difficult to separate from that of the morphology alone.

At the beginning of every experiment, the working electrode tip was polished on a 0,1 μm diamond film disk attached on a glass support and put in a sonic bath for several seconds. This procedure was repeated any time the substrate was changed or the tip crashed on the substrate surface, in order to remove molecules that could be absorbed on the probe surface, causing electrode fouling that would influence negatively image resolution, and in general any time that from experience it was possible to notice electrode fouling.
The electrochemical cell in these experiments was composed by a 35 mm Ø Petri dish, on its bottom, the sample (usually a square of 1 cm^2) was glued with a Gel-Pak® bioadhesive tape and the dish was fixed to the optical microscope plate, in order to avoid any movement that could affect SECM imaging.
The dish was then flooded with the electrolytic solution of redox mediator (FcCOOH 1 mM in PBS), the use of PBS buffer was essential to control the pH, in order to obtain reproducible data, since this parameter influences the electron transfer kinetic rates.
Lastly a working (Pt 10 μm Ø and RG = 10), a reference Ag/AgCl (KCl 3M) and a Pt counter electrode were positioned, always making certain that they were immersed in the solution, and well connected. Once the UME was immersed inside the solution a Cyclic Voltammetry (CV) was performed, in order to test if the electrode was well polished and to control the UME geometry.

CV were performed in a potential range E = 0-0,6 V, and a scan rate of 20 mV/s. A typical CV obtained for our experiment is reported in **Fig. 1**.

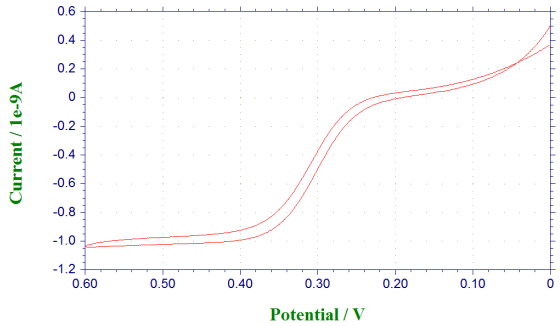

Fig. 1 Cyclic Voltammetry of 1 mM FcCOOH in PBS 1x. E = 0-0,6 V; Scan rate: 20 mV/s; WE: Pt 10 µm Ø; RE: Ag/AgCl; CE: Pt.

If a typical sigmoidal shape was obtained as expected, the experiment was carried on and the probe was approached performing a Probe Approach Curve (PAC). Usually two consecutive PACs were performed. A first faster PAC (scan rate 50 µm/s) was performed in order to approach the surface quickly. After this the UME was retracted (usually by 300 µm) and a slower PAC (scan rate 5 µm/s) was performed, this scan rate consented a more accurate measurement. Usually the PAC were set to stop automatically when the current at the tip reached the 75% of its initial current in the bulk, but they could be manually stopped as well. PAC were all conducted at E = 0,45 V vs Ag/AgCl, a potential sufficient to oxidize the redox mediator (FcCOOH) with a rate higher than mass transfer.

MCF10A on Pentacene (P5)

PACs were performed on Pentacene, right after it was immersed in the PBS solution containing the electrolyte for the first time, time zero (t_0). These measures were used to obtain the rate constants for electron transfer at the substrate as well to approach the surface. In **Fig. 2** a representative PAC obtained for P5 at t_0 is shown. The tip current I_T is normalized on the current in the bulk $I_{T,\infty}$.

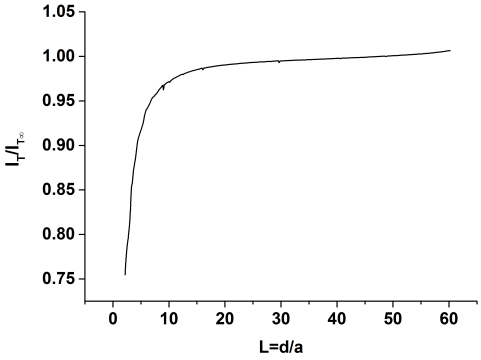

Fig. 2 PAC on P5 at t_0. E = 0,45 V. Scan rate: 5 µm/s.

We can observe that the approach on this substrate follows a negative feedback behavior.

Once the substrate was approached, the UME was retracted by 10 - 20 µm, this distance was enough not to crash on cells during the scansion. Then a SECM image was performed, the scan was started from the point were the tip approached and covered an area in the xy plane usually of the size of 400 µm x 400 µm at a scan rate of 16.7 µm/s. In both these SECM images (**Fig. 3**) is evident that cells show a more negative feedback due to their topography.

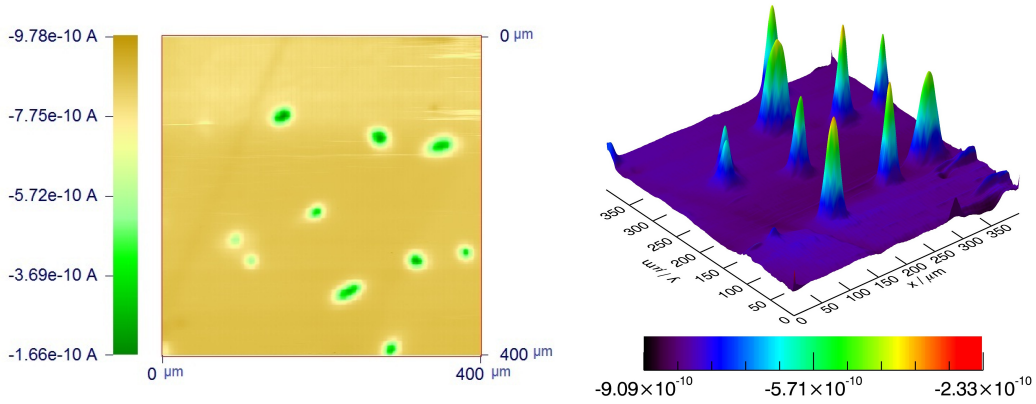

Fig. 3 SECM images 400 µm x 400 µm of MCF10A on P5. Scan rate: 16.7 µm/s. 2D (left) and 3D (right). Pt 10 µm, 1mM FcCOOH in PBS, E=0,45V vs Ag/AgCl.

From **Fig 3**, it is also appreciable that it is possible to image the morphology of cells in different phases for example during the cellular division. These cells were not considered in the data manipulation, in fact since they are overlapped, their morphology and shape is not independent from their interaction and is typical of cytokinesis phase. With respect to the other samples studied, cells on P5 resulted the most numerous, suggesting a higher proliferation that was confirmed by epifluorescence microscopy measurements (see Chapter 3).

MCF10A on α-Sexithiophene (6T)

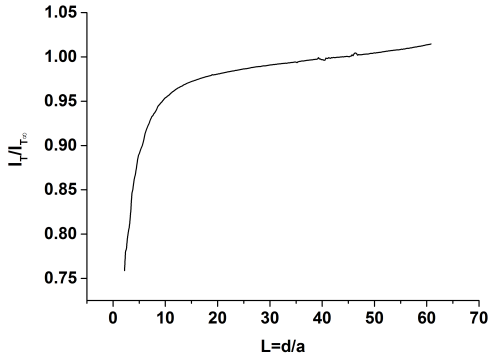

Fig. 4 PAC on 6T at t_0. Approach rate: 5 µm/s. Pt 10 µm, 1mM FcCOOH in PBS, E=0,45V vs Ag/AgCl.

A PAC carried out on α-Sexithiophene is reported in **Fig. 4**, this substrate shows a negative feedback.

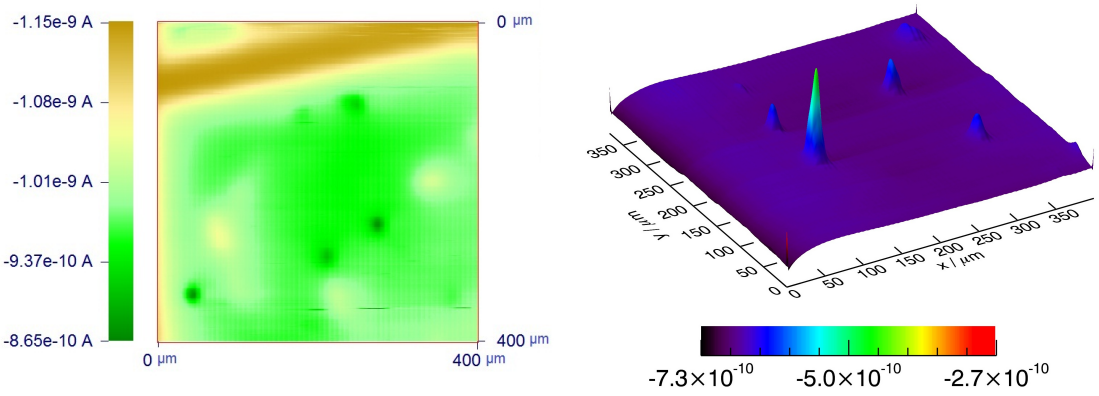

Fig. 5 SECM images 400 µm x 400 µm of MCF10A on 6T. Scan rate: 16.7 µm/s. 2D (left) and 3D (right). Pt 10 µm, 1mM FcCOOH in PBS, E=0,45V vs Ag/AgCl.

Besides, in **Fig. 5** it can be noticed that even if the morphology of this substrate proved to be homogeneous by AFM measurements, the functionality of the substrate displays microstructured zones that show higher conductivity than the rest of the surface. This characteristic can be effectively investigated by SECM imaging. This behavior is typical throughout the substrate, the reason why in the SECM image in **Fig. 5** it is exhibited in such an evident way, is due to the lower

working distance at which the scan was performed, which proved to be effective to reveal the changes in conductivity/reactivity of the substrate.

MCF10A on Perylene (PDI8-CN2)

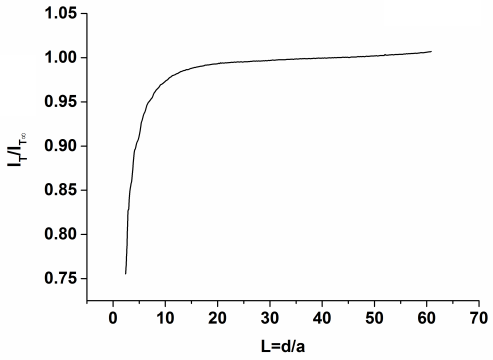

Fig. 6 PAC on PDI at t_0. Approach rate: 5 µm/s. Pt 10 µm, 1mM FcCOOH in PBS, E=0,45V vs Ag/AgCl.

A PAC carried out on PDI8-CN2 is reported in **Fig. 6**, this substrate shows a negative feedback. Fixed cells act as a non-conductive substrate, from SECM images of MCF10A on PDI reported in **Fig. 7**, is evident that the substrate being a semiconductor has a higher rate constant of electron transfer than cells, as expected.

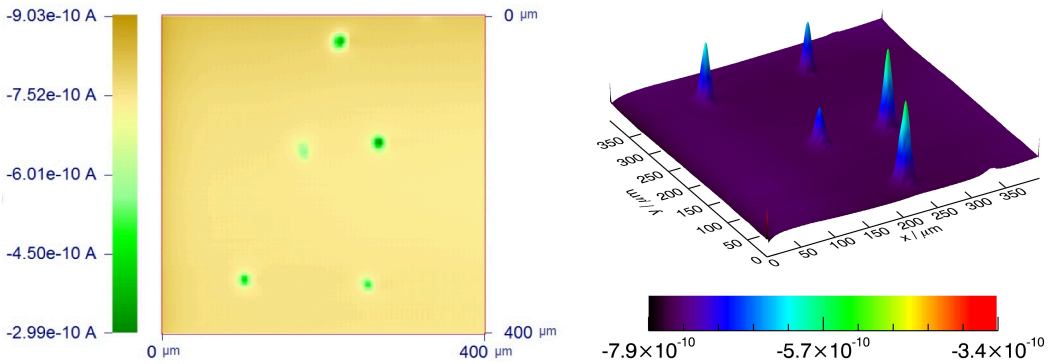

Fig. 7 SECM image 400 µm x 400 µm of MCF10A on PDI. Scan rate: 16.7 µm/s. 2D (left) and 3D (right). Pt 10 µm, 1mM FcCOOH in PBS, E=0,45V vs Ag/AgCl.

Data Treatment

In order to obtain information regarding the morphology of the cells, all the current values recorded by SECM measurements had to be transformed into distances.

Fitting Procedures

MIRA software by Prof. Wittstock (http://www.uni-oldenburg.de/chemie/pc2/pc2forschung/secmtools/mira/) was used for fitting all current approach curves and for plotting the images. Approach curves were fitted by Cornut-Lefrou equations for purely negative feedback, purely positive feedback and for finite sample kinetics, tip/substrate separations and heterogeneous rate constants were accordantly evaluated. [16] A first order heterogeneous rate constant in cm per second (k_{eff}) can be determined, using the dimensionless constants obtained in the fitting procedures and reported in the text, accordingly to the following equation:

$$k=k_{eff}\, r_T/D$$

where r_T is the electrode radius and D the diffusion coefficient of the redox species. A typical experimental approach curve and its relative fitting obtained with the procedure just mentioned are depicted in **Fig. 8**.

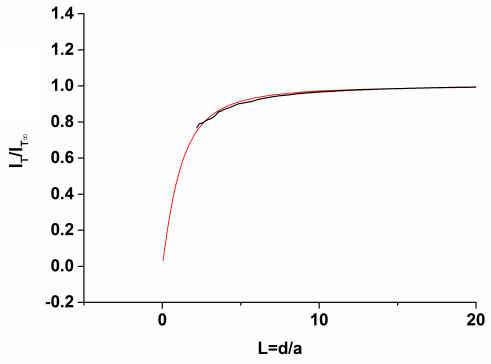

Fig. 8 Experimental approach curve (black line) and fitted curve (red line) of the tip to 6T in presence of FcCOOH 1mM in PBS.

The following procedure, performed with the software package Origin 9.0 (specific for scientific graphing and data analysis) was adopted for every SECM image acquired.

The Bin file of the SECM image produced by the CHI software was converted to text, in this way an ASCII file of three columns (xyz) was generated, where the first two columns were the x and y distances travelled by the probe in µm and the z represented the current in nA. The ASCII file was

imported in Origin and the currents were normalized dividing by the bulk current. To the normalized currents was subtracted the baseline current (the current measured at the substrate).
In **Fig. 9** is shown how the fitted approach curve can be divided in short segments, which in turn can be fitted by a linear equation.

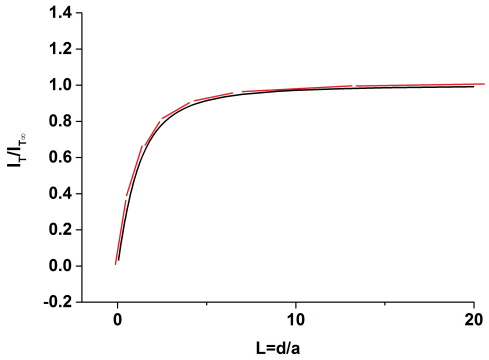

Fig. 9 Fitted approach curve (black line) and fitting straight segments (red) of the tip to 6T in presence of FcCOOH 1mM in PBS.

We considered the interval of the curve included between the minimum value of current measured on a cell and the current measured on the substrate in the proximity of the same cell. In the obtained range, we applied a linear fitting (Fit Linear) operation. The currents previously obtained, were divided by the slope (nA/µm) of the fitted straight line (taking into account the information that L=d/a see Chapter 2). The last operation allows the transformation of the currents registered into distances.

Morphology Characterization Procedure

At this stage, a all the coordinates in micrometers of the cells was exported from Origin and elaborated using the software for image and data treatment Gwyddion. [17] The morphological analysis was performed on SECM images recorded for each cell. Initially some operations for the flattening of the image were applied, these were needed in order to overcome the defects intrinsic to every image such as the tilt of the sample and to reduce irregularities due to noise or other imaging errors. This procedure lead to morphological images of MCF10A cells on SIO_x substrates covered with mono-molecular layers of organic molecules (specifically α-Sexithiophene, Pentacene, PDI8-

CN2). In **Fig. 10**, a representative morphological image derived from SECM imaging of cells on 6T is presented in its two-dimensional and three-dimensional form.

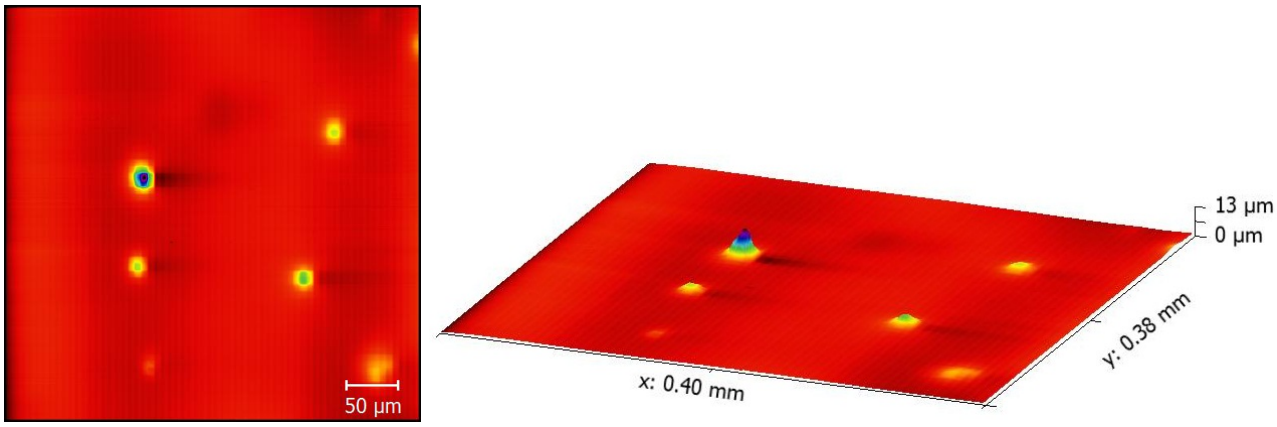

Fig. 10 Representative morphological image derived from SECM image and displaying MCF10A on 6T in 2D (left) and 3D (right).

From **Fig. 10** is clear as the substrate is flat and cells were sufficiently far apart not to influence their respective shapes. In **Fig. 11** an emblematic illustration of cells on P5 is displayed in 2D and 3D.

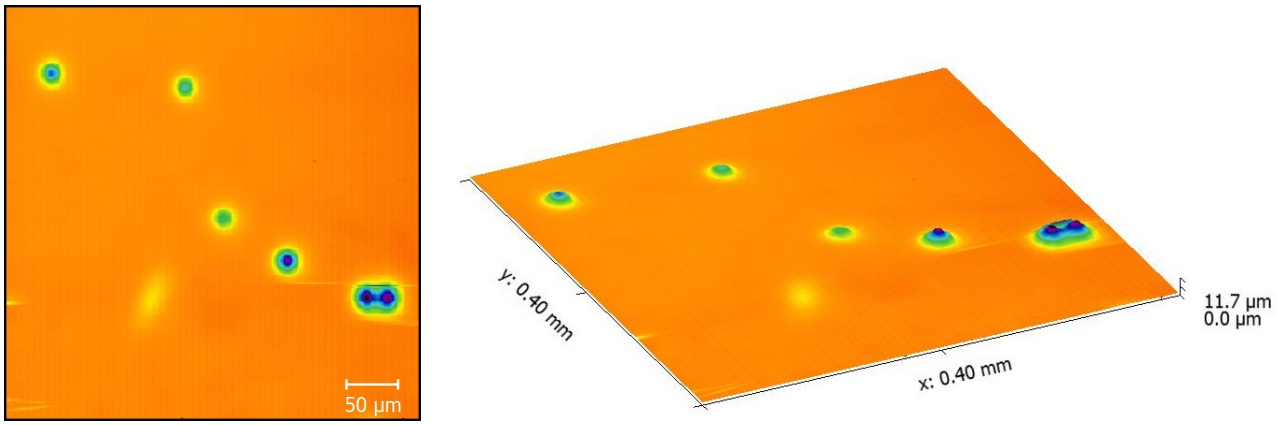

Fig. 11 Representative morphological image derived from SECM image and displaying MCF10A on P5 in 2D (left) and 3D (right).

In **Fig. 11**, among those imaged, the two dividing cells were not considered for data treatment and morphology study in our work since the results would be clearly altered by their interaction. Nevertheless it is worth noting that the two cells, however superimposed, are resolved by our technique and are well distinguishable in the SECM image obtained.

Below a representative image of cells imaged on PDI8-CN2, obtained after applying the operations described before, is reported in **Fig. 12** both in 2D and 3D.

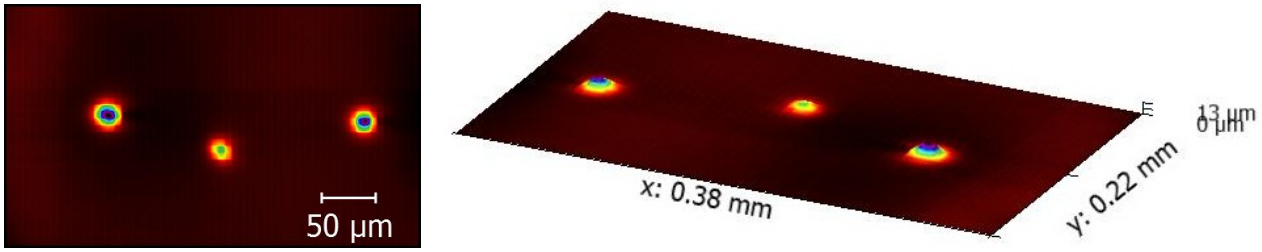

Fig. 12 Representative morphological image derived from SECM image and displaying MCF10A on PDI8-CN2 in 2D (left) and 3D (right).

It must be pointed out, that the z axis scale concerning the 3D image is displayed a little larger in proportion than its x and y counterparts, this is due only to graphic reasons, since a proportioned scaling would make cells three-dimensionality hard to visualize. Therefore in reality cells appear even flatter.

Next step consisted in selecting a single cell from the image. In **Fig. 13** a 3D image of a cell obtained after cropping the image in **Fig. 13** is shown.

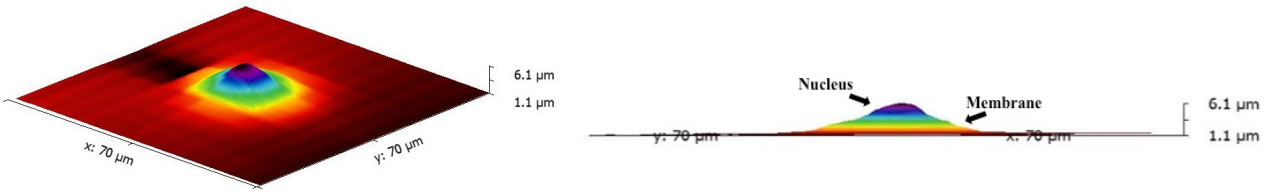

Fig. 13 SECM image displaying a single-cell MCF10A on PDI8-CN2 in 3D (left). Cell profile projection on the xz plane.

This image is explicative of the morphology of cells object of this study. The two major shape characteristics, namely the nucleus and the base of the cell membrane, clearly stand out. Besides from the profile obtained by the projection of the 3D image on the xz plane the angles defining the final cell shape are clearly visible.

Using the threshold process, the area of the cell was manually selected under a mask, then the tool *Statistical Quantities* output a number of parameters among which the Maximum height and the

Surface area. This method was used to calculate all the areas relative to the cells imaged and their maximum height.

At this point, through the tool *Extract Profile*, a profile of the cell was marked. Since cells in this study did not show a particular anisotropy, the approximation made by selecting one profile was considered acceptable for our purposes. The profile selected was exported as a text file and fitted with Fityk, a curve fitting application designed to fit with Gaussian curves. A typical fitting obtained for a cellular profile is displayed in **Fig. 14**, the profile extracted from the cell is represented by the green dotted line, while the fitting obtained is the yellow curve.

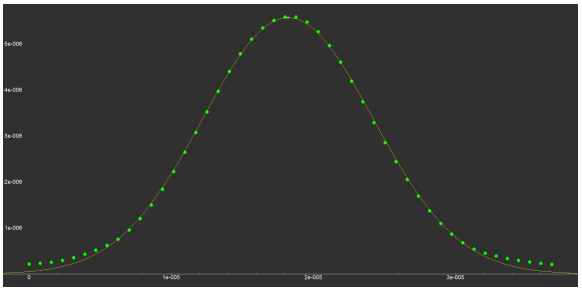

Fig. 14 Extracted cell profile (green dotted line) and fitting curve obtained (yellow line).

From the fitting curve obtained, the half width half maximum and the maximum height were acquired as significant parameters to describe the cellular shape.

In order to have a fine descriptor of cellular morphology, we applied a statistics function of Gwyddion, namely *Slope Distribution*. *Slope Distribution* calculates a distribution of derivatives, that is the horizontal and vertical coordinate on the resulting data field in the horizontal and vertical derivative, respectively. [17] In our case the slopes were calculated as central derivatives (with one side on the borders of the image).

Facet and plane inclinations of the whole surfaces are displayed as the spherical angles (ϑ,φ) of the plane normal vector. Geometrically angle ϑ is the angle between the upward direction and the normal, this means that $\vartheta = 0$ for horizontal facets and it increases with the slope. It is always positive. Angle φ is the counter-clockwise measured angle between axis x and the projection to the xy plane, as displayed in **Fig. 15**.

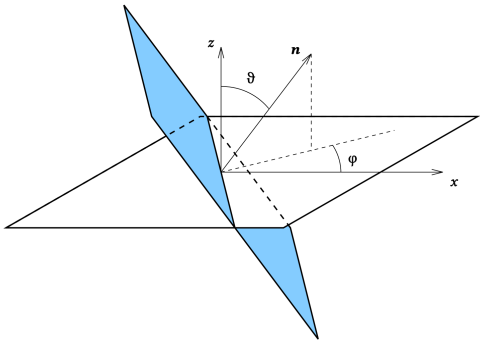

Fig. 15 Surface facet (displayed blue) orientation measured as the counterclockwise angle from x-axis to the projection of facet normal vector **n** to xy plane. [17]

With *Slope Distribution* a graphs representing the distribution of the inclination angle ϑ from the horizontal plane can be plotted. ϑ is expressed in the following formula:

$$v = \left(\frac{dz}{dx}, \frac{dz}{dy}\right), \qquad \nu = |v|, \qquad \vartheta = \operatorname{atan}\nu$$

The graph obtained was exported as a text file and fitted with Fityk. The fitting was carried out using the least possible of Gaussian curves. A typical slope distribution curve for a cell on PDI8-CN2 and its relative fitting curve in yellow are shown in **Fig. 16**, the slope distribution is reported as green dotted line, the Gaussian curves used (4 in this case) are red and the fitting obtained is the yellow curve.

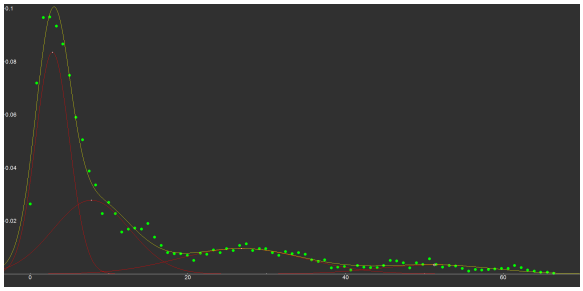

Fig. 16 Slope distribution (green dotted line), Gaussian curves used for the fitting (red line) and fitting curve obtained (yellow line).

The center of each gaussian curve represents the most characteristic inclination angles measured in the single-cell image analyzed. The first peak at low angles (<10°) with the highest counts, was appointed to the substrate noise, while the others were collected for each substrate analyzed in this study (6T, P5, PDI8-CN2). All the angles extracted by this procedure for each substrate, were analyzed with Origin and a frequency count was performed. The resulting data reported in a column

graph showed the distribution of the angles measured, this distribution was fitted with two gaussian curves, in order to obtain the most probable angles in cells morphology on a particular surface.

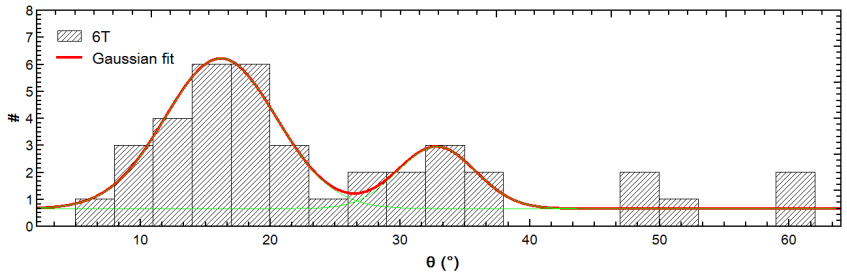

Fig. 17 Frequency count of the inclinations angles obtained for MCF10A cells on 6T. Gaussian curves used for the fitting (green line) and fitting curve obtained (red line).

In **Fig. 17**, the frequency count of the inclinations angle ϑ, for the cells imaged on the sample 6T is shown. The fitting curve highlights two peaks centered respectively on 16° (± 4) and 33° (± 3), these are the most common angles ϑ for MCF10A cells on α-Sexithiophene. The frequency count allowed to extrapolating the most representative inclinations angle found in cell morphology on PDI8-CN2 (**Fig. 18**). MCF10A on this sample have two characteristic angles: 16° ± 4 and 41° ± 3.

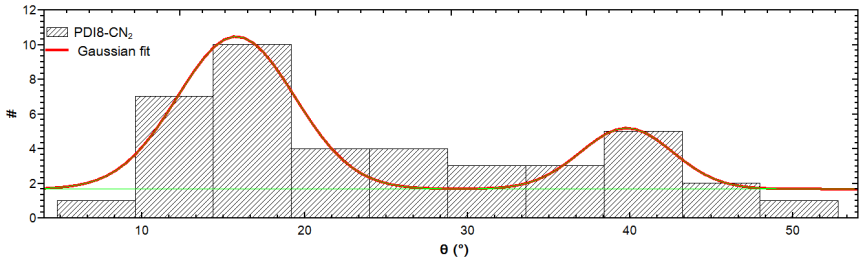

Fig. 18 Frequency count of the inclinations angles obtained for MCF10A cells on PDI8-CN2. Gaussian curves used for the fitting (green line) and fitting curve obtained (red line).

The distribution of the inclination angles measured for cells on Pentacene are reported in **Fig.19**, also in this case the cell morphology exhibits two typical angles: 18° ± 11 and 48° ± 6.

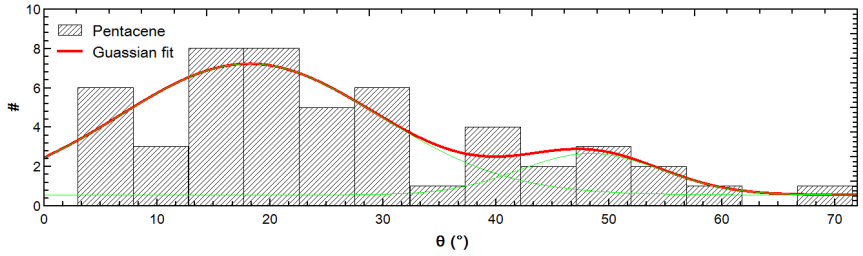

Fig. 19 Frequency count of the inclinations angles obtained for MCF10A cells on P5. Gaussian curves used for the fitting (green line) and fitting curve obtained (red line).

The results obtained by the procedure described so far, are a series of parameters related to cell morphology, namely characteristic inclination angles, cell area projected on the surface, the half width measured at half maximum and lastly the maximum height. Combining this information it was possible to obtain an accurate description of the typical morphology shown by MCF10A cells on the organic monolayers investigated. These data were compared, in order to verify how the substrate different chemistry influenced cell response.

After statistical data treatment (one-way ANOVA test, vide infra), the averaged cellular area on each substrate was calculated and compared, the results are shown in a column graph in **Fig.20**, and resumed in **Table 1**. **Fig. 20** highlights the similar surface occupied by cells on PDI8-CN2 and 6T, whereas that on P5 is the widest, in line with the averaged nucleus area calculated (see Chapter 3).

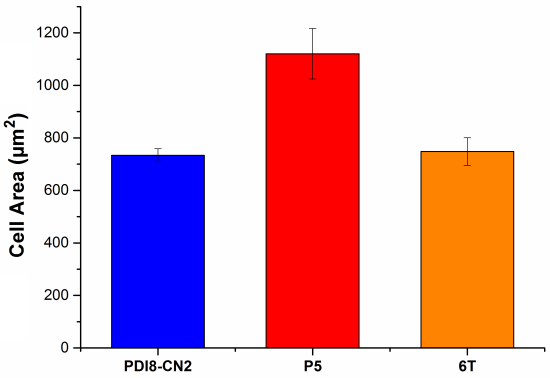

Fig. 20 Averaged cellular area displayed by MCF10A cells on PDI8-CN2, P5 and 6T.

The ANOVA test confirms the null hypothesis that averaged cell area on PDI8-CN2 and 6T are not significantly different, on the other hand they are both significantly different from the same quantity measured on P5. The considerably higher surface area, almost 50 % bigger (see **Table 1**), occupied by cells on Pentacene implies that cell-substrate affinity is higher on this sample with respect to the others tested and consequently adhesion on this mono-molecular layer is fostered in respect to the others.

Table 1

	Averaged Cell Area (μm^2)
MCF10A on PDI8-CN2	734 ± 25
MCF10A on P5	1121 ± 96
MCF10A on 6T	748 ± 53

As far as the maximum heights are concerned (**Fig. 21**, **Table 2**), the F-test revealed that these quantities are not significantly different regardless of which couple is selected.

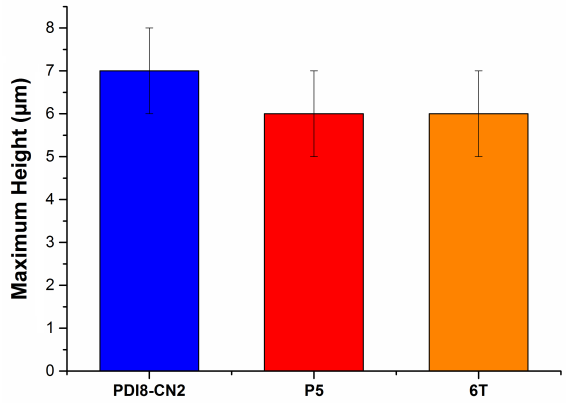

Fig. 21 Averaged maximum height displayed by MCF10A cells on PDI8-CN2, P5 and 6T.

The great correspondence between these values means that our substrates produced little to none effects on this geometrical parameter, which in turn is not indicative of any change in cell behavior. Since cells maximum height reflects the nucleus height in the direction normal to the surface, it is possible to assert that, on the substrates studied, the nucleus height is not influenced by the different chemical functionalities at the surface.

Table 2

	Averaged Maximum Height (µm)
MCF10A on PDI8-CN2	7 ± 1
MCF10A on P5	6 ± 1
MCF10A on 6T	6 ± 1

The averaged half widths at half maximum are displayed in the graph in **Fig. 22**, and values reported in **Table 3**.

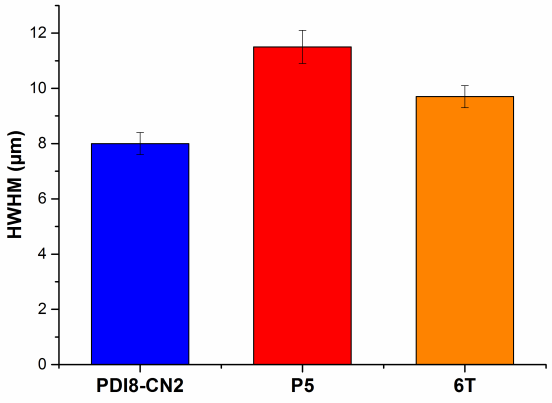

Fig. 22 Averaged Half Width Half Maximum displayed by MCF10A cells on PDI8-CN2, P5 and 6T.

The statistical data treatment, in this case indicates that any couple of samples considered, the mean HWHM calculated are significantly different between them. HWHM of MCF10A cells proved to be affected by the different surfaces analyzed in this work. Regarding the geometry of the cell, this parameter describes the cell membrane shape around the nucleus. A higher HWHM at a constant height entails a greater cell volume.

Table 3

	Averaged Half Width Half Maximum (µm)
MCF10A on PDI8-CN2	8.0 ± 0.4
MCF10A on P5	11.5 ± 0.6
MCF10A on 6T	9.7 ± 0.4

Typical inclination angles shown by cells on substrates analyzed are resumed in **Table 4**. It can be noticed that two main inclination angles have been calculated for cells on each sample. The lower angle is the same for all three substrates. However if the characteristic higher angles shown by PDI8-CN2 and P5 are comparable (respectively 41 ± 3 and 48 ± 6), they are both different from that of cells on 6T which is lower (33 ± 3).

Table 4

	ϑ (°)

MCF10A on PDI8-CN2	16 ± 4	41 ± 3
MCF10A on P5	18 ± 11	48 ± 6
MCF10A on 6T	16 ± 4	33 ± 3

In **Table 5** all the geometrical parameters taken into account to evaluate cellular shape changes are resumed. As previously mentioned, the combination of these constants allowed us to recreate morphologies that are typical of MCF10A cells on PDI8-CN2, P5 and 6T.

Table 5

	Area (μm^2)	Max (μm)	HWHM (μm)		ϑ (°)
PDI8-CN2	734 ± 25	7 ± 1	8.0 ± 0.4	16 ± 4	41 ± 3
P5	1121 ± 96	6 ± 1	11.5 ± 0.6	18 ± 11	48 ± 6
6T	748 ± 53	6 ± 1	9.7 ± 0.4	16 ± 4	33 ± 3

A sketch reproducing the archetypical cellular shapes analyzed on different organic monolayers is shown in **Fig. 23**. Cells display all the same height whereas the shapes and the surface area occupied are influenced by the substrates. The lower inclination angles, similar for all the cells, account for the angle measured at the membrane interface in close proximity of the substrate at the leading edge whereas the higher angles describe membrane shape around the nucleus. Cells on Pentacene have the highest volume, as a combination of the biggest projection area and the highest HWHM. This morphology indicates a good affinity for P5 surfaces, since cells are well spread and adhesion is higher. The archetype cell on 6T occupies a reduced surface if compared to that on P5, its width at half maximum is intermediate between the other two. This cell is bell shaped, in fact shows a lower inclination angle relative to the portion of membrane close to the nucleus. The shape is swollen with respect to the cell on P5. Lastly the cell on PDI8-CN2 has a contact area comparable to the one on 6T, its nucleus is shaped as a slightly elongated spheroid. In this case the cell is shrunk, the membrane is tightly adhered to the nucleus and overall the cell volume is reduced.

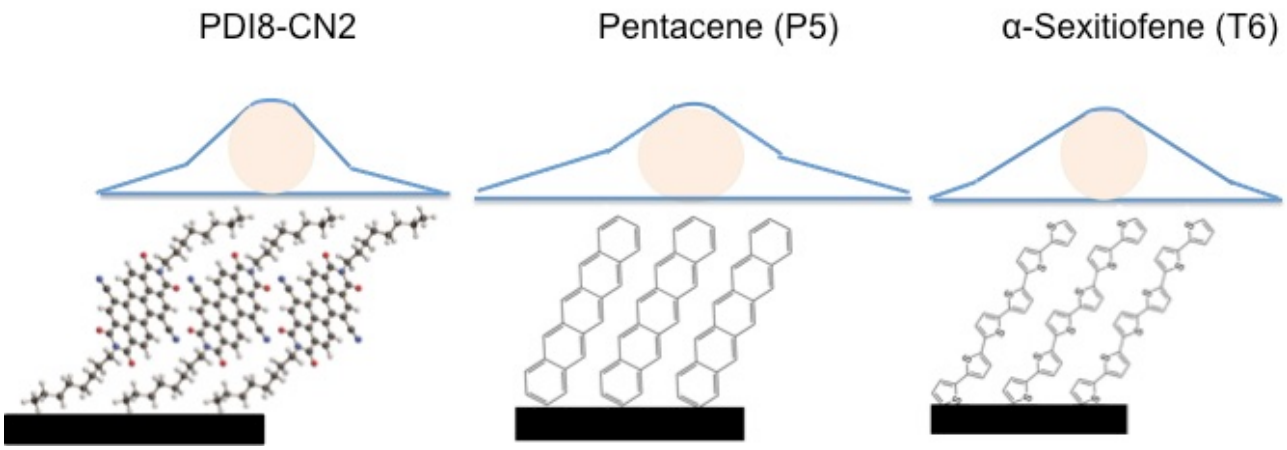

Fig. 23 Morphologies displayed by MCF10A cells on PDI8-CN2, P5 and 6T.

B. Statistical Analyses

A one-way analysis of variance (one-way ANOVA) is a technique that can be used to test if two sample the same mean values. It can be used to determine if two sets of data with different size are significantly different from each other. The ANOVA applies an *F-test*, which is any statistical test in which the test statistics has an F-distribution under the null hypothesis that datasets have the same mean values. It is based on the statistical analysis of variances of two samples, to be statistically different the variance of a dataset should not be significantly different than the variance between the two datasets. We employed the statistical analysis pakage of Origin 9.0 to perform the statistical analyses.

References

1. Barone, V.; Heisenberg, C.-P. Cell adhesion in embryomorphogenesis. *Curr. Opin. Cell Biol.* 24, 148−153. (2012)
2. Middleton, J.; Patterson, A. M.; Gardner, L.; Schmutz, C.; Ashton, B. A. Leukocyte extravasation: chemokine transport and presentation by the endothelium. *Blood*, 100, 3853−3860. (2002)
3. Valastyan, S.; Weinberg, R. A. Tumor metastasis: Molecular insights and evolving paradigms. *Cell*, 147, 275−292. (2011)
4. Statz, A.; Barron, A.; Messersmith, P. Protein, Cell and bacterial fouling resistance of polypeptoid-modified surfaces: effect of side chain chemistry. *Soft Matter*, 4, 131−139. (2008)
5. Tang, L.; Jennings, T.; Eaton, J. W. Mast cells mediate acute inflammatory responses to implanted biomaterials. *Proc. Natl. Acad. Sci. U. S. A.* 95, 8841−8846. (1998)
6. Hallab, N. J.; Bundy, K. J.; O'Connor, K.; Moses, R. L.; Jacobs, J. J. Evaluation of Metallic and Polymeric Biomaterial Surface Energy and Surface Roughness Characteristics for Directed Cell Adhesion. *Tissue Eng.*, 7, 55−71. (2001)
7. Parsons, T. J.; Horwitz, A. R.; Schwartz, M. A. Cell adhesion: integrating cytoskeletal dynamics and cellular tension. *Nat. Rev. Mol. Cell Biol.*, 11, 633−643. (2010)
8. Sampson, N. S.; Mrksich, M.; Bertozzi, C. R. Surface molecular recognition. *Proc. Natl. Acad. Sci.* U. S. A., 98, 12870−12871. (2001)
9. Brodland, G. W. The Differential Interfacial Tension Hypothesis (DITH): a comprehensive theory for the self-rearrangement of embryonic cells and tissues. *J. Biomech. Eng.*, 124, 188−197. (2002)
10. Gabella, C.; Bertseva, E.; Bottier, C.; Piacentini, N.; Bornert, A.; Jeney, S.; Forró, L.; Sbalzarini, I. F.; Meister, J. J.; Verkhovsky, A. B. Contact Angle at the Leading Edge Controls Cell Protrusion Rate. Curr. Biol., 24, 1126−1132. (2014)
11. Maître, J.-L.; Berthoumieux, H.; Krens, S. F.; Salbreux, G.;Jülicher, F.; Paluch, E.; Heisenberg, C. P. Adhesion functions in cell sorting by mechanically coupling the cortices of adhering cells. *Science*, 338, 253−256. (2012)
12. Fouchard, J.; Bimbard, C.; Bufi, N.; Durand-Smet, P.; Proag, A.; Richert, A.; Cardoso, O.; Asnacios, A. Three-dimensional cell body shape dictates the onset of traction force

generation and growth of focal adhesions. *Proc. Natl. Acad. Sci.* U. S. A. , 111, 13075−13080. (2014)

13. Simson, R.; Wallraff, E.; Faix, J.; Niewöhner, J.; Gerisch, G.; Sackmann, E. Membrane bending modulus and adhesion energy of wild-type and mutant cells of Dictyostelium lacking talin or cortexillins. *Biophys*. J., 74, 514−522. (1998)
14. Bruinsma, R.; Sackmann, E. Bioadhesion and the dewetting transition. C. R. *Acad. Sci., Ser. IV: Phys., Astrophys.*, 2, 803−815. (2001)
15. Sackmann, E.; Bruinsma, R. F. Cell adhesion as wetting transition? *ChemPhysChem*, 3, 262−269. (2002)
16. R. Cornut and C. Lefrou, *Journal of Electroanalytical Chemistry*, , 608, 59-66. (2007)
17. Gwyddion Scan Probe Microscopy data analysis software. Gwyddion User Guide. <http://gwyddion.net/>, © David Neas and Petr Klapetek.

5. Novel Method for the Fabrication of SECM Nanoelectrodes

In the last years, Scanning Probe Microscopies, such as Scanning Tunneling Microscopy (STM), Atomic Force Microscopy (AFM) and Scanning Electrochemical Microscopy (SECM) have been increasingly used to investigate important biological issues. [1-3]

In order to best apply to the characteristics of these techniques in biological and medical fields, the probes used for imaging have to be: i) cheap and disposable as they can be easily contaminated and damaged during their use; ii) small enough to resolve the investigated biological phenomena or object; iii) reproducible in their aspect and imaging capability. In the field of nanotechnologies the search for high-resolution imaging is vital.

In addition, electrodes of very small size are particularly useful to probe local concentrations on a microscopic scale. Several methods have been reported to insulate the surface of these electrodes, providing electrodes whose exposed dimensions are in the micrometer and in some cases nanometric range. These electrodes are suitable for applications such as Scanning Electrochemical Microscopy (SECM) and intracellular measurements. [4]

The fabrication of micro to nanoelectrodes, can be achieved by the electrochemical etching of a metal wire. This technique requires the key components of a common electrochemical cell: an electrolyte aqueous solution of NaOH or KOH, a cathode, usually a stainless steel or platinum rod/ring and an anode, a metal wire. Although Pt/Ir and tungsten are the metal of choice for most STM measurements, tungsten better suited our requirements for the setup phase, since it is a cheap material and needs milder chemical conditions to be etched away. In order to have a thorough understanding of how tips are usually produced through home made systems by researchers in STM laboratories, this study started from studying an ordinary setup and verifying its performances.

In this respect I tested the basic setup for the electrochemical etching of tungsten wires that was in use in the ISMN SPM laboratory in the CNR of Bologna. The system components are shown in **Fig. 1**.

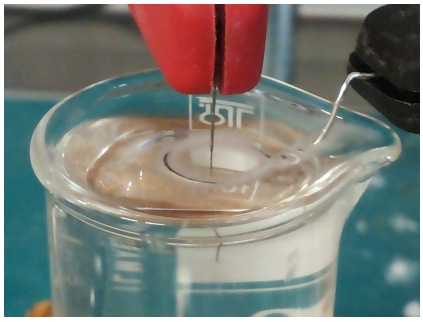

Fig. 1 Anode (W wire) suspended in the center of the cathode (Pt wire ring-shaped), both electrically connected and immersed in an aqueous solution of KOH.

A 25 mL beaker filled with an aqueous solution of KOH, a Pt wire shaped by hand into a ring serving as the cathode, a portion of roughly 2-3 cm of tungsten wire with diameter of 250 µm serving as the anode, complete the elements of the electrochemical cell needed to carry out an electrochemical etching. Both the anode and the cathode are clamped and connected to an electronic circuit that applies a voltage to drive the erosion process. The operator can control the applied potential and the shut-off sensitivity thanks to the dedicated software, as well as register the applied potential and the current passing through the circuit during the experiment. It is also possible to save the current vs. time and potential vs. time data, as ASCII files, to further analyze the curves.

This first part of the experiment was necessary to evaluate the possibility of standardizing the system. Besides, it was very useful in order to assess all the limitations and drawbacks typical of this procedure, that helped the design and suggested the solutions adopted in our new etching system. The experiment consisted in cutting from a tungsten wire reel a portion of 2-3 cm, since this material is quite stiff, it was often necessary to try to straighten the cut segment by means of tweezers or by hand, always wearing gloves in order to keep the wire as clean as possible. Once the wire segment was fairly straight, it is almost impossible to obtain a perfectly linear wire from a W coil, it was clamped and placed perpendicularly through the Pt ring, which was also clamped, inside the KOH solution. The Pt ring is kept on the surface of the solution, at the air/electrolyte interface. When both the electrodes are positioned and clamped, note that this operation usually takes some time if an accurate geometry is sought-after, a positive potential V_b is applied to the electrodes. In **Fig. 2** the progressive erosion of the W wire is schematized.

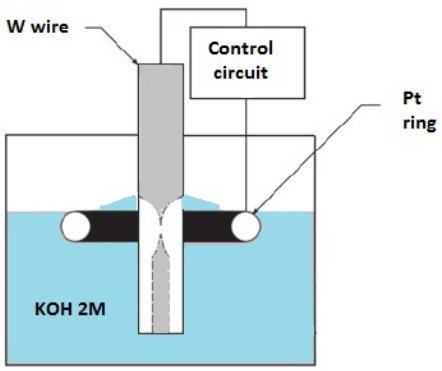

Fig. 2 Scheme of an electrochemical etching experiment setup. The W wire (anode) experiences a higher corrosion in its section closer to the Pt ring (cathode), where the electrical field is stronger, both the electrodes are connected to an electronic circuit and immersed in an aqueous solution of KOH.

An electrical field is generated in the area inside the Pt ring, the overall electrochemical reaction is:

Cathode	$6H_2O + 6e^- \rightarrow 3H_2\,(g) + 6OH^-$	SRP = -2,48 V
Anode	$W\,(s) + 8OH^- \rightarrow WO_4^{2-} + 4H_2O + 6e^-$	SOP = +1,05 V
	$W\,(s) + 2OH^- + 2H_2O \rightarrow WO_4^{2-} + 3H_2\,(g)$	E^0 = -1,43 V

At the cathode water is reduced to form bubbles of hydrogen gas, while at the anode the W oxidizes to give WO_4^{2-} tungstate anions soluble in water. The standard potential E^0 of the overall process is obtained by the sum of the standard reduction potential (SRP) and the standard oxidation potential (SOP). To obtain tungstate anions, a potential higher than 1,43 V is thus needed according to theory. Actually, due to kinetics limitations of the heterogeneous electron transfer process at the electrode surface, the potential required to drive the reaction is usually higher than that calculated from standard electrode potentials. [5]

The etching process results in the W wire thinning, with a higher rate by the section of the wire in proximity of the cathode, until its tensile strength is overcome by the weight of the immersed bottom part. At this point the wire breaks and two sharp tips are formed. Even if in literature some researchers reported that both the top and the bottom tip could be used with good results. [6] Only probes from the top part of the wire were collected in our case. The reasons behind this decision were two. First, even with the less concentrated electrolyte solution, the erosion experienced by the bottom tip was always more intense relatively to the top one, making it very difficult to handle and almost impossible to mount in a STM tip-holder. Second, the mechanical stress due to the fall subsequent to the tip formation was enough to damage the tip apex and the attempts to pick it up from the bottom of the beaker with tweezers could only make the situation worse.

A fundamental step in tip production coincides with the tips formation mechanism. It has been studied that the etching current should stop immediately after the tip drop, otherwise the erosion of the new tip continues, resulting in a dull tip. This has been called back-etching. [7,8] To prevent this unwanted process, the best solution resulted to be using a cut-off circuit implemented in the device

controlling the current and the applied potential (**Fig. 3)**. Such electronic circuit, has the function to stop the applied voltage as soon as the wire breaks. It can detect the change of current flowing through the system, when the wire breaks the resistance in the cell is noticeably increased, consequently the current drops down and the applied voltage is stopped by the feedback mechanism.

Fig. 3 Electronic device realized by Falco Consulting limited.

In this experiment two parameters were varied and influenced the final tips shape. The applied voltage and the shut-off sensitivity, this number in our software controls the change in current required to shut off the circuit when the etching is complete. It was necessary to find the right setting for this parameter, expressed in percentage, since if the setting was too high the etch could never stop, while if it was too low the system may be too sensitive and shut off early.

On the whole, about 60 tips were produced with the standard system. As electrolyte a solution of KOH 2M was chosen, while the applied potential V_b was varied in the range 1,5 – 7,5 V and the shut-off sensitivity values employed were 30% 40% 50%. The setup geometry such as the wire immersion depth and the Pt ring, were kept fixed as much as possible considering the limitations of this approach. After the probe was formed it was carefully taken with tweezers, since even the smallest bump would result in a dented tip as shown in **Fig. 4**.

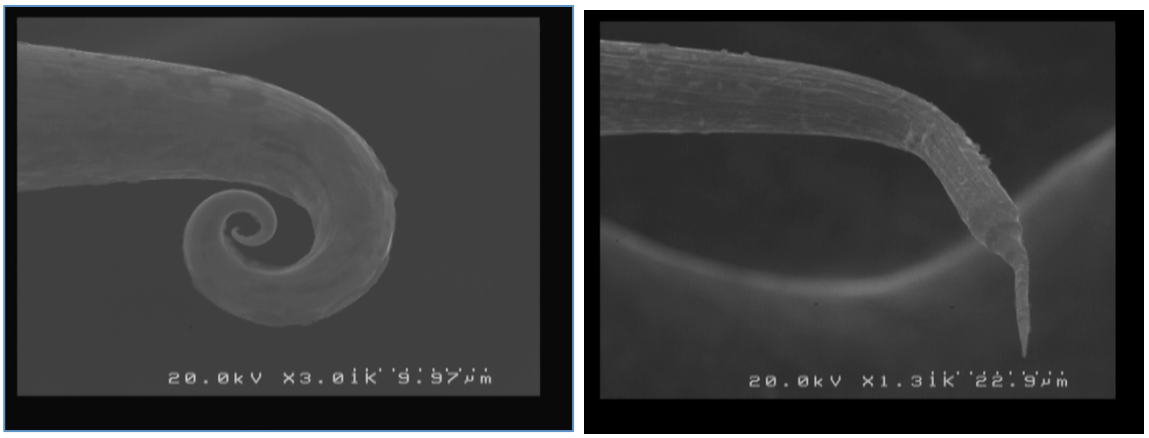

Fig. 4 Scanning electronic microscope images showing damages at the final part of two tips not handled in the correct way.

The tip was then observed under an optical microscope at 10X magnification for a first evaluation of the general shape and a finer inspection at the Scanning Electron Microscope (SEM) followed. By the SEM it was possible to determine if the tip shape was uniform and symmetrical as desired or if it presented points of discontinuity, asymmetry or any general flaws. This also made possible to calculate a "success rate" typical of the standard method, defined as the percentage of how many tips with uniform exponential shape (e.g. the one displayed in **Fig. 5**) were obtained among all the produced ones.

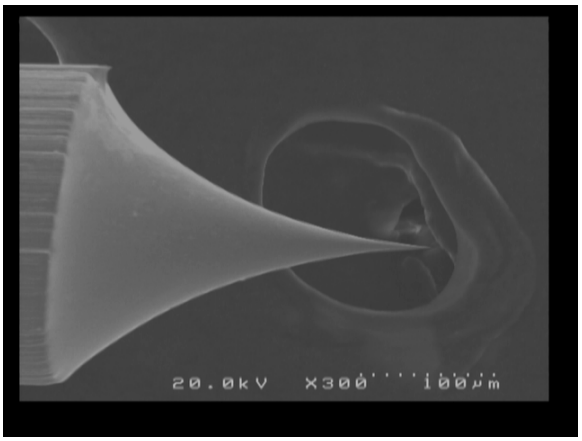

Fig. 5 SEM image of one of the tips that showed a uniform exponential shape.

The SEM images revealed some typical shapes among those tip that did not result in a uniform conical or exponential shape. One of the tip shapes that occurred the most was that reported in **Fig. 6** which represents a typical (multi-staged) tip. This shape is caused by the wire moving upward

during the etching, in fact even a slight movement probably due to the gradual decrease of the weight of the final part results in several separated stages of etching.

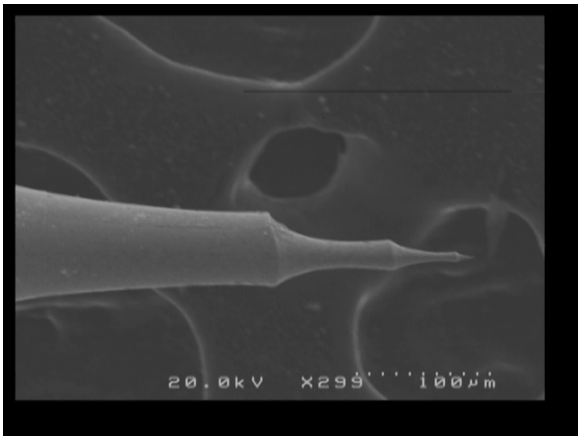

Fig. 6 SEM image of a tip with several separated stages of etching.

Other recurrent anomalous shapes were found in tips that were uniformly etched but with an asymmetrical profile, like that shown in **Fig. 7** (left) or probes that instead showed a total lack of symmetry and uniformity like the one in **Fig. 7** (right).

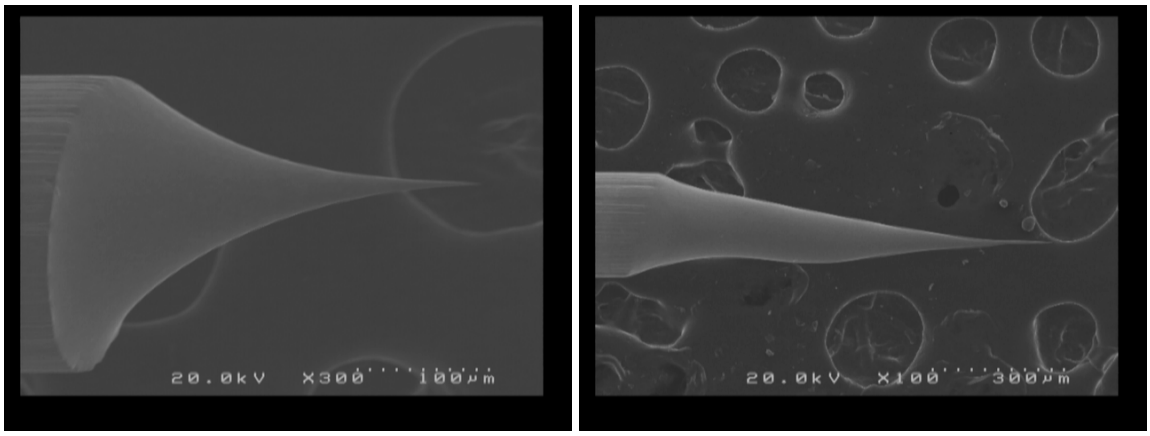

Fig. 7 SEM images of a tip uniformly etched but with an asymmetrical profile (left) and of one with no symmetry at all.

When all the tips were characterized by means of SEM, in order to evaluate the correlation between the arbitrary chosen "uniformity parameter" (the estimated by the quality check operated by observation of the tips at the SEM) of tip profile and applied voltage and time of the experiment, the 3D graph in Fig. 8 was made.

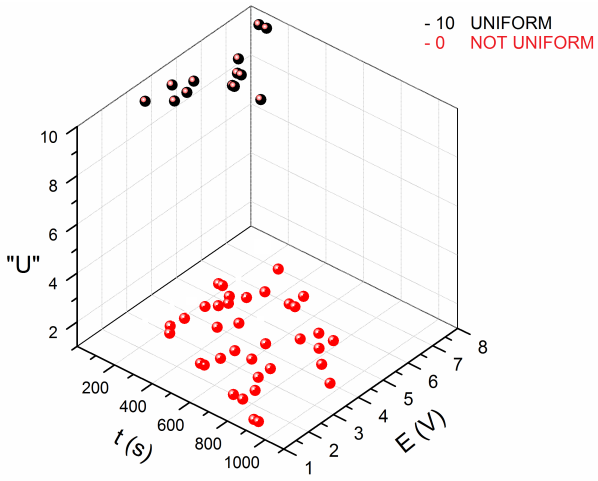

Fig. 8 3D graph reporting time vs. potential vs. "uniformity" of the tips obtained with the standard method.

This graph reports the applied voltage (x) versus time (y) and on the z-axis a binary parameter to represent the uniformity of tip profile. To highlight as much as possible the two states, the value 10 was given to tips characterized by uniform exponential profile and 0 was assigned to those tips lacking this profile uniformity. As one can see clearly from the figure, only few tips responded to the requisites of uniformity while the vast majority proved to be asymmetrical in some of the ways mentioned before. The success rate of the standard method here adopted was thus calculated and resulted to be of only about 20-24% depending on how strictly the "uniformity", still an arbitrary parameter, was considered.

By this qualitative analysis applied to the standard method, it was clear that it presents several drawbacks. To start with, even if the setup components are few, it is rather complicated to reproduce exactly the same geometry every time. Indeed small variations in the relative positioning of the W wire and the Pt ring are certain. Also the symmetry of the Pt ring hand shaped is questionable for obvious reasons. This changes in the geometry impact on the final tip shape. This can happen either by a movement of the clamps holding the electrodes or because of the generation of an electric field not completely uniform deriving from a Pt ring with imperfections. These issues linked to the final geometry of the system are correlated to the high difficulty the operator experiences to prepare every experiment and consequently to the long time each tip fabrication requires. Further on, as already mentioned, the success rate of this technique is quite low, as only 20-25% of the produced tips have a satisfactory profile.

Finally, taking into account the current vs. time curves related to different etching processes, it is clear that even for experiments characterized by the same parameters (KOH 2 M, applied potential

3 V), as in **Fig. 9**, the trends are considerably heterogeneous, regarding both the time of the experiments and the curves shape.

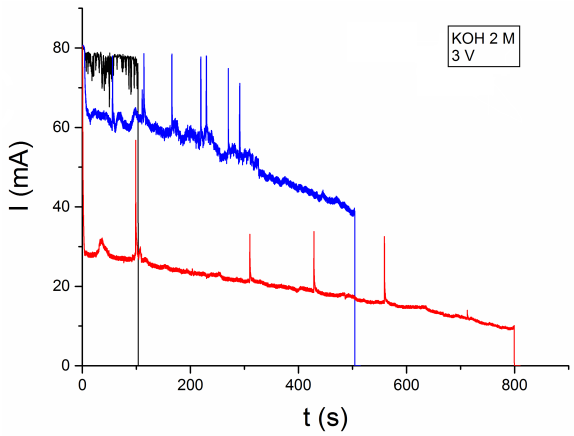

Fig. 9 Current/time trends of three experiments with the standard setup (KOH 2 M, applied potential 3 V)

In conclusion this method suffers of poor reproducibility, long preparative times and low success rate, makes it quite inefficient, and it needs to be improved.

This general procedure, with little adjustments, applies to most of the setups adopted so far. In literature several variations of the drop-off method are proposed for a fabrication with the best control of shape: single lamella, double lamella, zone electropolishing, orizontal setting, double etching, multiple etching, dynamic etching or even a controlled hydrodynamic flow. [10-13]

Our device was designed and tested in order to address the common issues that still persists in many of the aforementioned works as well as in the standard method previously described. Most of the procedures proposed, have complicated setups, require a great amount of skill from the operator and are not very reproducible.

The method proposed in this work, was chosen for its simplicity, high reproducibility and control of shape as well as because the resulting quality of the tip is not influenced by the operator skills.

This work started from defining the optimal geometric parameters that characterize a high-quality tip, intended as a tip that would provide high-resolution surface morphology STM images.

Our definition was based on the results found in previous literature: a high-quality tip should have a conical/exponential shape characterized by a small opening angle (OA), a radius of curvature (ROC) as small as possible (20 nm or less) and a high aspect ratio (AR). A higher

aspect ratio of the STM tip leads to improvement of reliability of STM images too, especially in imaging of nanometric deep trenches [14,15] and rough profiles. [16] A scheme of the influence of tip aspect ratio on STM image readability and reliability is shown in **Fig. 10**. [17]

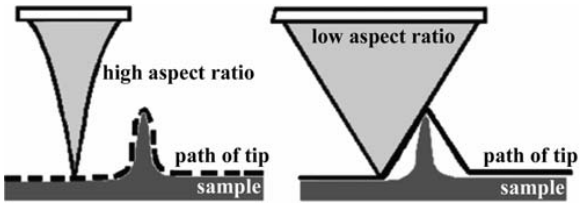

Fig. 10 Influence of tip aspect ratio on STM image readability and reliability. [17]

If we consider a typical probe like that in **Fig. 11** comparable to a cone, the AR is the height to the base diameter ratio. The OA is the vertex angle made by a cross section through the apex and the center of the base, in our case the OA were calculated from cross sections with a height of 5-10 μm.

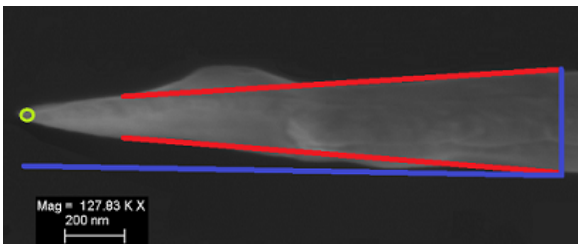

Fig. 11 Geometrical parameters defining a high quality tip: radius of curvature (ROC), the radius of the green circle encompassing tip apex; opening angle (OA), the angle between the two red lines tangents to the cone surface; aspect ratio (AR), calculated by dividing the height of the cone by its base, both in blue.

These geometrical requirements refer to an STM tip that would provide highly resolved images of a micro/nanostructured surface, whereas a large OA and low AR are preferred to study a perfectly flat surface (e.g. HOPG) since the mechanical stability is enhanced and thus tip vibrations are reduced providing a more precise imaging.

The New Etching System

Etching system

In order to produce such high-quality tips, a new etching system was expressly designed and developed, during the PhD work program. The system main body is divided in two parts that form a

cave PTFE cylinder with a base diameter of 6 cm and a height of about 8 cm, inside which the reaction takes place (**Fig. 12**).

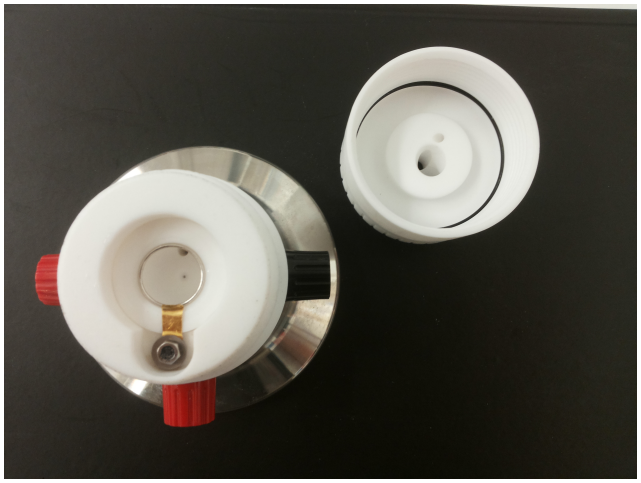

Fig. 12 The two components of our device while open. Bottom part (left) and top part (right).

The bottom part contains the electrolytic solution and is fixed onto a solid steel base to minimize vibrations. At the top of this chamber is placed an adapter that holds a microsewed Pt ring (∅=15mm), the cathode, at the air-liquid interface. Thanks to the refined geometry of the ring, a perfectly uniform electric field can be generated. A golden plate provides the electrical connection to the cathode, this was a modification implemented after the initial connections in brass proved to be unsuitable for our purpose, since they were oxidized in place of tungsten.

Initially the device was designed to keep the W wire pulled, so the wire was fixed to the upper part and blocked by a screw at the bottom, also providing the electric connections. After a few experiments it was clear that this mechanical solution was not ideal to obtain an atomically sharp tips. In fact all the probes fabricated in this way, were truncated at the end, like the one in **Fig. 13**. This behavior was ascribed to the stiffness typical of the tungsten wire and low elasticity of the material. It is likely that, even if the traction set was enough to prevent the wire from bending, once the diameter was reduced to roughly a fifth of its initial value, the tangential force produced by the wire was able to break it, long before the etching was complete.

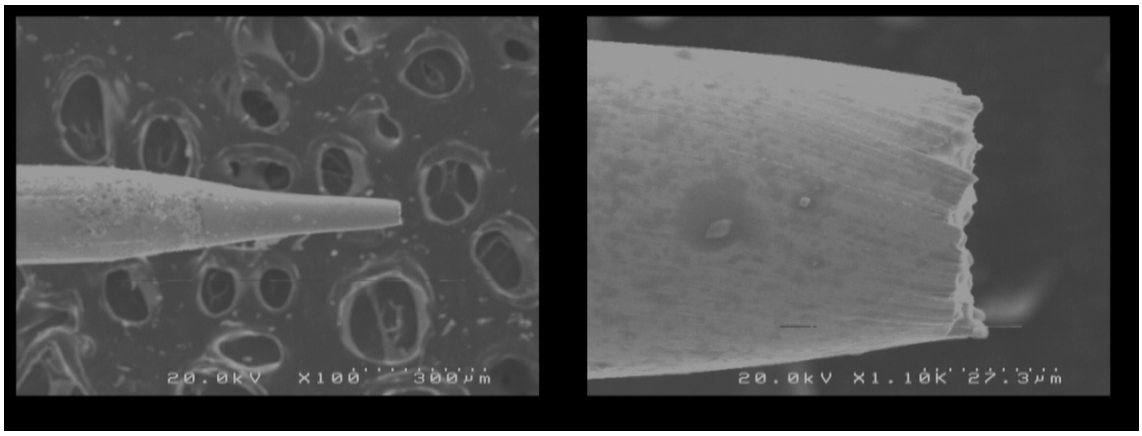

Fig. 13 Probe with truncated apex in two magnifications: scale bar 300 µm (left) and 27 µm (right).

Although this result was unexpected, it is not excluded that this characteristic truncated cone shape could be exploited in the production of probes for some different techniques from STM such as SECM UME (ultra micro-electrode). To overcome this unforeseen event, the mechanical holder of the wire had to be redesigned, so that it could keep the wire in place without pulling it and as a consequence the electric connection had to be modified as well. The solution that was adopted consisted in exploiting an electrically connected needle fixed to the upper part (**Fig. 14**).

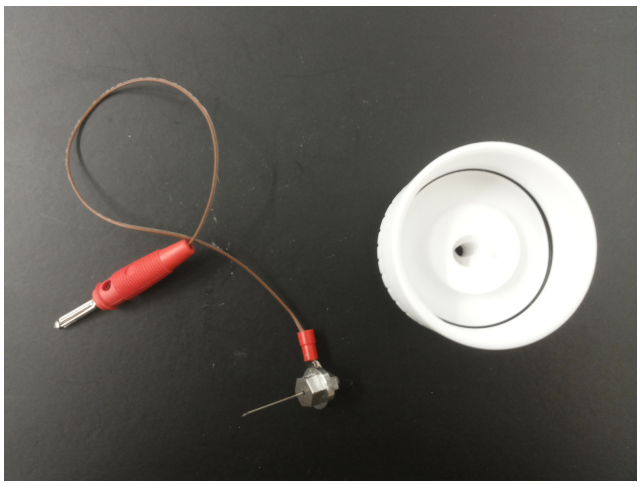

Fig. 14 Electrically connected needle used to hold the W wire in place without pulling it.

The bottom part is filled with the electrolyte solution up to the Pt ring. When the upper part is screwed onto the base the wire is immersed in the electrolyte solution and is positioned perfectly in the center of the Pt ring, so that it could undergo a symmetric corrosion. An O-ring gasket situated inside the upper part ensures a tightly closed unit (**Fig. 15**).

Fig. 15 Our electrochemical etching device when sealed.

For our experiments, the same electronic device designed by Falco Consulting Limited, utilized in the standard method already described, was employed. It is able to apply a potential difference up to 8 V and record the current flowing between the working and the counter electrode.

Our device exploits the common "drop-off" [5] method: the etching takes place until the tensile strength of the wire holding its final section is overcome by gravity, at this point the wire breaks and two tips are formed.

To classify the obtained tips, as said before, the geometric parameters taken into account were: aspect ratio (AR), opening angle (OA) and apical radius of curvature (ROC).

Optimization of the Process

Once all the mechanical issues were fixed, it was fundamental to find the specific set of experimental parameters, influencing the final shape of the tip, that would give the best results. In particular, three parameters were taken into account: wire immersion depth in the solution, applied potential and concentration of the electrolyte. From time to time only one parameter was varied, while the other two were fixed.

Regarding wire immersion, these lengths of the wire out of the needle were tried: 9, 7 and 5 mm. To deal with a valuable statistics, at least 10 experiments were conducted using each of these geometries.

Every tip was characterized by scanning electron microscopy (SEM) and the images were elaborated by ImageJ, an image processing program. Thus it was possible to evaluate the tips conformity to the established geometric standards and to find the best combination of parameters that led to high-quality tips. The length out of wire chosen after the aforementioned procedure was 9 mm. This parameter was never modified in the following experiments.

The applied potentials were varied in the range 1,5 V < E < 8 V, which were limited at the lowest value by the formal overall reaction E_0 and at the higher value by the instrument capability. Furthermore these values were likely to be suitable for our system, considering previous literature results. In particular the potentials employed were 2/4/6/8 V, to test each of this values, at least 3 to 10 experiments were carried out. The same quality check modality followed for the immersion depth lead to the choice of the optimal applied potential, which resulted to be 8 V.

Finally, using 9 mm and 8 V as parameters of choice, several KOH concentrations were tested, namely 1/1,5/2/2,5/3/3,5/4/6/8/10 M. The first concentrations tried were 2/4/6/8/10 M. With KOH 6 M and higher concentrations, the tips produced experienced a coarse etching, resulting in an irregular tip surface. For this reason, in order to have a finer screen of the parameters explored, concentrations of 1/1,5/2,5/3,5 M were employed. Eventually KOH 2 M was the concentration that proved to give the best results in terms of the quality of the tips produced.

In conclusion the optimal combination of parameters specific to our system, as emerged from experimental work, was: a length out of the needle of 9 mm, an applied potential V_b of 8 V and KOH 2 M. Using this optimized combination of parameters gave excellent results in term of reproducibility. In fact as much as 75% of the tips fabricated with our device after the optimization, were categorized as high quality tips as they well conformed to the previously stated geometrical parameters. Some of these tips are reported in **Fig. 16**.

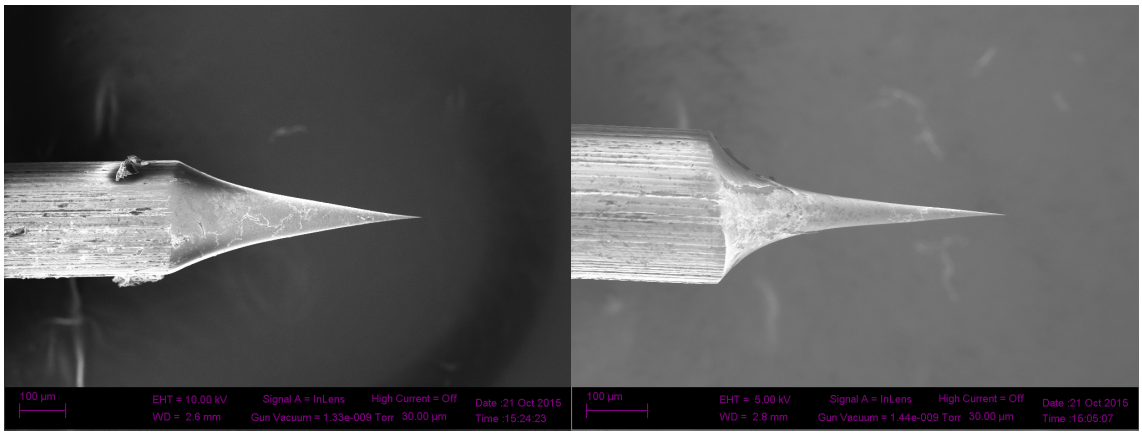

Fig. 16 Two high quality tips. Scale bar: 100 µm.

In addition, it was noteworthy that the current/time curves recorded, for processes conducted under the same experimental conditions, showed current trends reproducible and almost superimposable as shown in **Fig 17**.

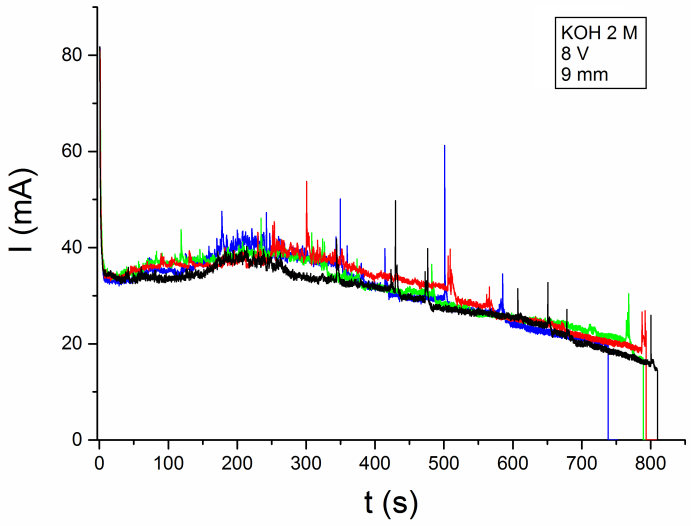

Fig. 17 Current vs. time curves relative to four etching process with the optimized set of parameters: KOH 2 M, V_b = 8 V and a length out of the needle of 9 mm.

For the I/t curves relative to the erosion process with optimized parameters (9 mm, V_b 8 V and KOH 2 M), a characteristic trend is shown in **Fig. 18**.

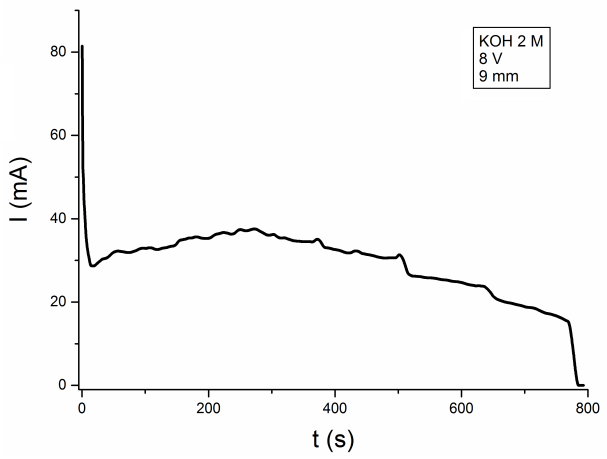

Fig. 18 Typical current vs. time curve obtained from an etching experiment with the optimized set of parameters: 9mm length out of the needle, V_b = 8 V and KOH 2 M.

In the first few seconds after the voltage is applied, the current drops from 80 mA to 25-35 mA, then it starts to rise and after reaching a maximum point averagely at 40 mA, it decreases steadily, with a constant slope, until the tip is formed. Then drops to 0 mA, as soon as the cut-off circuit interrupts the current flow. Below a reasonable hypothesis for the explanation of this trend is provided. For a deep understanding of this curve, all the chemical and electrochemical reactions involved in the etching process of tungsten in alkaline media, must be taken into account. The electrochemical reactions are usually resumed as described by Equation 1 in the paragraph concerning the standard method. For simplicity the anode reaction is repeated here:

Anode $\quad W\,(s) + 8OH^- \rightarrow WO_4^{2-} + 4H_2O + 6e^-$ $\quad SOP = +1{,}05\ V$

This is certainly a good approximation, as far as the main electrochemical reactions are considered. Actually the involved mechanism is quite more complicated and has been deeply investigated and described. [18,19] Starting from these previous findings, the typical trend for our reactions was interpreted as follows: initially the current drops for few seconds, due to the charging of the electrical double layer, as confirmed by its shape in the in the I/ t graph. After the reach of a minimum point, the current starts to rise again with an approximately constant slope. This trend, quite particular for an erosion process, can be explained if both the chemical and the electrochemical contribution are considered. In fact it is known that WO_3, the native oxide of tungsten which develops in air, it is soluble in KOH, following the reaction:

$$WO_3 + KOH \rightarrow WO_4^{2-}$$

When the wire is submerged in the KOH solution, the oxide WO_3, that forms a sort of sheath around the surface of the wire, begins to dissolve, thus uncovering the metallic not oxidized tungsten under the oxide layers. While WO_3 is dissolving, more and more sites for the electrochemical oxidation become available and the anodic reaction takes place as reported in scheme 1:

Anode $W(s) + 8OH^- \rightarrow WO_4^{2-} + 4H_2O + 6e^-$ SOP = +1,05 V

After the rise, when the currents reaches the maximum point, all the oxide that shielded the wire has dissolved and the maximum surface area of the tungsten wire is exposed and available for the anodic electrochemical reaction. A characteristic trend of erosion processes follows, where the current diminishes proportionally with the decrease of the electrode superficial area and the increased resistance R. Approximately, this current trend is characterized by a fixed slope, which is proportional to the etching rate of the system. The process terminates with the breaking of the wire leading to the formation of the tips, and immediately after the cut off circuits interrupts the current flow.

Another hint that this may be the mechanism involved in this experiment, come from the behavior of the current trends registered for experiments with a higher concentration of electrolyte than the standard: KOH 10 M. In fact, as reported in **Fig. 19**, the characteristic currents for these experiments show a quite different trend from those relative to experiments with the optimized conditions. The three curves in **Fig. 19** show a current that steadily decreases with a little slope and finally drops to zero. Here is evident a total lack of the bump, in other words the section where the current increases due to the chemical removal of the oxide, is no longer there. This is induced by the higher concentration of KOH, which produces a quicker dissolution of the oxide layer.

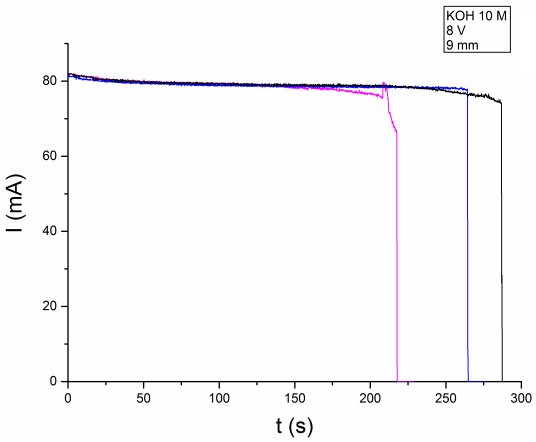

Fig. 19 Current vs. time curves relative to three etching experiments with the set of parameters: 9 mm, V_b = 8 V and KOH 10 M.

In order to experimentally verify this hypothesis, we tried to exclude the chemical contribution of the etching process, which in our hypothesis is responsible for the rising part of the current vs. time graph, namely the chemical dissolution the oxide, to see whether the trend would be modified. For this reason, the tungsten wire was submerged in an aqueous solution KOH 10M for increasing times, up to 15 hours. After that, the wire was rinsed with KOH 2M and the etching process was carried out using the same experimental conditions of the standard experiments. Observing the graph in **Fig. 20**, it is clear that the bump characterizing our standard experiment gradually shrinks with the inverse of the immersion time employed. This is due to the oxide dissolution and after the maximum time used of 15 hours it is completely removed from the surface, as one can see from the graph, where the bump is no longer present.

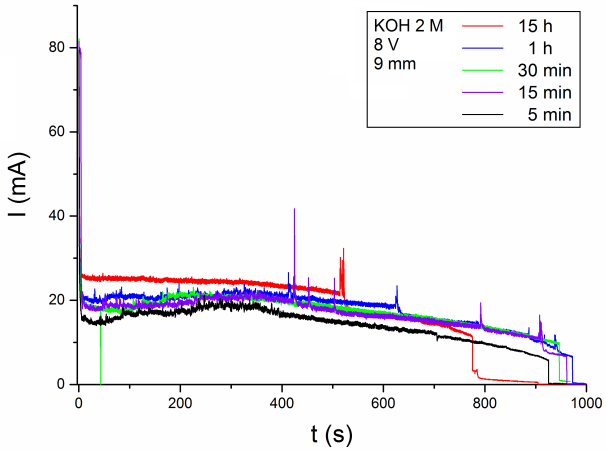

Fig. 20 Current/time curves relative to several etching experiments with the optimized set of parameters: 9 mm, V_b = 8 V and KOH 2 M. Before all these etching processes, the W wire was submerged in KOH 10 M for times ranging from 5 min to15 hours.

Another reasonable remark coming from this last experiment is that, by applying a potential to the system, the dissolution process is enhanced. In fact, if the removal of the external oxide layer takes around five minutes for experiments with optimized parameters (9 mm, V_b 8 V and KOH 2 M), is evident that even after an hour of immersion in KOH 10 M (blue curve in **Fig. 20**), therefore in presence of only the chemical dissolution process, a little bump is still visible suggesting the presence of some residual oxide.

Modification for use as SECM electrode

In order to adapt these electrodes to SECM working electrodes, further modifications were required. In fact this technique usually exploits disk electrodes as probes, which have a metal wire encapsulated in a glass sheathed and only the very end of the wire is uncovered. This allows to perform local imaging, and to achieve a good resolution. We decided to exploit a procedure normally used for the fabrication of probe used in Electrochemical STM (ESTM). This process (see methods) was carried out in the laboratory of Prof. Goletti (University of Rome "Tor Vergata").

The covered tips were characterized in the CNR – IMM laboratories by means of an environmental SEM (Zeiss Evo LS10). SEM images (**Fig. 21**) show a tip completely covered by wax above and a tip correctly insulated, with only the very end exposed. Prior to every electrochemical experiment each tip can be further characterized by cyclic voltammetry.

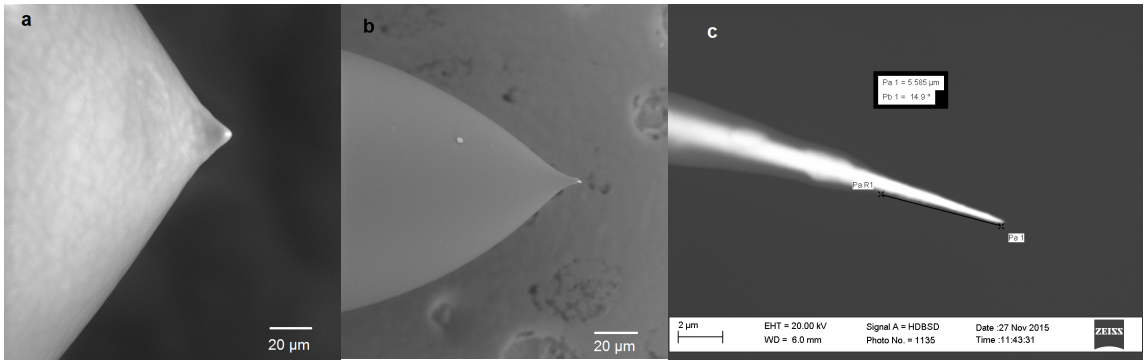

Fig. 21 SEM images of: a) a tip fully covered by wax; b) and c) a tip correctly insulated at different scales.

The adopted method have has proven effective to insulate the surface of our homemade probes, providing electrodes whose exposed dimensions are in the nanometric range.

Insulation procedure

Prior to insulation tips were washed in triply distilled water. Insulation of the tips was carried out with molten Apiezon wax. The sharp etched tips were mounted vertically on a manipulator. A copper plate held horizontally, was heated using a soldering iron element and used to melt the Apiezon wax. A 1-mm-wide rectangular slit extends from one side to the center of the copper plate, providing a temperature gradient (colder at the open end and hotter at the closed end) for the melted wax. The tip is brought from underneath the slit by means of a manipulator. The tip is first moved slowly into the hot wax and allowed to attain thermal equilibrium and uniform wetting. The tip is then raised through the wax and allowed to break the top surface of the melt. If the tip breaks the surface at too hot a region, it is mostly bare while if the tip breaks at the colder region of the melt, it raises a blob of wax above it. In between these two regions exists an optimum point where the wax insulates the tip almost completely. The insulated tip is moved sideways out of the groove so as to leave the very end of the tip unperturbed. Characterization by means of cyclic voltammograms showed that the Apiezon wax is inert in most electrolytes. [20]

Preliminary results

The uncovered metal wire of an insulated tip was inserted inside a glass capillary, with the wax cap blocking the probe. A solution of Collodion was delicately brushed at the interface between the capillary and the base of the wax clot and let dry in air for several minutes. Such probe was mounted as working electrode on the SECM. Through the movement controlled by SECM stepper motors and with the visual help of the inverted optical microscope in transmittance it was possible to penetrate a cell without damaging as shown in **Fig. 22**. The last part of the tip is inside the cell, which maintained its 3D structure without any modifications. This proves that this kind of electrodes thanks to their nanometer sized dimensions could be exploited in the future for intracellular studies.

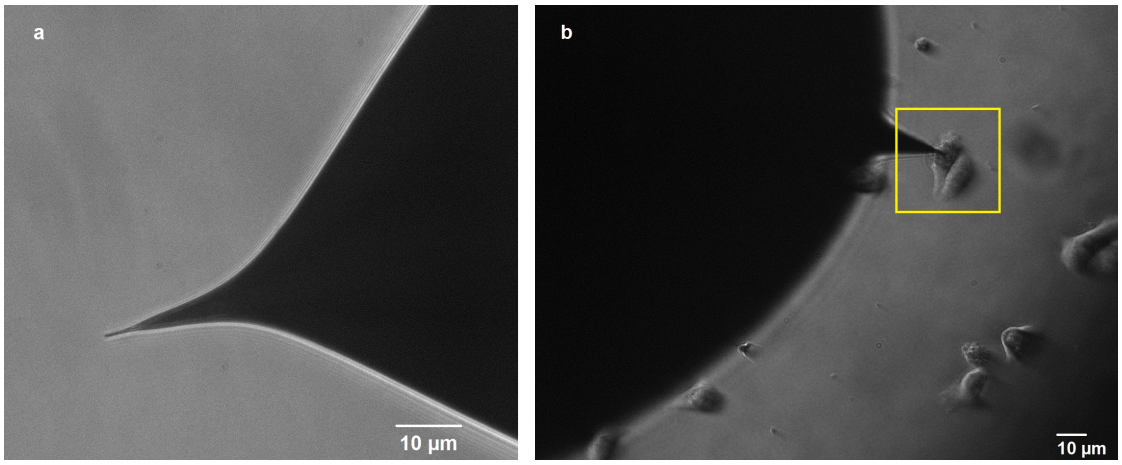

Fig. 22 Optical image of the SECM nanoprobe. a) Outside the cell and b) inside the cell.

Conclusions

As mentioned in the introduction to this chapter, electrodes designed to be used for imaging biological samples have to be cheap and disposable, small enough to resolve biological processes and reproducible in their aspect and imaging capability. In addition, electrodes of nanometer size allow to performing intracellular measurements like probing local concentrations with high spatial resolution. The fabrication method proposed in this work and the probes obtained comply with all aforementioned characteristic.

References

1. Cricenti, A. (n.d.). Scanning probe microscopy in material. https://doi.org/10.1088/0022-3727/44/46/464008
2. Santos, N. C., & Castanho, M. A. R. B. (2004). An overview of the biophysical applications of atomic force microscopy, *107*, 133–149. https://doi.org/10.1016/j.bpc.2003.09.001
3. Amemiya, S., Guo, J., & Xiong, H. (2006). Biological applications of scanning electrochemical microscopy : chemical imaging of single living cells and beyond, 458–471. https://doi.org/10.1007/s00216-006-0510-6
4. Cox, J. T., & Zhang, B. (2012). Nanoelectrodes : Recent Advances and New Directions. https://doi.org/10.1146/annurev-anchem-062011-143124
5. Colton R. J., Ibe J. P., Bey P. P. , Brandow S. L. Brizzolara R. A. , Burnham N. A., & Dilella D. P. On the electrochemical etching of tips for scanning tunneling microscopy On the electrochemical etching of tips for scanning tunneling microscopy, *3570*(1990). https://doi.org/10.1116/1.576509
6. Fotino M. et al. Tip sharpening by normal and reverse electrochemical etching. *Review of Scientific Instruments*, 64, 1, 159-167 (1993) doi: http://dx.doi.org/10.1063/1.1144419
7. Nakamura Y., Mera Y., and Maeda K., *Rev. Sci Instrum.*, 70, 3373 (1999)
8. Sun W. X., Shen Z. X., Cheong F. C., Yu G. Y., Lim K. Y., and Lin J. Y. , *Rev. Sci Instrum.*, 78, 073707 (2007)
9. Silva, E. L., Silva, R. F., Zheludkevich, M., Oliveira, F. J. Novel electrochemical method of fast and reproducible fabrication of metallic nanoelectrodes, , *Rev. Sci Instrum.*, 85, 0*95109*. (2014) https://doi.org/10.1063/1.4895639
10. Hagedorn, T., Ouali, M. El, Paul, W., Oliver, D., Miyahara, Y., Grütter, P., … Oliver, D. (2011). Refined tip preparation by electrochemical etching and ultrahigh vacuum treatment to obtain atomically sharp tips for scanning tunneling microscope and atomic force microscope. *Rev. Sci Instrum.*, 82, *113903*. https://doi.org/10.1063/1.3660279
11. Melmed A. J., in Fifth International Conference on Scanning Tunnelin Microscopy/Spectroscopy (1991), Vol. 9, pp. 601–608.
12. Kulawik M., Nowicki M., Thielsch G., Cramer L., Rust H.-P., Freund H.-J., Pearl T. P., and Weiss P. S., *Rev. Sci. Instrum*. 74, 1027 (2003).
13. Yu Z. Q., Wang C. M., Du Y., Thevuthasan S., and Lyubinetsky I., *Ultramicroscopy*108, 873 (2008).

14. Pasquini A, Picotto GB, Pisani M STM carbon nanotube tips fabrication for critical dimension measurements. *Sens. Actuators. A Phys.* 123–124:655–659. doi:10.1016/j.sna. 02.036 3. (2005)
15. Vasile MJ, Grigg DA, Griffith JE et al. Scanning probe tips formed by focused ion beams. *Rev Sci Instrum*, 62 (9):2167–2171. (1991) doi:10.1063/1.1142334 4.
16. Resnik D, Vrtacnik D, Aljancic U et al. Different aspect ratio pyramidal tips obtained by wet etching of (100) and (111) silicon. *Microelectron J*, 34:591–593. (2003) doi:10.1016/S0026-2692 (03)00056-9
17. Tahmasebipour, G., Hojjat, Y., Ahmadi, V., & Abdullah, A. (2009). Optimization of STM/FIM nanotip aspect ratio based on the Taguchi method. *International Journal of Advanced Manufacturing Technology*, *44*(1–2), 80–90. https://doi.org/10.1007/s00170-008-1799-4
18. Johnson J. W. and Wu C. L., *J. Electrochem. Soc.* 118, 1909 (1971).
19. Kelsey G. S., *J. Electrochem. Soc.* 124, 814 (1977).
20. Nagahara L. A., Thundat T., and Lindsay S. M. , Preparation and characterization of STM tips for electrochemical studies, Citation: *Rev. of Sci. Instrum.* 60 , 3128 (1989); doi: 10.1063/1.1140590

Conclusions

The aim of this project was to investigate cell-material interaction through the use of Scanning Electrochemical Microscopy. The morphology of the cells changes consistently with the surface where they adhere and is affected by a number of factors including surface structuration as well as surface peculiar chemical functionalities.

In order to control both morphology and chemistry of the surface, mono-molecular layers of small organic molecules (specifically Pentacene, α-Sexithiophene and PDI8-CN2) were deposited on SiO_x substrates by means of Organic Molecular Beam Epitaxy (OMBE). MCF10A cells were grown on the aforementioned substrates.

The sample characterization by means of epifluorescence microscopy showed that the organic monomolecular layers increase the biocompatibility of bare SiO_x. MCF10A cells adhere and proliferate on the substrates investigated whereas on SiO_x cells grown in 3D structures, maximizing the cell-cell interactions. This behavior accounts for a higher cell-surface affinity of the cells on the 2D organic monolayer in respect to the SiO_x.

In order to evaluate the cell proliferation on the different substrates, the cells were stained, imaged and counted, the averaged nucleus area for cells were also estimated. The cellular population on Pentacene (P5) resulted to be the only one significantly different from that on SiO_x, this was not the case on α-Sexithiophene (6T) and PDI8-CN2. The populations on the different monomolecular layers were significantly different, so the chemical microenvironment of the cell has an effect on cell proliferation.

Scanning Electrochemical Microscopy imaging performed on each sample made possible to assess cell shape, structure and size. This SPM technique was adopted on the grounds that: i) it has a high throughput capability (scanning rates of several microns per second are achieved), ii) does not require a stain, which can be toxic for the cells and is not always capable to mark cell topography and iii) it works in physiological solution and can be performed on living cells. More parameters that define cellular morphology on different substrates could be obtained by SECM characterization, namely nucleus height, surface contact area, half width half maximum and inclination angles of the cell surfaces.

Image analyses allowed to calculate the inclination angles through the statistical function slope distribution, which calculates the slopes as vertical derivatives of the facet inclinations on the whole surface of the cell.

The combination of the aforementioned parameters, consented to outline the archetypical profile shown by cells on each sample. Nucleus heights were not affected by the substrates and were all the same. All cells showed two typical inclination angles, the lower one measured between the membrane leading edge and the surface and the higher one shown by the side of the nucleus to the substrate.

Cells on Pentacene have the highest volume and are well spread, that should involve a higher adhesion.

The typical cell on 6T occupies a reduced surface if compared to that on P5, its width at half maximum is intermediate between the other two. This cell is bell shaped, thus shows a lower inclination angle relative to the portion of membrane close to the nucleus. The shape is swollen in respect of the cell on P5. Lastly the cell on PDI8-CN2 has a contact area comparable to the one on 6T, its nucleus is shaped as a slightly elongated spheroid. In this case the cell is shrunk, the membrane is tightly adhered to the nucleus and overall the cell volume is reduced.

To sum up, among the samples studied the monomolecular layer of P5 on SiOx resulted to be the environment for which MCF10A cells have the best affinity, considering the higher proliferation, the larger adhesion and the morphology they show. By contrast PDI on SiOx turned out to be the substrate with which cells interacts the least, as proved by both the cellular count and the measured area. Lastly, T6 on SiOx has an intermediate behavior between the other two, in fact it is significantly different from PDI both as number of cells and of average area, so it displays a better affinity and is not significantly different from P5 in terms of average areas, which could suggest that this material promotes adhesion more than proliferation.

The method developed can be exploited to determine morphology and adhesion of different cell kinds both pathogenic and not, on different substrates. Additionaly, the definition of a new geometrical parameter can lead to a quantitative description of cellular morphology and thus help the study of metastatic mechanisms.

In the perspective of studying cell-material interaction by SECM a breakthrough implicates the size reduction of the working probes from micrometer dimensions to nanometer dimensions. These electrodes have to be cheap and disposable, as they can be easily damaged or contaminated during imaging of biological samples. Reduced dimensions are essential to resolve biological processes and to perform intracellular analyses with high special resolution. Lastly these tips need to be reproducible in their aspect and imaging capability. The fabrication method proposed in this work and the probes obtained comply with all these requirements.